

**PASSIVE RADIATIVE COOLING USING OPTICAL THIN FILM COATINGS**

by

Muhammed Ali Keçebaş

Submitted to the Graduate School of Engineering and Natural Sciences in partial  
fulfillment of the requirements for the degree of Master of Science

Sabancı University

July 2016

PASSIVE RADIATIVE COOLING USING OPTICAL THIN FILM  
COATINGS

APPROVED BY:

Assoc. Prof. Dr.....  
(Thesis Supervisor)

Kürşat Şendir 

Assoc. Prof. Dr.....

Burcu Misirkoğlu 

Asst. Prof. Dr.....

Erdem Ögüt 

DATE OF APPROVAL: 28/07/2016

© Muhammed Ali Keebaş, 2016  
All Rights Reserved

## **ABSTRACT**

### **PASSIVE RADIATIVE COOLING USING OPTICAL THIN FILM COATINGS**

**Muhammed Ali Keçebaş**

**Mechatronics Engineering, MSc. Thesis, 2016**

**Thesis Supervisor: Assoc. Prof. İbrahim Kürşat Şendur**

Keywords: Thin Films, Nanophotonics, Spectral Behaviors, Radiative Cooling

Radiative cooling is a passive way of cooling by which a body loses heat by emitting energy. When a body is exposed to sky, heat transfer between the body and sky occurs depending on transparency of the atmosphere through radiation. During nighttime, due to extremely low incident solar irradiation cooling can be achieved. However, during daylight nearly  $940 \text{ W/m}^2$  energy is present in Istanbul, due to sun and since emission by the object is not as high as this energy, cooling cannot be achieved. So, in order to achieve radiative cooling during daylight, incident solar energy has to be reflected strongly which prevents heating of the object. Also, by maximizing emission in the atmospheric transparency window in  $8\text{-}13 \mu\text{m}$  range, in which very low amount of solar energy is carried, radiative cooling can be achieved.

In this study, design studies about thin film filters are carried out whose focus is to achieve high reflection in the visible and near-infrared spectrums in which high amount of solar energy is present and maximize absorption/emissivity in  $8\text{-}13 \mu\text{m}$  spectrum where atmospheric transparency window is present. For these purposes, different design methods are examined, e.g. quarter wavelength stacks for high reflection and an impedance matching technique, Chebyshev transform, is used to increase emission in  $8\text{-}13 \mu\text{m}$  spectrum. For the performance evaluations, radiative heat transfer dynamics are examined and cooling powers are compared with a design results given in the literature. It is observed that significant performance improvement can be observed by proposed design methods.

## ÖZET

# OPTİK İNCE FİLM KAPLAMALAR ARACILIĞI İLE PASİF IŞINIMSAL SOĞUTMA

Muhammed Ali Keçebaş

Mekatronik Mühendisliği, Yüksek Lisans Tezi, 2016

Tez Danışmanı: Doç. Dr. İbrahim Kürşat Şendur

Anahtar Kelimeler: İnce film, nanofotonik, tayfsal davranışlar, Işınımsal soğutma

Işınımsal soğutma bir objenin etrafına enerji yayarak ısı kaybettiği pasif bir soğuma yöntemidir. Bir obje gökyüzü ile etkileşim halinde olduğunda atmosferin geçirgenliğine bağlı olarak obje ve gökyüzü arasında radyasyon aracılığı ile ısı transferi gerçekleşir. Gece saatlerinde gelen güneş enerjisi çok az olduğundan bu saatlerde soğuma gerçekleşebilir. Ancak gündüz saatlerinde İstanbul üzerine yaklaşık 940 W/m<sup>2</sup> güneş enerjisi gelmektedir ve objenin yaydığı enerji bu denli yüksek olmadığı için soğuma gerçekleşmemektedir. Bu yüzden gündüz saatlerinde objenin güneş enerjisinden dolayı ısınmasının engellenmesi ve ışınımsal soğutmanın gerçekleştirilebilmesi için gelen bu enerjinin güçlü bir şekilde yansıtılması gerekmektedir. Ayrıca objenin yayınım katsayısını çok düşük miktarda güneş enerjisinin mevcut olduğu ve atmosferik geçirgenlik penceresinin bulunduğu 8-13 µm tayfında yükselterek ışınımsal soğutma gerçekleştirilebilir.

Bu çalışmada amacı yüksek miktarlarda güneş enerjisinin mevcut olduğu görülebilir ve yakın kızılötesi bantlarda yüksek yansımaya ve atmosferik geçirgenlik penceresinin bulunduğu 8-13 µm tayfında yüksek yayınım katsayısına sahip ince film filtre tasarımları yapılmıştır. Bu amaçlar doğrultusunda yüksek yansımaya için çeyrek dalga boyundaki katmanlardan oluşan bir tasarım geliştirilmiş ve yüksek yayınım için ise bir empedans eşleştirme tekniği olan Chebyshev dönüşümü ile oluşturulmuş bir tasarım incelenmiştir. Performans değerlendirmeleri için ışınımsal ısı transferi dinamikleri incelenmiş ve soğutma güçleri literatürde verilen bir başka tasarım sonuçları ile karşılaştırılmıştır. Önerilen yeni tasarımların sonuçları göz önüne alındığında yüksek miktarda performans artışı gözlemlenmiştir.

*To my family ...*

## TABLE OF CONTENTS

Abstract .....	iii
Özet .....	iv
CHAPTER 1 INTRODUCTION .....	1
1.1. Literature Review.....	2
1.2. Contributions .....	5
1.3. Outline .....	6
CHAPTER 2 METHODOLOGY .....	7
2.1. Obtaining Reflectance, Absorption and Transmission of a Thin Film System with Characteristic Matrix Method .....	7
2.2. Analysis of the Characteristic Matrix and Quarter Wavelength Design .....	13
2.3. Heat Balance .....	21
2.4. Atmospheric Transmittance and Solar Irradiance .....	24
2.5. Investigation of Material’s Spectral Behaviors for Radiative Cooling .....	34
CHAPTER 3 RADIATIVE COOLING SYSTEM DESIGN .....	43
CHAPTER 4 MINIMIZATION OF REFLECTION ON THE FRONT SURFACE IN THE 8-13 $\mu\text{m}$ SPECTRUM BY USING CHEBYSHEV TRANSFORM .....	68

## List of Figures

Figure 1.1. Blackbody radiation curves of different object's which are at temperatures 300, 800, 1000, 2900 and 5800K from 100 nm to 100 $\mu$ m spectrum.....	3
Figure 2.1. Scheme of a single layer coating on a substrate with incident medium.....	8
Figure 2.2. Incidence angle of an incoming wave propagating in a medium with index of $n_0$ with respect to normal to the surface with refractive index of $n_1$ .....	10
Figure 2.3. Representation of angle of refraction in different mediums.....	12
Figure 2.4. Demonstration of high-low index layered thin film coating system where each layer is quarter wavelength thick, which is used to achieve high reflection around operation of wavelength, $\lambda_0$ .....	15
Figure 2.5. Reflections of high-low index layers each quarter wavelength thick 7 layers in total, where outer ones are high index layers, with different operational wavelengths. $n_{high}$ is 2.75 and $n_{low}$ is 1.45 and $n_{sub}$ is 1.5. Operation of wavelengths are 300, 600, 900 and 2500 nm.....	17
Figure 2.6. Reflections of high-low index layers, each quarter wavelength thick, consist of 3, 5 and 7 layers where outer ones are high index layers with 300 nm operation of wavelength where $n_{low}$ is 1.45, $n_{high}$ is 2.75 and $n_{sub}$ is 1.5.....	18
Figure 2.7. a) Reflections of high-low index layers, each quarter wavelength thick and outer layers are low index layers, with 300 nm of operation of wavelength where $n_{low}$ is 1.45, $n_{high}$ is 2.75. b) Only difference from 'a' is that outer layers composed of high index material. Indexes of substrates are set to 1.5, 2 and 2.5 in both 'a' and 'b'.....	18
Figure 2.8. Reflections of high-low index layers, each quarter wavelength thick, 5 layers in total in which outer ones are high index layers, with 300 nm of operation of wavelength and $n_{sub}$ is set to 1.5 and ratio of $n_{high}$ and $n_{low}$ is set to 1.37, 1.58 and 1.89.....	19
Figure 2.9. Reflections of high-low index layers, each quarter wavelength thick. Besides high reflection zones around $\lambda_0$ s, each case have high reflection zones around $\frac{\lambda_0}{3}$ , $\frac{\lambda_0}{5}$ , $\frac{\lambda_0}{7}$ .....	20
Figure 2.10. Heat balance scheme for an object in an open environment. Left side represents the contributions to heat inflow to the system and right hand side contains the heat outflows from the object.....	22
Figure 2.11. Representation of azimuth and incidence angles of the sun.....	25

Figure 2.12. Comparison of solar irradiation at Istanbul (41,28) on March, June and December in 21 <sup>st</sup> in 2016 with respect to wavelength.....	26
Figure 2.13. Comparison of solar irradiation at Istanbul (41,28) on 21 <sup>st</sup> March 2016 at 7:00, 9:00 and 12:00 with respect to wavelength.....	27
Figure 2.14. Comparison of solar irradiation at Istanbul (41,28) on 21 <sup>st</sup> March 2016, at 12:00 for tilt angles of 0°, 15°, 30° and 45°.....	28
Figure 2.15. Black body radiation of an object at 5850K at wavelengths 280 nm to 4000 nm.....	29
Figure 2.16. Visualization of steradian angle. Area of the blue segment is A and radius of the cone is r. Given that parameters, solid angle can be calculated as given in 2.23.....	30
Figure 2.17. Atmospheric transmission with from visible to middle infrared spectrum...30	30
Figure 2.18. Solar irradiance at (23,27) on 21 June 2016 at 12:00 is given as reference and compared with calculated solar irradiance.....	31
Figure 2.19. Solar irradiance at (41,28) on 21 March 2016 at 12:00 is given as reference and compared with calculated solar irradiance.....	32
Figure 2.20. Solar irradiance at (41,28) on 21 March 2016 at 12:00 is given as reference and compared with calculated solar irradiance with model which includes incidence angle parameter.....	33
Figure 2.21. Refractive index and extinction coefficient of GaAs with respect to wavelength.....	34
Figure 2.22. Spectral behavior of the GaAs layer with thickness of 100 nm on Si substrate.....	35
Figure 2.23. Refractive index and extinction coefficient of Ag with respect to wavelength.....	35
Figure 2.24. Spectral behavior of the Ag layer with thickness of 100 nm on Si substrate.....	36
Figure 2.25. Refractive index and extinction coefficient of SiC with respect to wavelength.....	36
Figure 2.26. Spectral behavior of the SiC layer with thickness of 100 nm on Si substrate.....	37
Figure 2.27. Refractive index and extinction coefficient of TiO <sub>2</sub> with respect to wavelength.....	37

Figure 2.28. Spectral behavior of the TiO <sub>2</sub> layer with thickness of 100 nm on Si substrate.....	38
Figure 2.29. Refractive index and extinction coefficient of Al <sub>2</sub> O <sub>3</sub> with respect to wavelength.....	39
Figure 2.30. Spectral behavior of the Al <sub>2</sub> O <sub>3</sub> layer with thickness of 100 nm on Si substrate.....	39
Figure 2.31. Refractive index and extinction coefficient of MgF <sub>2</sub> with respect to wavelength.....	40
Figure 2.32. Spectral behavior of the MgF <sub>2</sub> layer with thickness of 100 nm on Si substrate.....	40
Figure 2.33. Refractive index and extinction coefficient of SiO <sub>2</sub> with respect to wavelength.....	41
Figure 2.34. Spectral behavior of the SiO <sub>2</sub> layer with thickness of 100 nm on Si substrate.....	42
Figure 3.1. Atmospheric transmittance in the mid-infrared (8-13 μm) spectrum.....	44
Figure 3.2. Solar irradiance with respect to wavelength from visible to mid-infrared (280nm to 14 μm) spectrum.....	44
Figure 3.3. Ideal emissivity with respect to wavelength for a radiative cooling system.....	45
Figure 3.4. a) Emissivity of the design demonstrated in [42] from visible to near infrared spectrum. b) Emissivity of the same design from near infrared to mid-infrared.....	46
Figure 3.5. Visualization of radiative cooling design given in [42], which consists of seven thin film layers on top of a silver substrate.....	47
Figure 3.6. Emissivity graph of the partially imitated design given in [42] with respect to wavelength.....	48
Figure 3.7. Emissivity graph of the partially imitated design from which silver layer is excluded.....	49
Figure 3.8. Emissivity of the partially imitated design for incidence angles of 15°, 30°, 45° and 60° in a, b, c and d respectively.....	50
Figure 3.9. Schematic representation of structure of design II showing the changes from design I to design II.....	52
Figure 3.10. Comparison of emission curves of design I and II in 8-13 μm spectrum.....	53

Figure 3.11. Comparison of emission curves of design II with and without Al <sub>2</sub> O <sub>3</sub> layers.....	54
Figure 3.12. Comparison of emission curves for varying individual layer thicknesses of 100 nm, 200 nm and 300 nm in the triplets.....	54
Figure 3.13. Comparison of emission curves for varying number (multiples of number of triplets) of absorption layers whose individual layer thicknesses are 200 nm.....	55
Figure 3.14. Comparison of emission curves of systems, which has 3 absorption triplets with individual thicknesses of 200 nm, for varying incidence angles of 15°, 30°, 45° and 60° from ‘a’ to ‘d’ respectively.....	56
Figure 3.15. Emissivity curve of the second design at 40° incidence angle with 3 absorption triplets, each has individual layer thickness of 200 nm.....	57
Figure 3.16. Spectral behavior of the first design when Ag is defined as a layer on top of Si substrate.....	59
Figure 3.17. Spectral behavior of the first design when Ag layer is defined as the substrate.....	59
Figure 3.18. Comparison of structures of the previous designs and the new design. Third design is composed of more than one segment.....	60
Figure 3.19. Emissivities of the systems with number of layers of 6, 8, 10 and 12 at each segment for incidence angle of 0° for cases ‘a’, ‘b’, ‘c’ and ‘d’ respectively.....	62
Figure 3.20. Emissivities of the systems with 8 layers at each segment for incidence angles of 15°, 30°, 45° and 60° for cases ‘a’, ‘b’, ‘c’ and ‘d’ respectively.....	63
Figure 3.21. Emissivity curve of the third design at 40° incidence angle with 8 segments, each has 8 layers which are quarter wavelength thick.....	64
Figure 3.22. Emissivity curve of the third design at 40° incidence angle with 8 segments, each has 8 layers which are quarter wavelength thick and a 50 nm thick Ag layer at the bottom.....	66
Figure 4.1. ‘Transmittance Region’ is responsible for minimizing the reflection of incident wave from the surface of the multilayer system. In other words, it is used to maximize transmission to the multilayer system and it does not alter the transmittance response of the multilayer system. Since reflection from the surface of the multilayer system is decreased and transparency of it is not changed, it’s absorption should increase to satisfy Kirchhoff’s scattering law.....	69
Figure 4.2: Transmission graphs with respect to wavelength, for ripple magnitude 0.05 and 2 layers with center of wavelength 9.5, 10 and 10.5 μm air-Si interface.....	72

Figure 4.3. Transmission graphs with respect to wavelength, for ripple magnitude 0.05 and 3 layers with center of wavelength 9.5, 10 and 10.5 $\mu\text{m}$ air-Si interface.....	73
Figure 4.4. Transmission graphs with respect to wavelength, for ripple magnitude 0.05 and 4 layers with center of wavelength 9.5, 10 and 10.5 $\mu\text{m}$ air-Si interface.....	74
Figure 4.5. Transmission graphs with respect to wavelength, for center of wavelength 10 $\mu\text{m}$ and 2 layers with ripple magnitudes of 0.05, 0.15 and 0.25 air-Si interface.....	75
Figure 4.6. Transmission graphs with respect to wavelength, for center of wavelength 10 $\mu\text{m}$ and 3 layers with ripple magnitudes of 0.05, 0.15 and 0.25 air-Si interface.....	75
Figure 4.7. Transmission graphs with respect to wavelength, for center of wavelength 10 $\mu\text{m}$ and 4 layers with ripple magnitudes of 0.05, 0.15 and 0.25 for air-Si interface.....	76
Figure 4.8. Transmittance graphs with respect to wavelength of a design which has 10 $\mu\text{m}$ center of wavelength, 0.05 ripple magnitude and 3 layers with incidence angles of $15^\circ$ , $30^\circ$ , $45^\circ$ and $60^\circ$ from 'a' to 'd' with average performances of %99.83, %99.48, %97.93 and %94.14 respectively.....	77
Figure 4.9. Transmission graphs with respect to wavelength, for ripple magnitude 0.05 and 2 layers with center of wavelength 9.5, 10 and 10.5 $\mu\text{m}$ for air-TiO <sub>2</sub> interface.....	78
Figure 4.10. Transmission graphs with respect to wavelength, for ripple magnitude 0.05 and 3 layers with center of wavelength 9.5, 10 and 10.5 $\mu\text{m}$ for air-TiO <sub>2</sub> interface.....	78
Figure 4.11. Transmission graphs with respect to wavelength, for ripple magnitude 0.05 and 4 layers with center of wavelength 9.5, 10 and 10.5 $\mu\text{m}$ for air-TiO <sub>2</sub> interface.....	79
Figure 4.12. Transmission graphs with respect to wavelength, for center of wavelength 10 $\mu\text{m}$ and 2 layers with ripple magnitudes of 0.05, 0.15 and 0.25 for air-TiO <sub>2</sub> interface.....	80
Figure 4.13. Transmission graphs with respect to wavelength, for center of wavelength 10 $\mu\text{m}$ and 3 layers with ripple magnitudes of 0.05, 0.15 and 0.25 for air-TiO <sub>2</sub> interface.....	80
Figure 4.14. Transmission graphs with respect to wavelength, for center of wavelength 10 $\mu\text{m}$ and 4 layers with ripple magnitudes of 0.05, 0.15 and 0.25 for air-TiO <sub>2</sub> interface.....	81
Figure 4.15. Comparison of theoretical and realized design performances in which center of wavelength is 10.5 $\mu\text{m}$ , ripple magnitude is 0.05 and number of layers is two. In theory, average transmission in 8-13 $\mu\text{m}$ range is %93.44, whereas in realization it is %93.16.....	83

Figure 4.16. Comparison of theoretical and realized design performances in which center of wavelength is 10.5 $\mu\text{m}$ , ripple magnitude is 0.05 and number of layers is three. In theory, average transmission in 8-13 $\mu\text{m}$ range is %93.63, whereas in realization it is %93.29.....	84
Figure 4.17. Comparison of theoretical and realized design performances in which center of wavelength is 10.5 $\mu\text{m}$ , ripple magnitude is 0.05 and number of layers is three. In theory, average transmission in 8-13 $\mu\text{m}$ range is %92.92, whereas in realization it is %92.70.....	85
Figure 4.18. a) Reflectivity of quarter wavelength design with Ag combined with transmittance region, consists of 2 layers of $\text{MgF}_2$ and $\text{CaF}_2$ . Average reflection from 280 nm to 2.5 $\mu\text{m}$ is 99.20 and it is %14.29 in 8-13 $\mu\text{m}$ . b) Transmission to the substrate with respect to wavelength. c) Emission/Absorption of the design in which average emission in 8-13 $\mu\text{m}$ is 85.69. d) Summation of reflection, transmission and emission coefficients which equals to 1.....	86
Figure 4.19. a) Reflectivity of quarter wavelength design with Ag combined with transmittance region, consists of 3 layers of $\text{LiF}$ , $\text{CaF}_2$ and $\text{BaF}_2$ . Average reflection from 280 nm to 2.5 $\mu\text{m}$ is 99.29 and it is %13.89 in 8-13 $\mu\text{m}$ . b) Transmission to the substrate with respect to wavelength. c) Emission/Absorption of the design in which average emission in 8-13 $\mu\text{m}$ is 86.10. d) Summation of reflection, transmission and emission coefficients which equals to 1.....	87
Figure 4.20. a) Reflectivity of quarter wavelength design with Ag combined with transmittance region, consists of 4 layers of $\text{LiF}$ , $\text{MgF}_2$ , $\text{CaF}_2$ and $\text{BaF}_2$ . Average reflection from 280 nm to 2.5 $\mu\text{m}$ is 99.22 and it is %13.04 in 8-13 $\mu\text{m}$ . b) Transmission to the substrate with respect to wavelength. c) Emission/Absorption of the design in which average emission in 8-13 $\mu\text{m}$ is 86.94. d) Summation of reflection, transmission and emission coefficients which equals to 1.....	88

## List of Tables

Table 3.1. Rates of reflection and emission for various number of layers in the segments in different spectrum ranges.....	62
Table 3.2. Rates of reflection and emission for different incidence angles in different spectrum ranges.....	63
Table 4.1. Average transmission in 8-13 $\mu\text{m}$ spectrum for layer numbers of 2, 3 and 4 at center of wavelengths 9.5, 10 and 10.5 $\mu\text{m}$ , with ripple magnitude of 0.05 for air-Si interface.....	76
Table 4.2. Average transmission in 8-13 $\mu\text{m}$ spectrum for layer numbers of 2, 3 and 4 with the ripple magnitudes of 0.05, 0.15 and 0.25, with center of wavelength 10 $\mu\text{m}$ for air-Si interface.....	77
Table 4.3. Average transmission in 8-13 $\mu\text{m}$ spectrum for layer numbers of 2, 3 and 4 at center of wavelengths 9.5, 10 and 10.5 $\mu\text{m}$ , with ripple magnitude of 0.05 for air-TiO <sub>2</sub> interface.....	82
Table 4.4. Average transmission in 8-13 $\mu\text{m}$ spectrum for layer numbers of 2, 3 and 4 with the ripple magnitudes of 0.05, 0.15 and 0.25, with center of wavelength 10 $\mu\text{m}$ for air-TiO <sub>2</sub> interface.....	82
Table 4.5. Refractive indexes of BaF <sub>2</sub> , CaF <sub>2</sub> , LiF, MgF <sub>2</sub> and KCl for wavelengths of 9.5, 10 and 10.5 $\mu\text{m}$ which are going to be used in the realization of theoretical design of Chebyshev transformer.....	83

## List of Symbols and Abbreviations

- R: Reflection percentage of the system.
- $\epsilon$ : Absorption percentage of the system.
- T: Transmission percentage of the system.
- $N_0$ : Complex refractive index of the incident medium.
- $N_1$ : Complex refractive index of the thin film.
- $N_2$ : Complex refractive index of the substrate.
- $n$ : Real part of the complex refractive index (refractive index).
- $k$ : Complex part of the refractive index (extinction coefficient).
- $i$ : Complex number.
- $d$ : Physical thickness of a thin film.
- B: One of the elements of characteristic matrix of a multilayer thin film system.
- C: One of the elements of characteristic matrix of a multilayer thin film system.
- $\delta$ : Optical thickness of a thin film.
- $\eta$ : Optical admittance of a thin film.
- $\lambda$ : Wavelength.
- $\vartheta$ : Angle of refraction.
- $\theta_0$ : Incidence angle.
- TM: Transverse magnetic.
- TE: Transverse electric.
- s: Synonym of TE.
- p: Synonym of TM.
- $\gamma$ : Admittance of free space.

$r$ : Current layer number in a multilayer thin film.

$q$ : Number of layers in a multilayer thin film.

$n_H$ : Refractive index of the high index layer.

$n_L$ : Refractive index of the low index layer.

$n_S$ : Refractive index of the substrate.

$d_{High}$ : Physical thickness of the high index layer.

$d_{Low}$ : Physical thickness of the low index layer.

$\lambda_0$ : Wavelength of operation.

$P_{Cool}$ : Cooling power.

$I_{BB}$ : Black body radiation.

$h$ : Planck's constant.

$c$ : Speed of light.

$k$ : Boltzmann's constant.

$T$ : Temperature.

$P_{Rad}$ : Radiated power by a body.

$A$ : Surface area of a body.

$P_{Atm}$ : Absorbed power due to atmospheric thermal radiation.

$\epsilon_{Atm}$ : Emissivity of the atmosphere.

$T_{Amb}$ : Ambient temperature.

$P_{Sun}$ : Power radiated by sun.

$\theta_{Sun}$ : Incidence angle of the sun.

$P_{Cond+Conv}$ : Power loss due to conduction and convection.

- $h_c$ : Heat transfer coefficient which includes contributions from conduction and convection.
- $\Omega$ : Solid angle in steradians.
- $\Gamma_n$ : Reflection on the surface of the  $n^{\text{th}}$  layer in a multilayer system.
- $N$ : Number of layers in a multilayer thin film system.
- $\Gamma_m$ : Bound of the reflection ripples in Chebyshev transformation.
- $R_L$ : Impedance of air.
- $Z_n$ : Impedance of the  $n^{\text{th}}$  layer in a multilayer system.
- $\epsilon_r$ : Relative permittivity of  $r^{\text{th}}$  layer in a multilayer system.
- $\mu_r$ : Relative permeability of  $r^{\text{th}}$  layer in a multilayer system.

# 1 INTRODUCTION

Thin film coatings, which generally have thicknesses of a few micrometers, can be coated on selected substrates with a desired pattern or as a complete film layer [1], for various applications. Some of these applications are electronics [2-3], optics [4-5], sensors [6] and energy [7-9]. Depending on the application; metals, semiconductors and dielectrics can be coated as different geometrical structures. In this thesis, thin film structures are investigated for their interesting optical properties for potential use in energy applications. To understand optical response of the thin film structures for potential use as energy efficient coatings, interaction of waves with various coatings made of different thicknesses, layer numbers, and materials are of interest. Below we summarize those optical responses.

When an incident wave propagating in a medium comes into contact with another medium, the wave splits into 3 components upon contact. First, certain amount of the wave reflects from the surface of the adjacent medium. In other words, some part of the incoming wave does not able to pass to the adjacent medium and that part is called the reflected component. Secondly, the part that is not reflected from the surface of the adjacent medium passes to the adjacent medium and propagates in that medium, which is called transmitted component. However, not the entire transmitted component reach to the end of the adjacent medium, but losses may occur during the propagation. Those losses are the absorbed component. Kirchhoff's radiation law states that under thermal equilibrium, the emission and absorption can be related. Based on this, reflection, emission and transmission can be related as

$$R + \varepsilon + T = 1 \quad (1.1)$$

In equation 1.1, 'R' stands for the reflection, 'ε' for the emission and 'T' for the transmission coefficients of the object or surface. Since summation of those coefficients equals to 1, it means that incident wave is either reflected, transmitted, or absorbed. Although all materials reflect and transmits at different percentages, some of them may

not absorb the incident wave, or has negligible absorption, at certain spectrums. In that case, unreflected portion of the incident wave is transmitted. This condition can be expressed mathematically as

$$R + T = 1 \quad (1.2)$$

There are several factors that influence spectral behaviors of the materials, such as geometrical structure of the coating (only thickness of the layer when it is complete layer of film), optical properties of the material, incidence angle of the incident wave and wavelength of the incident light. Spectral responses of the thin film structures can be modified by changing these parameters. To design thin film structures with desired spectral properties for potential use in energy efficiency, various parameters need to be investigated. In the next section, previous studies about passive radiative cooling will be summarized by reviewing the related literature.

### **1.1. Literature Review**

Passive radiative cooling has been studied widely [10-13], by designing selectively emitting surfaces. Fundamental principles behind all passive radiative cooling techniques are similar and can be explained as follows. It is well-known fact that heat transfer occurs between objects which are at different temperatures. Based on this fact, heat transfer between an object on the surface of the earth and sky can occur when an object is exposed to sky. In that case, energy flow from the object to the sky begins and object starts to lose heat. However, amount of transferred energy is dependent on transparency of the atmosphere, since atmospheric transmittance is the connection channel between the object and sky. Due to the fact that emitted energy by the object is in the form of an electromagnetic wave, whether it reaches to sky or not is dependent on the atmospheric transmittance which stands as an intermediate medium between the sky and earth's surface. So, heat transfer will not take place in the spectral regions in which atmosphere is opaque. When this is considered, it can be stated that emission of the object has to be increased in the spectrums in which atmosphere is transparent and this is one of the reasons why selective emission is desired.

From the above explanation of radiative heat transfer mechanism between an object on the surface of the earth and sky, it is understood that object should emit energy in the spectrums in which atmosphere is transparent. However, when atmospheric transmittance is generated [14] from visible to mid-infrared spectrum starting from 300 nm to 13  $\mu\text{m}$ , atmosphere is highly transparent except around 5  $\mu\text{m}$  spectrum where it is opaque. In spite of this broadband transparency, selective emission would still be more beneficial in terms of efficiency. The reason for this claim is related to difference in the emitted energies with respect to wavelength and temperature. According to Planck's law [15], energy emitted by the objects depend on their temperature and wavelength. Figure 1.1, which contains the graph of blackbody radiations, based on Planck's law, at different temperatures with respect to wavelength, would be beneficial in terms of understanding the temperature and wavelength dependency.

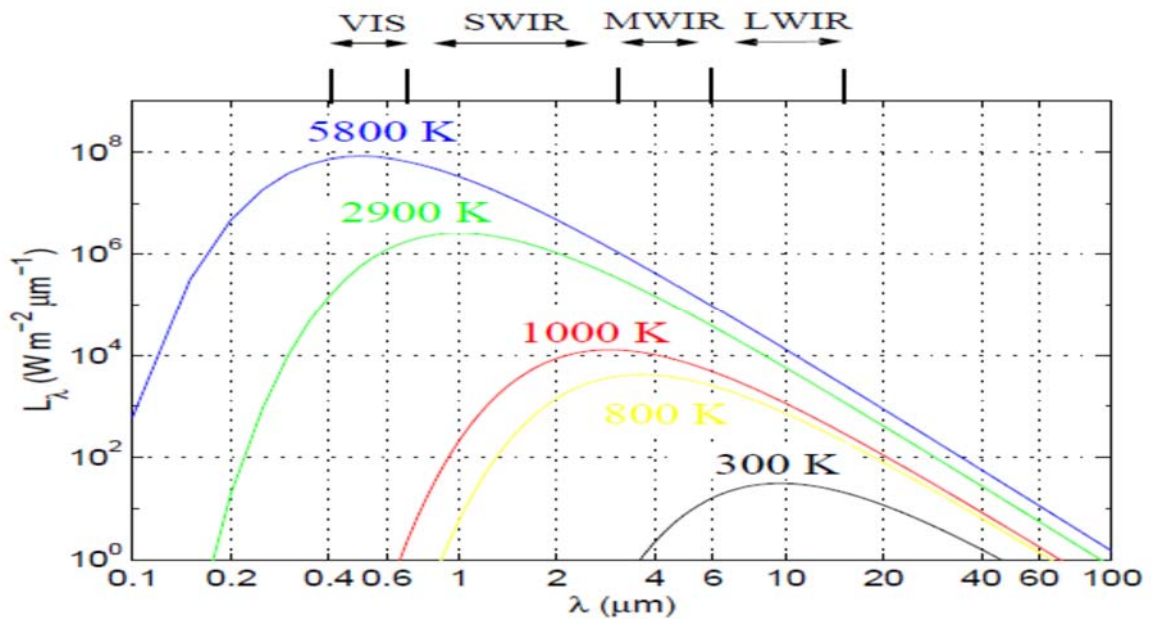


Figure 1.1. Blackbody radiation curves of different object's which are at temperatures 300, 800, 1000, 2900 and 5800K from 100 nm to 100  $\mu\text{m}$  spectrum.

As it can be seen from figure 1.1, blackbody radiation depends on both the temperature of the object and wavelength. This figure suggests that as temperature decreases, curves shift towards right. In other words, decrease in temperature results in presence of higher thermal radiation at longer wavelengths. For instance, when object at 300K is considered, its emission would be higher in 8-13  $\mu\text{m}$  than emission in 3-7  $\mu\text{m}$  spectrum. So, even if atmosphere is equally transparent in 300 nm to 13  $\mu\text{m}$  spectrum,

more energy would be transferred to the sky in 8-13  $\mu\text{m}$  spectrum, since objects, which have temperatures around 300K, has a peak in thermal radiation 8-13  $\mu\text{m}$  spectrum. Once influence of atmospheric transmittance and thermal radiation is understood, discussion about passive radiative cooling can be examined in more detail by illustrating different studies related to the field.

Passive radiative cooling designs can be divided into two sub groups in terms of design requirements based on operation time. More explicitly, design requirements change depending on whether the design is going to be used during daytime or nighttime. Radiative cooling during nighttime has been studied extensively [16-22] in the literature and high cooling performances are achieved. This is achieved by increasing emission in the 8-13  $\mu\text{m}$  spectrum, however emission maximization does not need to be necessarily restricted to 8-13  $\mu\text{m}$  spectrum but cooling performance can be improved by increasing the emissivity of the structure in the spectrums in which atmosphere is transparent. That is because there is not any external heat influx to the body, such as solar irradiance, in the electromagnetic spectrum during the nighttime. In the absence of such flux, selective emission is not a requirement but emissivity of the body can be maximized in a broadband spectrum to maximize the emission by the body, since there is not any energy to absorb, which would increase temperature of the body, during the nighttime.

Although passive radiative cooling during daytime is investigated [23-25], it is a relatively new research area when compared to radiative cooling during nighttime. Differently from radiative cooling during nighttime, an extra requirement rises for radiative cooling during daylight. Due to the presence of incident solar irradiation which is strong in the visible and near-infrared spectrums, radiative cooling cannot be achieved without reflection in those spectrums. Previously given studies use a foil made of ZnS, ZnSe or polymers and pigments which has reflection in the solar spectrum (visible and near-infrared) and transmission in 8-13  $\mu\text{m}$  range. However radiative cooling cannot be achieved in those cases, because overall reflection in the solar spectrum is reported to be below %85 percentage which still causes higher solar irradiance energy than overall thermal emission which is radiated to sky. Percentage of reflection is not a strict requirement, since lower reflection percentages can be balanced by thermal emission in 8-13  $\mu\text{m}$  spectrum. Only requirement is that the body should radiate more energy than it absorbs.

Once necessity of high reflection in the solar spectrum is understood, demand for radiative cooling designs that both reflect solar irradiance and emit radiation in the atmospheric transparency window rises. For that purpose, inspiring from the studies in the fields of thermophotovoltaics [26-28] and solar thermophotovoltaics [29-30] which use photonic structures that are able to either increase or decrease thermal emission of light in 2D [31-34] or 3D [35-39], new nanophotonic structures [40-42] are developed that satisfy necessary requirements for radiative cooling.

## **1.2. Contributions**

Aim of this thesis is to develop radiative cooling designs which are able to achieve cooling even in the presence of solar irradiance. Contributions of this thesis to future studies, as well as to the current literature are as follows:

- A more efficient model than commercial softwares, in terms of computation time, is implemented which is able to obtain spectral behaviors of 2D thin film structures.
- Solar irradiance data in the current literature is expanded from near-infrared to mid-infrared spectrum.
- It is shown that by including extra layers which composed of different materials, would cause tremendous performance improvement even without increasing overall thickness of system.
- By determining thicknesses of the periodically ordered high-low index dielectric layers, high reflection in the entire visible and near-infrared spectrum is achieved. This design method provides the opportunity of overcoming the performance limitation in the systems caused by metallic layers which are included to generate broadband reflection.
- Chebyshev transformation method, which is originally an impedance matching technique to increase transmission, is used to improve emission performance in 8-13  $\mu\text{m}$  spectrum by using materials that nearly do not emit in that spectrum. In that sense, it is a novel way of improving the design performance in this field.

### **1.3. Outline**

In chapter 2, theoretical model that is used to obtain spectral behavior of thin film structures is presented. After that, a design method which is derived from this model is shown. Heat dynamics between an object and its environment are discussed, and solar irradiance calculations are conducted. Incident solar energy is obtained with respect to location, time and wavelength (between visible and mid-infrared spectrums). Finally, optical behaviors of some materials are illustrated which are possible candidates for a radiative cooling design.

In chapter 3, studies related to design are given. First, a design given in the literature is evaluated as a benchmark for the other studies in the thesis. Here, the results are presented for comparison purposes to show that developed model is working properly. Then analysis is carried out by making slight changes to understand the dynamics of the optical behaviors and design method given in chapter 2 is implement and results of it are demonstrated.

Finally, in chapter 4 a design method, which is originally used to increase transmittance, is used to increase emission in the mid-infrared spectrum and results are illustrated. In the final chapter, conclusion is given which summarizes the important results of this thesis.

## 2 METHODOLOGY

In this chapter, we provide the details of the methods and models used in this thesis. First, we described the method that is used to obtain spectral behavior of multilayer thin film coatings. Next, a design method to obtain high reflection in the desired spectrum is demonstrated. This discussion is followed by examination of heat dynamics between an object and its environment. After that examination, methodology that is used to calculate incident solar irradiation based on the date and location from visible to mid-infrared spectrum is described. Finally, optical properties and spectral behaviors of different materials are illustrated to find out possible materials for radiative cooling applications.

### **2.1 Obtaining Reflectance, Absorption and Transmission of a Thin Film System with Characteristic Matrix\_Method**

When a wave, propagating in a medium, comes into contact with a thin film system, depending on the properties of the film some amount of the incident wave is reflected back to the incident medium, some amount is absorbed by the film and rest is transmitted through the film. Scheme for a single layer film on a substrate can be seen in figure 2.1.

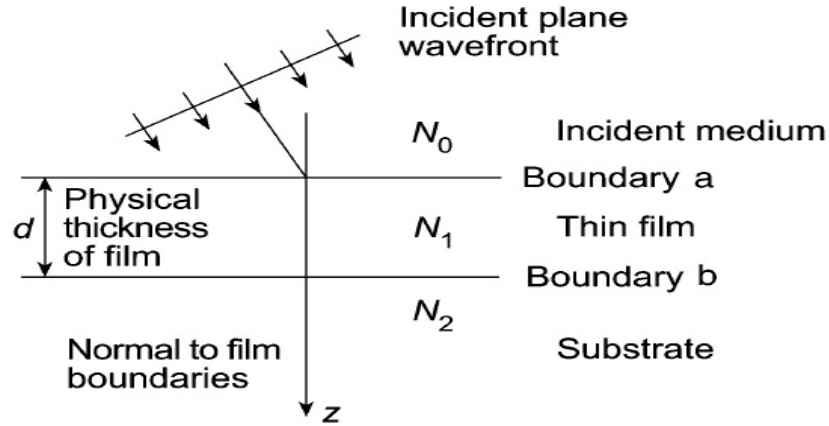


Figure 2.1. Scheme of a single layer coating on a substrate with incident medium.

In figure 2.1,  $N_0$ ,  $N_1$  and  $N_2$  stand for the optical properties (complex refractive index) of a material for incident medium, thin film and substrate respectively. Those parameters are defined in the form of 'n-ik', where 'n' and 'k' are the refractive index and extinction coefficient of the material and 'i' is the complex number. 'd' is the physical thickness of the thin film.

Fundamental parameters that affect the reflectance of a thin film are as follows: Optical properties of the incident medium, thin film and substrate material, thickness of the thin film and incidence angle of the wave which is the angle between the incident wave and normal of film boundary. In the case of normal incidence, perpendicular to the film, model is slightly simplified. Formulation for varying incidence angle is going to be demonstrated on the following sections. All those parameters appear in the formulation of spectral response of a thin film. All of the formulations are retrieved from [1].

Spectral behavior of a thin film can be obtained by using the characteristic matrix of it which is shown in equation 2.1.

$$\begin{bmatrix} B \\ C \end{bmatrix} = \begin{bmatrix} \cos \delta & (i \sin \delta) / \eta_1 \\ i \eta_1 \sin \delta & \cos \delta \end{bmatrix} \begin{bmatrix} 1 \\ \eta_2 \end{bmatrix} \quad (2.1)$$

In equation 2.1, right hand side is the characteristic matrix of a thin film. ' $\eta_1$ ' and ' $\eta_2$ ' are the admittances of film and substrate respectively. Admittance of air is denoted by ' $\gamma$ ' and equals to 1 in Gaussian unit system and admittance of any thin film layer can be obtained by multiplying admittance of air with ' $N$ ' of that layer when incidence angle is zero.

' $\delta$ ' is the optical thickness of the film and can be defined as in equation 2.2.

$$\delta = \frac{2\pi N d \cos \vartheta_1}{\lambda} \quad (2.2)$$

In equation 2.2, ' $\lambda$ ' is the wavelength of the incident wave and ' $\vartheta_1$ ' is angle of refraction in the film. When propagation direction is perpendicular to film, incident wave does not refract, so ' $\vartheta_1$ ' becomes equal to the incidence angle. However, when the angle of incidence is different than zero, angle of refraction needs to be calculated and method for that is going to be demonstrated in the following sections.

When characteristic matrix of a film is defined and coefficients ' $B$ ' and ' $C$ ' are obtained, reflectance, absorption and transmittance of the film can be calculated as follows:

$$R = \left( \frac{\eta_0 B - C}{\eta_0 B + C} \right) \left( \frac{\eta_0 B - C}{\eta_0 B + C} \right)^* \quad (2.3)$$

$$T = \frac{4\eta_0 \text{Re}(\eta_2)}{(\eta_0 B + C)(\eta_0 B + C)^*} \quad (2.4)$$

$$A = \frac{4\eta_0 \text{Re}(BC^* - \eta_2)}{(\eta_0 B + C)(\eta_0 B + C)^*} \quad (2.5)$$

To calculate reflectance, absorption and transmittance in a spectrum, above calculations are repeated for desired wavelengths.

As mentioned previously in this chapter, formulation of reflectance, absorption and transmission of a thin film is simplified slightly, when light propagates in a perpendicular direction to the film. Also it is stated that in this case, refraction angle does not change in the film layer but continues on its way in the same direction. However, this assumption is not valid usually and formulation has to be modified. Scheme that shows the incidence angle, ' $\theta$ ', can be seen in figure 2.2. Formulation for varying incidence angle is explained below.

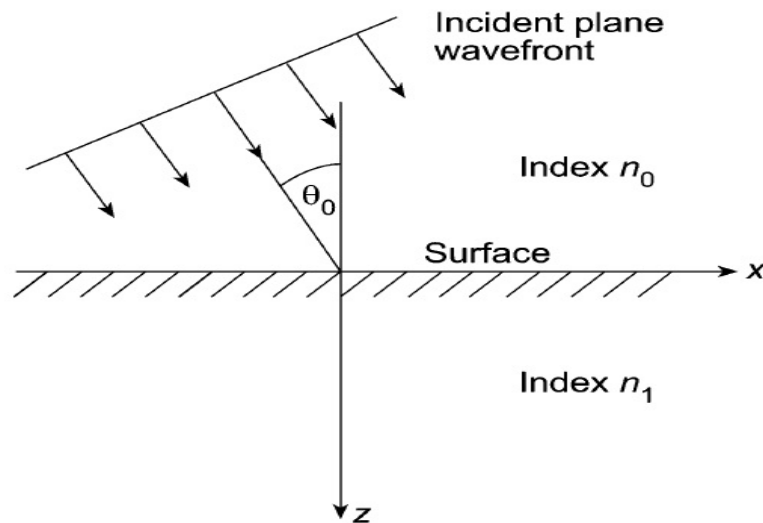


Figure 2.2. Incidence angle of an incoming wave propagating in a medium with index of  $n_0$  with respect to normal to the surface with refractive index of  $n_1$ .

In order to include the incidence angle, previous calculations are divided into two separate sections with respect to orientations of the incident wave. An incident wave vector has two orientations, one is on the plane of incidence, on the 'xy' plane of the scheme in figure 2.2, and other one is aligned normal to plane of incidence, parallel to 'y' axis in figure 2.2. Special name of the component that is on the plane of incidence is p-polarized or transverse magnetic (TM) and for the component that is aligned normal to plane of incidence is s-polarized or transverse electric (TE). So, calculations have to be carried out separately to obtain reflection, absorption and transmission coefficients with respect to wavelength for two polarizations.

Reason of including the polarization dependency can be explained as follows: When incident wave is perpendicular to film layer, both TE and TM polarizations yield same result for reflection, absorption and transmittance. However, when incidence angle is altered results vary with respect to different polarization components. That is because; optical admittance, ‘ $\eta$ ’, of the layer is changed in case of oblique incidence for different polarizations and relation can be given in following equations:

$$\eta_1 = \gamma N_1 \cos \vartheta_1 \quad \text{for } s - \text{polarizaion (TE)} \quad (2.6)$$

$$\eta_1 = \gamma N_1 / \cos \vartheta_1 \quad \text{for } p - \text{polarizaion (TM)} \quad (2.7)$$

From equation 2.6 and 2.7 it can be seen that when incidence angle is zero refraction angle in the corresponding layer is also zero then optical admittance of the layer is multiplication of ‘N’ of the film with admittance of air, since cosine of zero will yield 1. However, in the case of oblique incidence, refraction angle in the film will also vary and needs to be calculated. Admittance of the substrate can be calculated with the same equations, by replacing layer properties and refraction angle with the substrate’s.

Refraction angle in films, scheme is available in figure 2.3, can be calculated by exploiting the Snell’s law (or phase matching condition) which is given as follows:

$$N_0 \sin \vartheta_0 = N_1 \sin \vartheta_1 = N_2 \sin \vartheta_2 \quad (2.8)$$

From equation 2.8, refraction angle for the film and substrate can be calculated by using optical properties of the mediums and incidence angle.

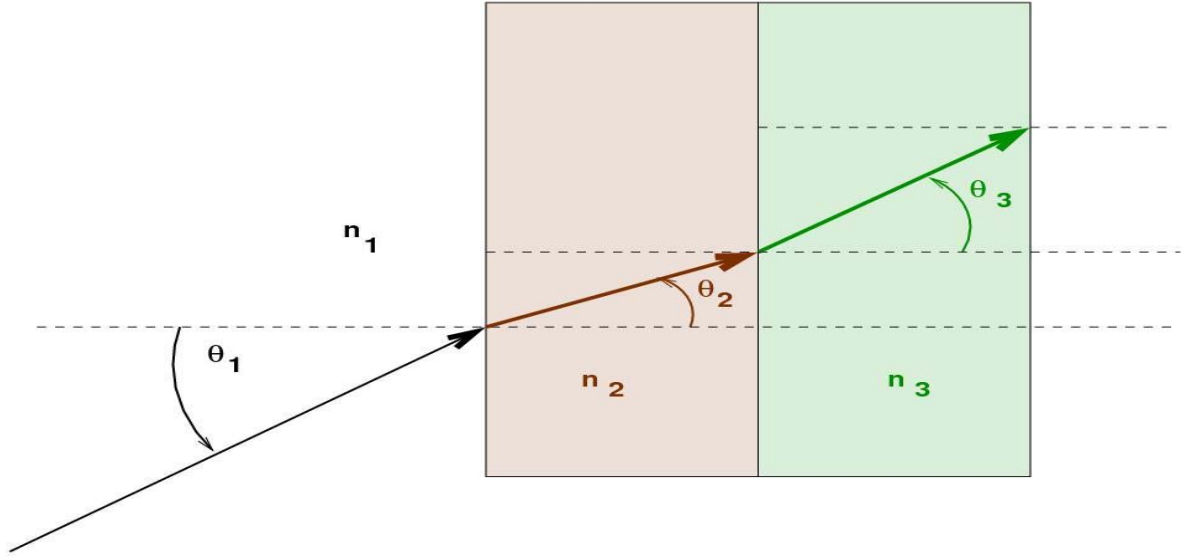


Figure 2.3. Representation of angle of refraction in different mediums.

In summary when incidence angle is not perpendicular to film, refraction angles in the film and substrate are needed to be calculated. Then optical admittances with respect to different polarization components have to be calculated. After that, characteristic matrix of the film can be formed for two different polarizations then reflection, absorption and transmission can be calculated for each polarization.

Until this point, single layer thin film on a substrate with varying incidence angle formulation is shown. For various applications, multilayer coatings are used and a formulation for a multilayer coating system is desired. For that purpose, previous formulation can be expanded to be used in a multilayer analysis.

In equation 2.1, 2x2 characteristic matrix for a single thin film layer is given in the right hand side of the equation. Combining it with the substrate admittance vector, required coefficients for calculating reflectance, absorption and transmission can be obtained. Modified version of that equation for multilayer coatings can be seen below.

$$\begin{bmatrix} B \\ C \end{bmatrix} = \left\{ \prod_{r=1}^q \begin{bmatrix} \cos \delta_r & (i \sin \delta_r) / \eta_r \\ i \eta_r \sin \delta_r & \cos \delta_r \end{bmatrix} \right\} \begin{bmatrix} 1 \\ \eta_m \end{bmatrix} \quad (2.9)$$

In equation 2.9, 'r' stands for the current layer number and 'q' is the total number of layers. Differently from the single layer version, substrate admittance is not denoted by a number but with 'm'. Starting from the first layer, adjacent to incident medium, characteristic matrix of each layer is formed and multiplied with each other until the substrate layer. Order is important in this case, meaning that q<sup>th</sup> layer is adjacent layer to the substrate. Finally, substrate layer is included in the end with admittance vector.

Same as before, in order to include incidence angle dependency in the formulation admittance of the layers are calculated separately based on polarization components. To do so, equation 2.6, 2.7 and 2.8 are modified as follows:

$$\eta_r = \gamma N_r \cos \vartheta_r \quad \text{for } s - \text{polarizaion (TE)} \quad (2.10)$$

$$\eta_r = \gamma N_r / \cos \vartheta_r \quad \text{for } p - \text{polarizaion (TM)} \quad (2.11)$$

$$N_0 \sin \vartheta_0 = N_r \sin \vartheta_r = N_m \sin \vartheta_m \quad (2.12)$$

Equation 2.6 and 2.7 are modified as in 2.10 and 2.11. In this case, admittance of each layer is calculated whereas it was calculated only for a single layer. Admittance of the substrate can be calculated in the same fashion, given in previous section. Refraction angles can be calculated based on Snell's law for each layer and substrate using the relationship with the incident medium. Once characteristic matrixes are formed and admittance of the substrate is calculated, formulation for obtaining reflection, absorption and transmittance is same with equation 2.3, 2.4 and 2.5.

## 2.2 Analysis of Characteristic Matrix and Quarter Wavelength Design

In chapter 2.2, characteristic matrix of a thin film layer is formed for varying incidence angle. Using the characteristic matrix of a thin film layer, its reflection, absorption and transmission can be calculated. The characteristic matrix of thin film layer can be considered as a design tool to manipulate the spectral behavior of a thin film layer on a specified substrate. Manipulation in this context means that engineering of spectral behavior of a thin film system, e.g. high reflection, transmission or absorption over a specified wavelength range. To achieve such a task, parameters that form the characteristic matrix have to be carefully studied.

Characteristic matrix parameters are optical thickness and admittance of the layer. Components of those parameters are wavelength, optical properties, geometrical thickness and incidence angle. Since the incident wave is coming at a fixed angle determined by external factors, remaining design tools are optical properties, geometrical thickness and wavelength of operation. To achieve a desired behavior (reflection, absorption or transmission) in a specified wavelength range, wavelength of operation is also determined in that range. In the end two design parameters are left, optical properties of the selected material and thickness of the coating.

Exploiting the fact that characteristic matrix of a thin film involves sine and cosine operations, characteristic matrix of a film can be simplified into a simpler form at certain optical thickness values. Relationship with the optical thickness at certain values and structure of characteristic matrix at those values can be seen as follows:

$$\delta = m \left( \frac{\pi}{2} \right) \text{ odd } m \xrightarrow{\text{yields}} \pm \begin{bmatrix} 0 & i/\eta \\ i\eta & 0 \end{bmatrix} \quad (2.13)$$

It can be seen that when optical thickness is odd multiple of  $\left(\frac{\pi}{2}\right)$ , characteristic matrix of the film simplifies into a form as in the right hand side of the expression 2.1. Given the formulation of optical thickness in chapter 2.2, ratio of the geometrical thickness and material based wavelength needs to be equal to  $\frac{1}{4}$ . In this case, optical thickness will be odd multiple of  $\left(\frac{\pi}{2}\right)$ . If layer in question is air, geometrical thickness can be set to quarter of wavelength of operation to satisfy optical thickness requirement of equation (2.1). However, depending on material properties, geometrical thickness has to be calculated such that, optical thickness will satisfy the given requirement.

Based on the form of optical thickness of a layer given in equation 2.13, high reflection around specified wavelength can be achieved by using alternate low and high index dielectric materials for which scheme can be seen in figure 2.4. When thickness of each layer is equal to quarter wavelength, reflected waves within the high index layers will not suffer any phase shifts whereas  $180^\circ$  of phase change will occur in waves that are reflected within low index layers. Because of that situation inner reflected components will not cancel each other; in fact, they will recombine constructively since they are all in same phase. As a result of that, high reflection in the front surface can be achieved.

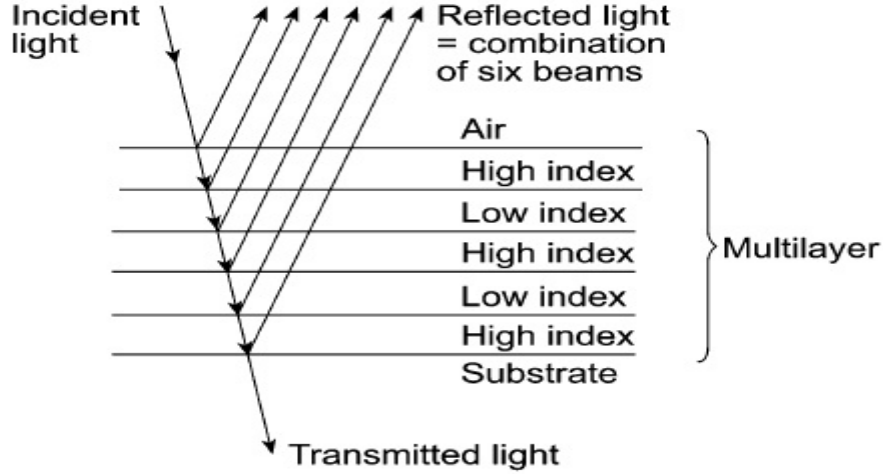


Figure 2.4. Demonstration of high-low index layered thin film coating system where each layer is quarter wavelength thick, which is used to achieve high reflection around operation of wavelength,  $\lambda_0$ .

Once physical reasoning behind the outcomes of this technique is explained, mathematical expressions that lead to this outcome is examined to understand the effect of design parameters in this special method. It is fairly easy to see that since layer thicknesses are quarter wavelength, geometrical thicknesses of the layers are already determined in this method. Using characteristic matrixes of the layers given in chapter 2.2, we end up with the reflection formula that is only valid for this case when outer layers are high index layers.

$$R = \left( \frac{1 - (n_H/n_L)^{2p} (n_H^2/n_S)}{1 + (n_H/n_L)^{2p} (n_H^2/n_S)} \right)^2 \quad (2.14)$$

In equation 2.14  $n_H$ ,  $n_L$  and  $n_S$  stand for refractive index of high index layer, low index layer and the substrate. ‘ $2p+1$ ’ is the number of layers. From the equation 2.14, it can be seen that contributing parameters are refractive indexes of the layers and the substrate as well as the number of layers. Three deductions can be made from this equation. First one is the fact that as the number of layer increases, reflection around operation of wavelength increases. So depending on the need, reflection can be increased by simply adding more layers which are quarter wavelength thick. Second deduction is the selection of the substrate. When most outer layers are high index layers, as the index of the substrate decreases, reflection increases again in the operation of wavelength. On the other hand, reverse scenario occurs when outer layers are low index layers. Final

inference is the influence of relation between layer indexes to amount of reflection. When the ratio of refractive indexes increases, reflection at the operation of wavelength goes up while number of layers remains same. So to achieve high reflection with less number of layers, ratio of the refractive indexes has to be selected as high as possible.

In order to test the quarter wavelength technique as well as the deductions given above, hypothetical materials are used as high and low index materials. Refractive index of first material is set to 2.75 which is considered as high index and other one is to 1.45 as the low index material. Refractive indexes of the materials are assumed to be constant with respect to wavelength, which is not valid for real materials generally. Also extinction coefficients are set to zero since model is valid only for dielectrics which do not have extinction coefficients, hence they are absorption free. Thickness of the layers are calculated as given in equation 2.15 and 2.16 which are derived from requirement given in equation 2.13.

$$d_{High} = \frac{m(\pi/2)\lambda_o}{2\pi n_{High} \cos \vartheta_r} \quad (2.15)$$

$$d_{Low} = \frac{m(\pi/2)\lambda_o}{2\pi n_{Low} \cos \vartheta_r} \quad (2.16)$$

When thicknesses are determined as in equation 2.15 and 2.16, characteristic matrix of layer will take the form given in 2.13. Inserting calculated thicknesses into characteristic matrixes of the layers and multiplying those one by one; spectral behavior of the overall system with respect to wavelength can be seen in figure 2.5. If extinction coefficients of the layers had been non zero, then thickness values would be complex numbers which is physically impossible. That is the reason why this technique is only valid for dielectrics.

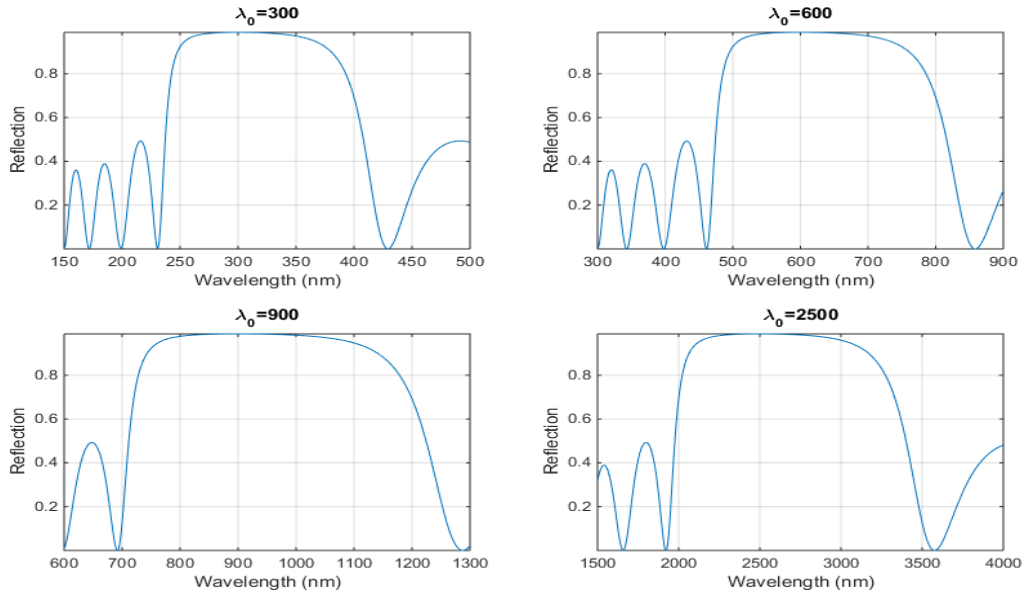


Figure 2.5. Reflections of high-low index layers each quarter wavelength thick 7 layers in total, where outer ones are high index layers, with different operational wavelengths.  $n_{\text{high}}$  is 2.75 and  $n_{\text{low}}$  is 1.45 and  $n_{\text{sub}}$  is 1.5. Operation of wavelengths are 300, 600, 900 and 2500 nm.

In figure 2.5, thicknesses are calculated such that requirement given in 2.13 is satisfied at 300, 600, 900 and 2500 nm wavelengths. As a result, reflection peaks are observed at those wavelengths.

In order to observe the influence of number of layers, same hypothetical materials are used again at an operation of wavelength with varying number of layers and results are compared in figure 2.6.

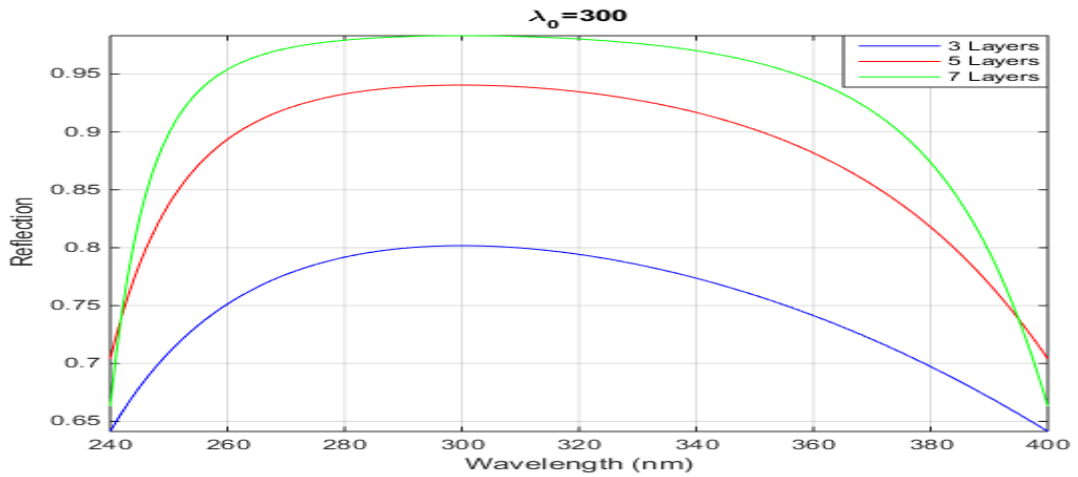


Figure 2.6. Reflections of high-low index layers, each quarter wavelength thick, consist of 3, 5 and 7 layers where outer ones are high index layers with 300 nm operation of wavelength where  $n_{low}$  is 1.45,  $n_{high}$  is 2.75 and  $n_{sub}$  is 1.5.

As mentioned above, as the number of layers in a stack increases overall reflection increases. In figure 2.6, claimed deduction is validated by observing increased reflection when number of layers are increased while everything else is kept constant.

Effect of the substrate can be seen in figure 2.7:

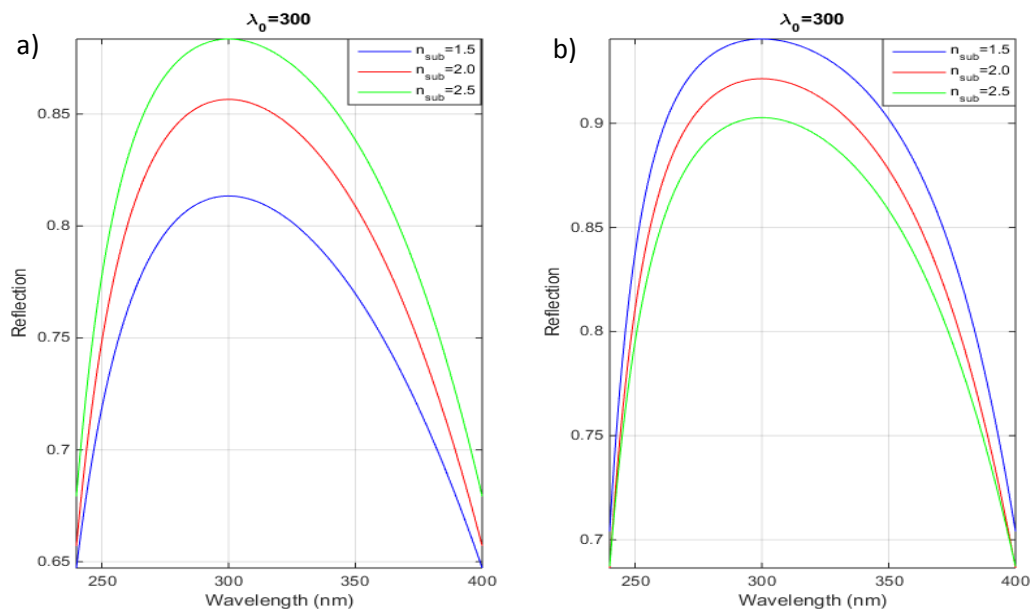


Figure 2.7. a) Reflections of high-low index layers, each quarter wavelength thick and outer layers are low index layers, with 300 nm of operation of wavelength where  $n_{low}$  is 1.45,  $n_{high}$  is 2.75. b) Only difference from 'a' is that outer layers composed of high index material. Indexes of substrates are set to 1.5, 2 and 2.5 in both 'a' and 'b'.

As previously stated, the effect of the substrate on overall reflection is dependent on the sequence of layers. If outer layers are high index layers then as the refractive index of the substrate increases, overall reflection increases. On the other hand, opposite scenario is valid when outer layers are not high index layers. In both case adjacent layer to incident medium is high index layer. However, results in the figure 2.7a belongs to system in which adjacent layer to the substrate is high index layer whereas for the results 2.7b, it is opposite. So, depending on the configuration of layer sequence, substrate selection can differ to enhance reflection around the operation of wavelength.

Influence of ratio of refractive indexes can be seen in figure 2.8 where ratio of refractive indexes is increased and results are compared.

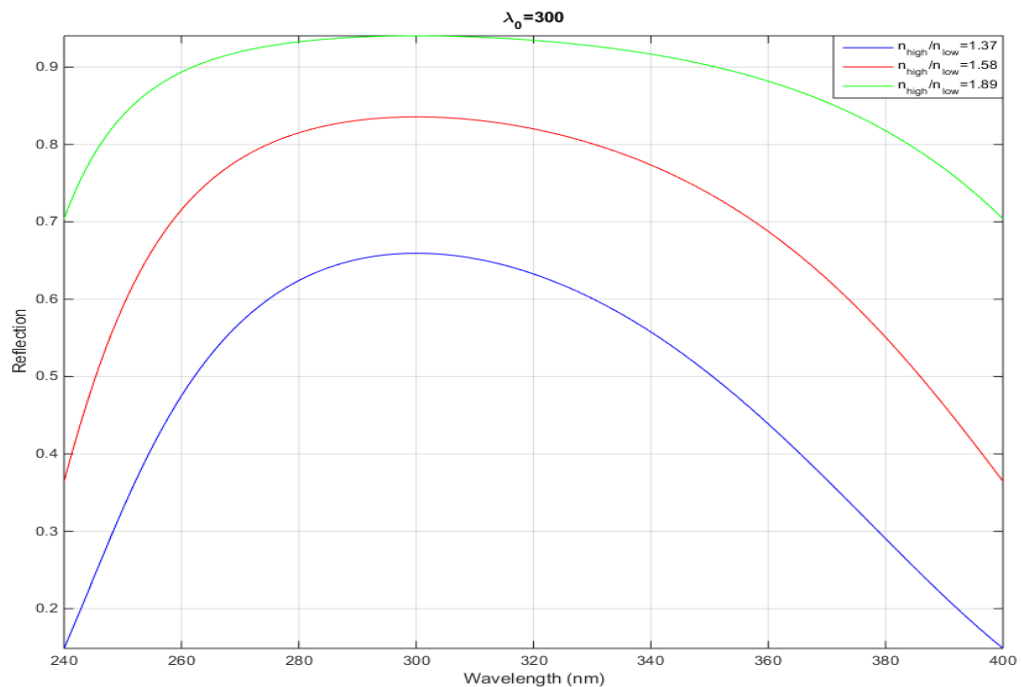


Figure 2.8. Reflections of high-low index layers, each quarter wavelength thick, 5 layers in total in which outer ones are high index layers, with 300 nm of operation of wavelength and  $n_{\text{sub}}$  is set to 1.5, ratio of  $n_{\text{high}}$  and  $n_{\text{low}}$  is set to 1.37, 1.58 and 1.89.

From figure 2.8, it can be seen that reflection at the wavelength of operation increases as the ratio of the refractive indexes increases as well as with the width of the reflection zone. These findings would be beneficial during the material selection for applications in which high reflection is desired.

Until this point factors that have an effect on the reflection magnitude at the operation of wavelength have been discussed with supportive results. However, when optical thickness is calculated such that it satisfies the given condition in equation 2.13, there is not a single peak of reflection, but many exist in the spectrum. This situation stems from the mathematical requirement given in 2.13. Optical thickness needs to be odd multiple of ' $\frac{\pi}{2}$ ' and this condition can be satisfied not only at wavelength  $\lambda_0$ , but at  $\frac{\lambda_0}{m}$  where m is equal to '1,3,5,...'. Given that, multiple high reflection zones can be observed at lower wavelengths. To observe that, reflection of periodic layers with different  $\lambda_0$  are plotted with respect to wider wavelength range in figure 2.9.

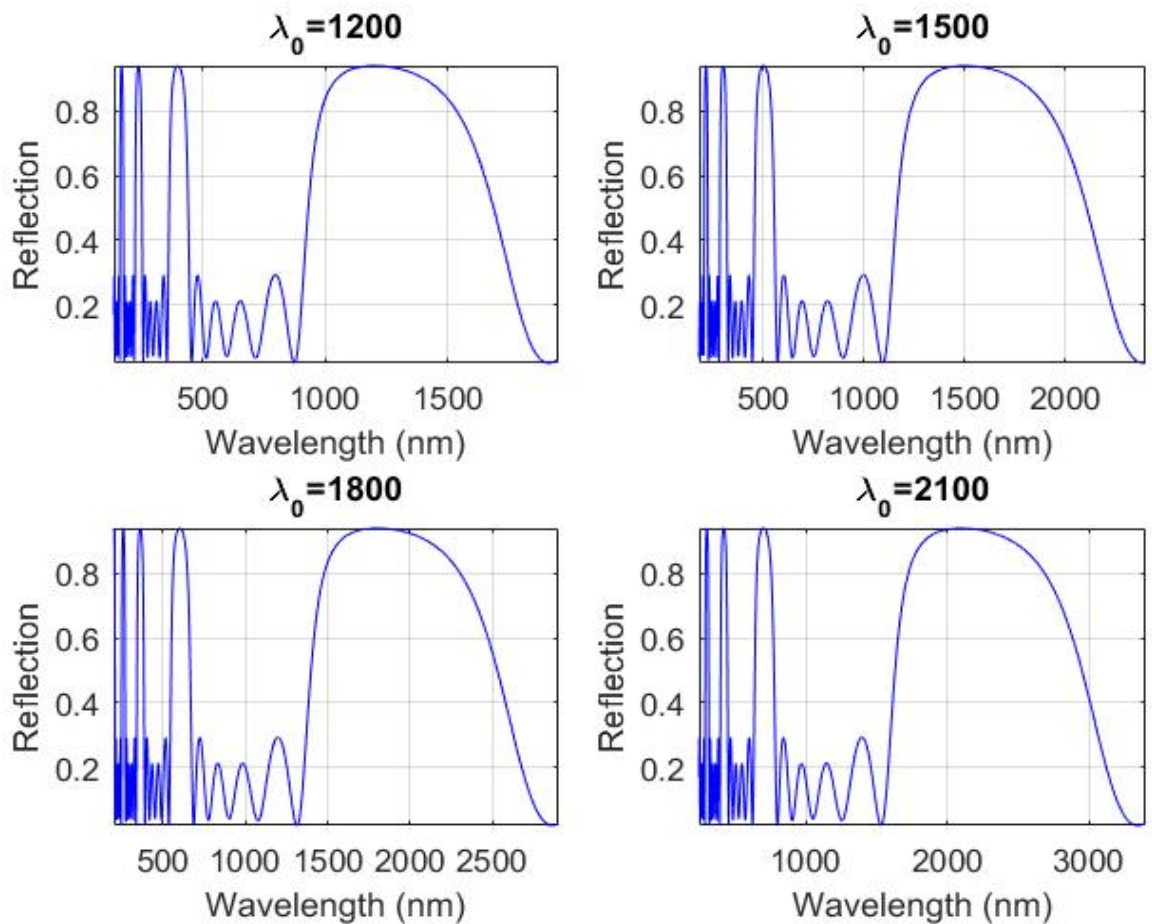


Figure 2.9. Reflections of high-low index layers, each quarter wavelength thick. Besides high reflection zones around  $\lambda_0$ s, each case have high reflection zones around  $\frac{\lambda_0}{3}$ ,  $\frac{\lambda_0}{5}$ ,  $\frac{\lambda_0}{7}$ .

From figure 2.9 it can be seen that multiple peaks can be seen in each case. Common part of this peaks is that, magnitudes of reflection at the peak wavelengths are same. However, bandwidth of the high reflection zone shrinks as peak wavelength decreases. This finding is important for spectral filter design, especially when broadband is considered. Because, although designed filter behavior satisfies the given requirement in a specified spectral range, it may violate requirements for lower wavelengths. Considering a case where high reflection is desired in near infrared region and high transmission is required in the visible spectrum. In that case, high reflection in near infrared can be achieved by quarter wavelength layers. However, that design causes reflection zones also in the visible spectrum which violates design specifications. Therefore, knowing the behavior of the designs in the spectrums for which it is not designed is essential.

### **2.3 Heat Balance**

Heat transfer occurs between objects that are at different temperatures. Heat is transferred through conduction, convection and radiation in the nature. Because of that, contribution of all transfer components has to be included in a comprehensive temperature analysis. Heat transfer finishes when temperature equilibrium is satisfied, in other words when temperature of the mediums or objects are equal.

Consider an object that is put into an open environment. When an object placed to an open environment all three components of heat transfer exists. There are different sources that bring heat to the object through conduction convection and radiation. In figure 2.10, contributions to heat balance of an object and its environment is demonstrated.

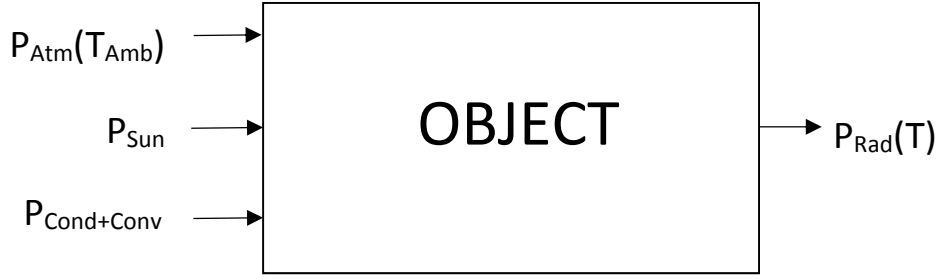


Figure 2.10. Heat balance scheme for an object in an open environment. Left side represents the contributions to heat inflow to the system and right hand side contains the heat outflow effects.

From figure 2.10, it can be seen that there are three components of heat inflow to the object and one outflow from the object. Since inflow and outflows can be expressed mathematically, heat balance equation can be defined as in equation 2.17.

$$P_{Cool} = P_{Rad}(T) - P_{atm}(T_{Amb}) - P_{Sun} - P_{Cond+Conv} \quad (2.17)$$

In equation 2.10, cooling rate of the object is defined in watts, since all components are in dimension of watts. If  $P_{Rad}(T)$  is higher than sum of other contributions than object starts to lose heat, since heat outflow will be higher. In other words, positive  $P_{Cool}$  means that object is losing heat, hence its temperature will decrease. On the other hand, its temperature will increase if  $P_{Cool}$  is negative.

In order to make numerical calculations related to heat equilibrium, components of it has to be formulated. Formulation is also essential in terms of understanding on what factors those components are dependent. By understanding those dependencies, necessary requirements for cooling to be occurred can be defined.

Before going into formulation of the heat equilibrium components, energy that an object radiates is required to be defined. That definition is important since, three out of four components of the equation 2.17 is related to radiation heat transfer which is related to radiation of the objects. Radiation of a special object that is called ‘black body’ can be defined as follows:

$$I_{BB}(T, \lambda) = \frac{2hc^2}{\lambda^5} \frac{1}{e^{hc/\lambda k_B T} - 1} \quad (2.18)$$

In equation 2.18, ' $I_{BB}$ ' is the black body radiation which is an object's radiation whose emissivity equals to 1. Other parameters can be defined as follows: ' $\lambda$ ' is the wavelength, ' $h$ ' is Planck's constant, ' $c$ ' is speed of light, ' $k_B$ ' is Boltzmann constant and ' $T$ ' is the temperature of the object. It can be seen that radiation of a black body depends on the wavelength and temperature of the object. After this definition, radiative heat transfer components can be defined as follows:

$$P_{rad}(T) = A \int_0^{\pi/2} 2\pi d\theta \sin \theta \cos \theta \int_0^{\infty} d\lambda I_{BB}(T, \lambda) \varepsilon(\lambda, \theta) \quad (2.19)$$

$P_{rad}(T)$  is defined as heat outflow from an object, which is the energy that object radiates to its surroundings. Radiation of any object can be calculated from multiplication of its emissivity, which is wavelength and angle dependent, and the black body radiation at temperature of the object. By that definition inner integrant is the radiation of an object at different wavelengths. To calculate object's radiation over a spectrum, it is integrated with respect to wavelength. Second integral is related to direction of the radiation. Since radiation of an object is not fixed to a single direction, but it is over a hemisphere in our case, object's radiation has to be integrated over a hemisphere. Finally, ' $A$ ' is the surface area of the object. When equation 2.19 is calculated, it results in  $P_{rad}(T)$  in dimension of watts.

$$P_{Atm}(T_{Amb}) = A \int_0^{\pi/2} 2\pi d\theta \sin \theta \cos \theta \int_0^{\infty} d\lambda I_{BB}(T_{Amb}, \lambda) \varepsilon(\lambda, \theta) \varepsilon_{atm}(\lambda, \theta) \quad (2.20)$$

In equation 2.20, expression for  $P_{Atm}(T_{Amb})$  can be seen.  $P_{Atm}$  stands for the energy that is absorbed due to atmospheric thermal radiation. Emissivity of the air can be defined as  $\varepsilon_{atm}(\lambda, \theta) = 1 - t(\lambda)^{1/\cos \theta}$  which is also wavelength and angle dependent as any object's emissivity. ' $t(\lambda)$ ' is the atmospheric transmittance which is defined in chapter 2.4 in detail. So, physical meaning of the inner integrant is the amount of absorbed thermal radiation by the object. So, equation 2.20 is similar to equation 2.19 except the inner integrant.

$$P_{Sun} = A \int_0^{\infty} d\lambda \varepsilon(\lambda, \theta_{Sun}) I_{AM1.5}(\lambda) \quad (2.21)$$

Equation 2.21 is the formulation of  $P_{Sun}$  which stands for the energy that reaches to earth's surface. ' $I_{AM1.5}(\lambda)$ ' is the radiation that sun makes at each wavelength which can be found in the literature numerically with respect to sun's position. Absorbed radiation by the object depends on its emissivity at the incidence angle of the sun. Again by integrating over the wavelength spectrum, energy inflow to the object caused by sun can be calculated.

$$P_{cond+conv}(T_{Amb}, T) = Ah_c(T_{Amb} - T) \quad (2.22)$$

Final component, the non-radiative one, of the heat balance equation is given in 2.22. In that equation, effects of conduction and convection is combined in a single heat transfer coefficient, ' $h_c$ ' and equation is developed accordingly. Conduction stems from physical interaction of the object with its environment and convection from the surrounding air.

Given the equations 2.19, 2.20, 2.21, 2.22 net cooling power can be calculated from the equation 2.17. Required parameters are surface area, temperature and emissivity of the object. However, only for equation 2.21, one extra parameter has to be considered which is  $I_{AM1.5}(\lambda)$ . Although there are sources for calculating the solar spectrum irradiance, they are restricted to visible and near infrared spectrums. To obtain irradiance in mid infrared spectrum, used methods are expressed in chapter 2.4.

## 2.4 Atmospheric Transmittance and Solar Irradiance

In section 2.3 it is stated energy that sun radiates, solar irradiance, has to be included in the cooling power calculations. To do so, amount of solar energy that reaches to earth has to be known. Amount of sunlight, so does solar irradiance, that reaches to earth is dependent on several factors. Without demonstrating related mathematical expressions, those factors are going to be explained conceptually. First, amount of the incident solar irradiance depends on the time of year, and latitude and longitude of the observation location.

In addition, time during day also has an influence due to rotary motion of the earth around itself. Because as the earth rotates around itself, position of any location with respect to sun changes. Influence of those motions alter two different angles which are related to position of the sun with respect to the earth. First one is the azimuth angle which is the compass direction from which sunlight is coming. Second one is the incidence angle in which sun's rays reach to the surface of the earth. A scheme in which azimuth and incidence angle are presented can be seen in figure 2.11. Incidence and azimuth angles are going to be used during the development of solar irradiation model.

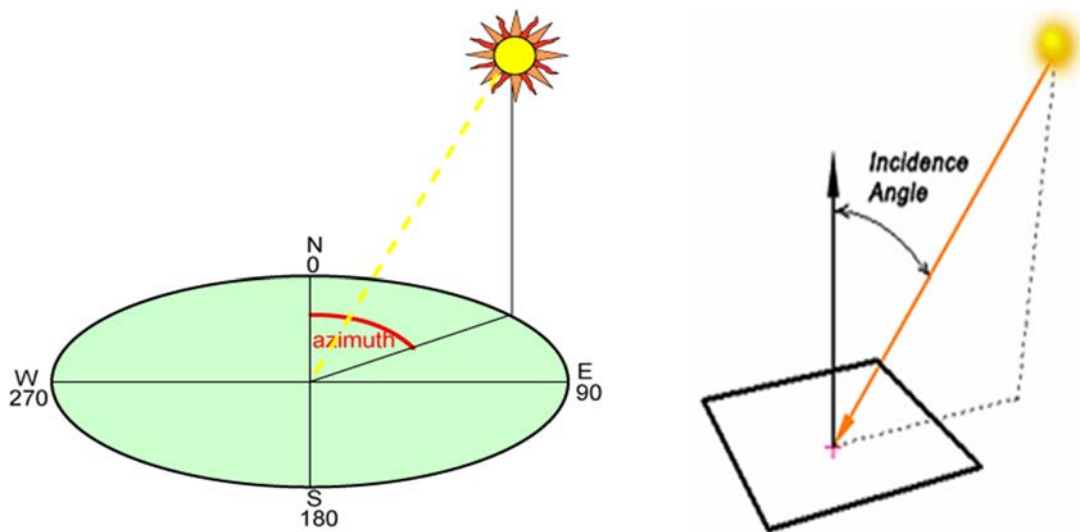


Figure 2.11. Representation of azimuth and incidence angles of the sun

An online calculator [43], whose source is  $I_{AM0}$  spectrum, is used to obtain solar irradiation for varying dates and locations. Inputs to the calculator are date, location in terms of latitude and longitude and orientation of the object on the earth. Outputs of the calculator are solar irradiation at each wavelength, as well as with azimuth and incidence angles. Based on that, solar irradiation is plotted with respect to wavelength for different conditions to observe the influencing factors. In figure 2.12, comparison of solar irradiances at a fixed location for different months can be seen.

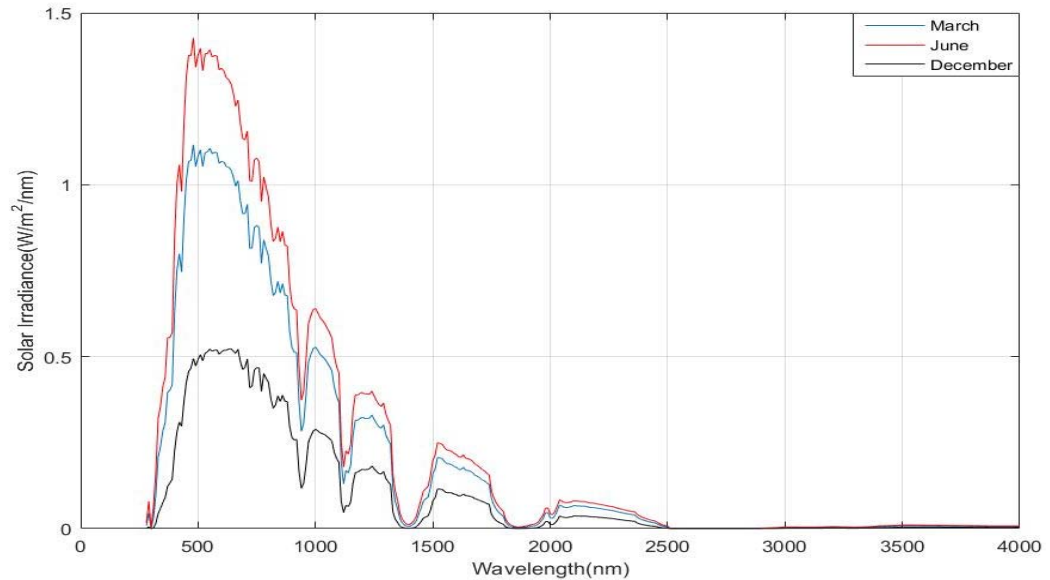


Figure 2.12. Comparison of solar irradiation at Istanbul (41,28) on March, June and December in 21<sup>st</sup> in 2016 with respect to wavelength.

From figure 2.12 it can be seen that solar irradiation varies significantly with respect to month at a fixed location. There is a considerable difference in solar irradiation on June when compared to March and December. On March azimuth angle is  $177.41^\circ$ , incidence angle is  $40.02^\circ$ , on June azimuth and incidence angles are  $178.48$  and  $17.57^\circ$  respectively and on December they azimuth angle is  $180.41^\circ$  and incidence angle is  $64.44^\circ$ . Based on those results, it can be seen that azimuth and incidence angles varies as month in a year changes. However, rate of change of incidence angle with respect to month in a year is higher when compared to azimuth angle.

In figure 2.13 effect of time on solar irradiation, on a day at a fixed location is shown:

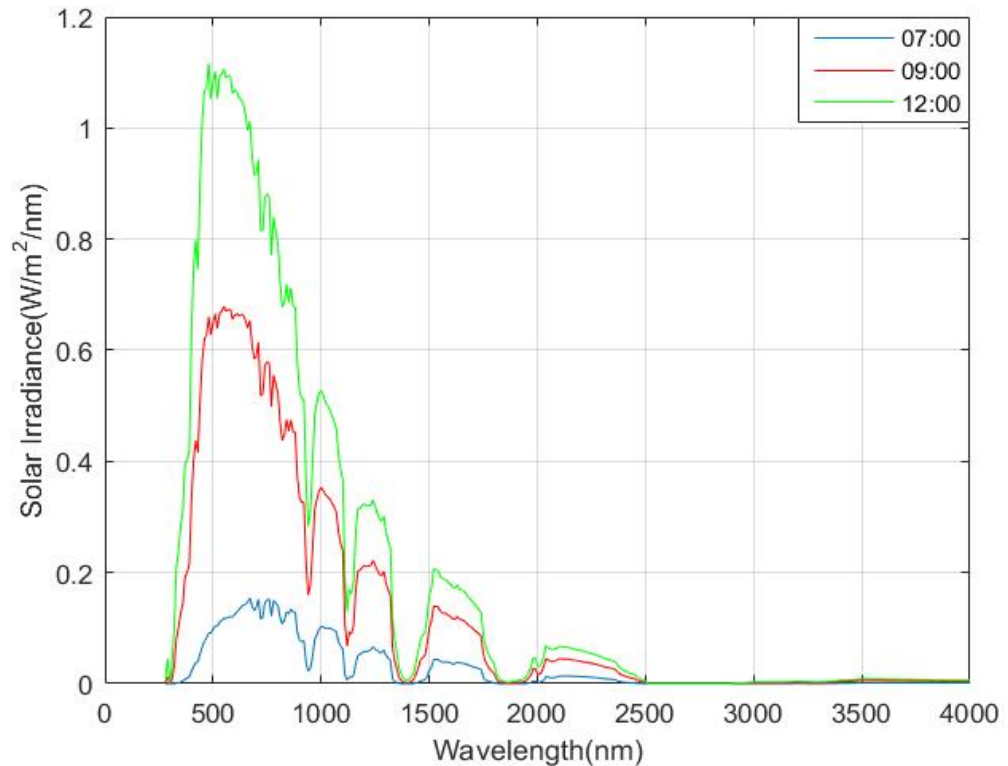


Figure 2.13. Comparison of solar irradiation at Istanbul (41,28) on 21<sup>st</sup> March 2016 at 7:00, 9:00 and 12:00 with respect to wavelength.

Results are almost identical to ones presented in figure 2.12. Time change in a day affects solar irradiance tremendously and alters azimuth and incidence angles. At 07:00 azimuth and incidence angles are  $98.12^\circ$  and  $79.37^\circ$ . They are equal to  $121.02^\circ$  and  $58.08^\circ$  at 09:00. Finally, at 12:00 they are  $1771.41^\circ$  and  $40.02^\circ$ . Until this point, factors that stem from motion of the earth is demonstrated which are date and time. However, as mentioned orientation of the object also has an effect on the incident solar irradiance.

Tilt angle which is used to define orientation of the object with respect to sun also has an impact on overall incident solar irradiation. Tilt angle has no effect on the azimuth angle, whereas it alters the angle of incidence. As the angle of incidence varies, amount of solar irradiance in a given location also varies. From figure 2.14, effect of tilt angle can be seen.

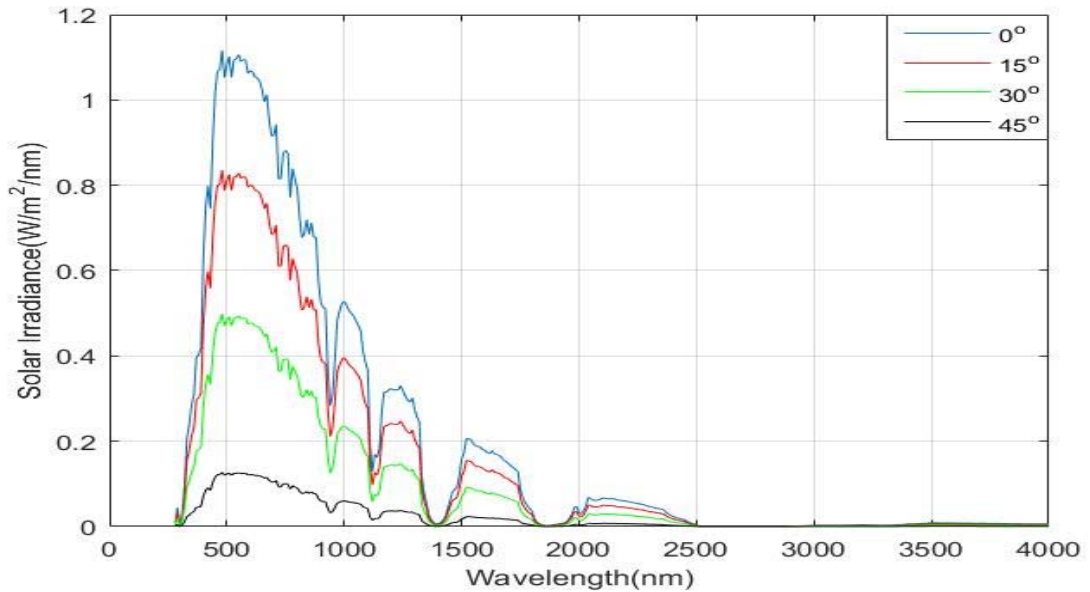


Figure 2.14. Comparison of solar irradiation at Istanbul (41,28) on 21<sup>st</sup> March 2016, at 12:00 for tilt angles of 0°, 15°, 30° and 45°.

In figure 2.14, tilt angle 0° means that object lies on the ground whereas it is perpendicular when angle is 90°. By looking at the results, it can be seen that as tilt angle increases solar irradiation decreases at a fixed location and time. Since, tilt angle does not have an effect on position of the earth with respect to sun, it does not alter the azimuth angle. So, azimuth angle remains at 177.41° whereas incidence angles are 40°, 55°, 70° and 85° for tilt angles 0°, 15°, 30° and 45°.

Incident solar irradiation with respect to different factors is demonstrated above. Sun radiates energy not only in visible and near infrared spectrums 280-4000 nm, but it also radiates in infrared spectrum. However, source that is used to generate above figures is limited to 4000nm. Although radiated energy decreases to very low amounts starting from 2500 nm when integrated over a wide wavelength range, e.g. until infrared spectrum, considerable amount of energy can be achieved. So, a study is conducted to develop a model that is able to estimate solar irradiance in wavelengths higher than 4000nm. Results given above provides a reference for the model. Once model is developed, results will be compared and if a good match could be achieved, then validity of the model would be verified and it would be used safely in longer wavelengths.

Development of model for solar irradiation starts with radiation formula given in chapter 2.3 equation 2.18. As mentioned in that chapter, any object radiates energy at different wavelengths based on its temperature and since point of interest is sun in this case, sun has to be modelled as an object with a temperature. Considering that sun can be modelled as a black body radiating at nearly 5850K. Plugging the temperature value into radiation formula and by specifying the wavelength radiation curve can be obtained as given in figure 2.15.

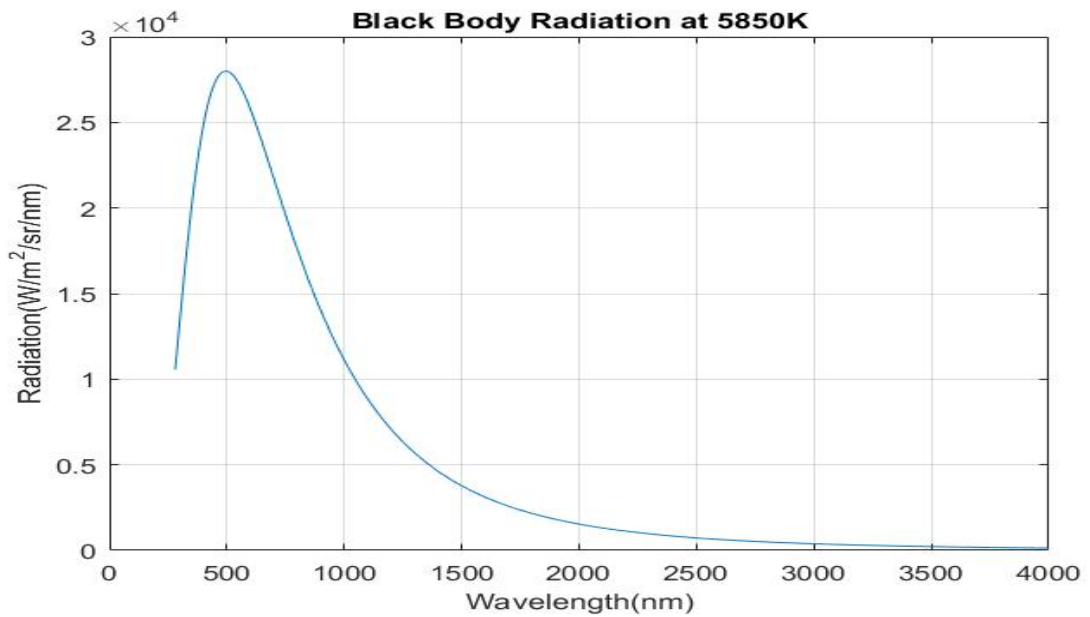


Figure 2.15. Black body radiation of an object at 5850K at wavelengths 280nm to 4000nm.

From figure 2.15, it can be seen that radiation at wavelengths higher than 2500nm is much lower when compared with smaller wavelengths. Although behavior of the radiation curve in figure 2.15 resembles with results in figure 2.12, 2.13 and 2.14 there is a big difference between the magnitudes. It can be seen that results in figure 2.12, 2.13 and 2.14 are in dimensions of  $Wm^{-2}nm^{-1}$  whereas dimension is  $Wm^{-2}sr^{-1}nm^{-1}$  in figure 2.15. The difference in dimensions is 'sr' factor which is solid angle in terms of steradians. Solid angle can be visualized as figure 2.16 and mathematical formulation of solid angle in steradians can be expressed as in equation 2.23.

$$\Omega = \frac{Area}{Distance^2} \quad (2.23)$$

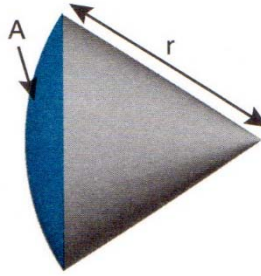


Figure 2.16. Visualization of steradian angle. Area of the blue segment is  $A$  and radius of the cone is  $r$ . Given that parameters, solid angle can be calculated as given in 2.23 [44].

Formulation given in 2.23 can be used to calculate solid angle of an object on the earth which receives radiation from the sun. Considering that radius of the sun is around 700,000 km and distance between the earth and the sun is given as 150 million kilometers, solid angle of a body on the surface of the earth is  $6.84 \times 10^{-5}$  [44]. So, results given in figure 2.15 have to be scaled with the calculated factor. However, there are also other parameters that have to be included in the solar irradiance formulation and one of them is the transmission of the atmosphere.

Earth is covered with atmosphere in which different gasses and particles are contained. Due to that containment, certain amount of incident solar irradiation is absorbed. Unabsorbed portion is transmitted to the surface of the earth. Transmission of the atmosphere with respect to wavelength generated by using ATRAN can be seen in figure 2.17.

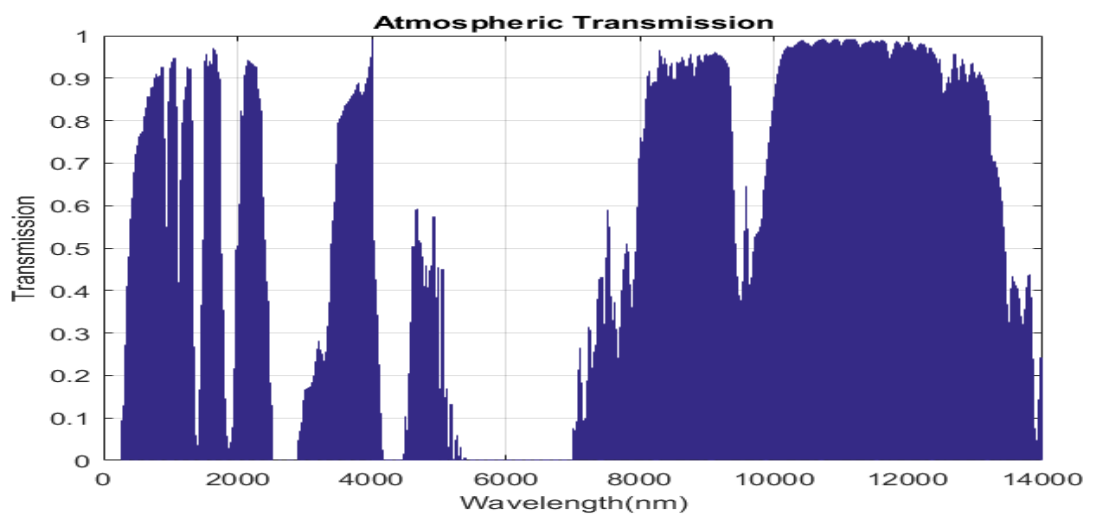


Figure 2.17. Atmospheric transmission with from visible to middle infrared spectrum.

Given in figure 2.17, it can be seen that atmosphere is not transparent in the entire solar spectrum. There are dips in visible and near infrared spectrum. It is also opaque around wavelength 6000 nm. Using this information as well as with 'sr' coefficient and multiplying it with black body radiation given in figure 2.15, results would be able to compete with reference values which is shown in figure 2.18.

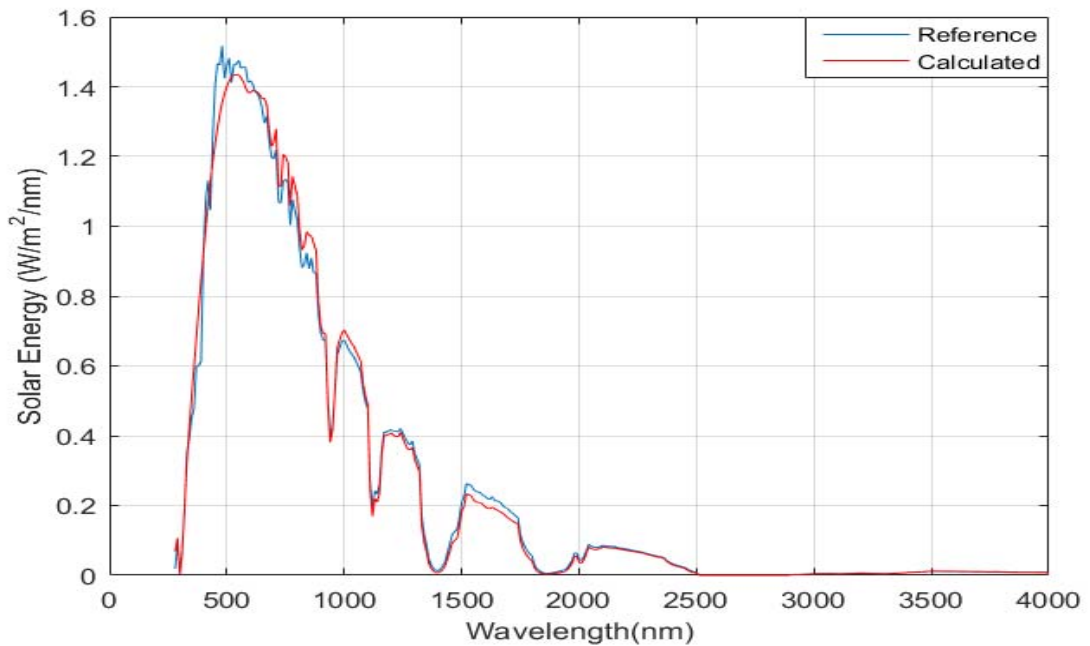


Figure 2.18. Solar irradiance at (23,27) on 21 June 2016 at 12:00 is given as reference and compared with calculated solar irradiance.

In figure 2.18, it is shown that there is a good match between the reference and model calculation in solar irradiation. On 21 June incidence angle of solar is almost perpendicular at 12:00 at (23,27) and azimuth angle is 46°. So, model is able to predict solar irradiation very accurately when compared with the reference in case of perpendicular incidence angle. Another comparison is made with solar irradiance at Istanbul (41,28) on 21<sup>st</sup> March 2016 at 12:00. Difference between the previous case is the altered incidence and azimuth angles. Results related to that case can be seen in figure 2.19.

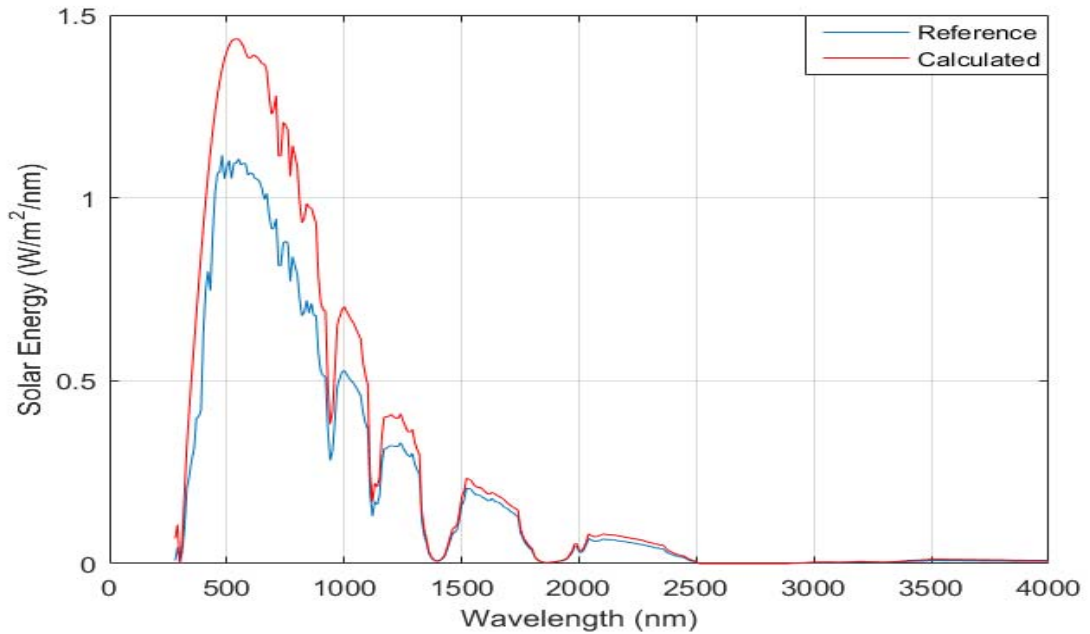


Figure 2.19. Solar irradiance at (41,28) on 21 March 2016 at 12:00 is given as reference and compared with calculated solar irradiance.

From figure 2.19, non-negligible amount of error between reference and model results can be observed. Reason for such error is that model does not contain any parameters related to relative position of the earth to the sun. As mentioned in the beginning of this chapter, azimuth and incidence angles are related relative position of the earth with respect to sun, however they are not included in the model. In order to obtain better matching between the model calculations and reference, incidence and azimuth angles have to be included.

When incidence angle included in the model as a multiple with cosine, obtained result can be seen in figure 2.20.

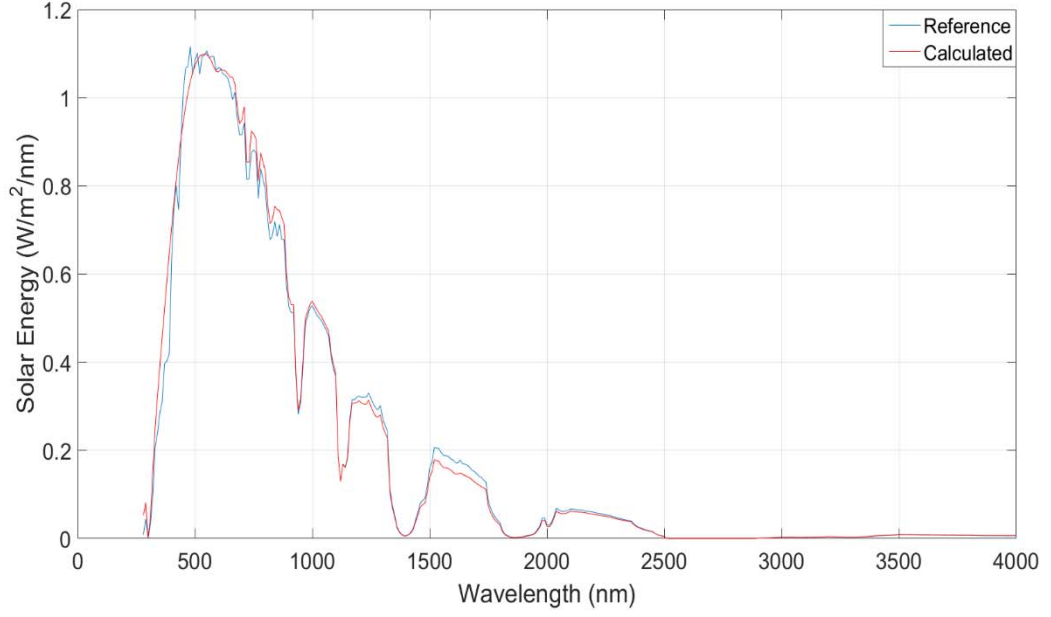


Figure 2.20. Solar irradiance at (41,28) on 21 March 2016 at 12:00 is given as reference and compared with calculated solar irradiance with model which includes incidence angle parameter.

From figure 2.20, it can be seen that including incidence angle in the model provides much better results when compared with the previous case. Once incidence angle is included, model adapts to changes of relative position of the earth with respect to sun. Although including azimuth angle in the formulation would provide better matching, current model still yields very good results, so it can be used safely during the irradiance calculations. Final version of the developed model can be seen in equation 2.24.

$$P_{Solar} = \frac{2hc^2}{\lambda^5} \frac{1}{e^{hc/\lambda kT} - 1} t(\lambda) \Omega \cos \theta_{Sun} \quad (2.24)$$

In equation (2),  $t(\lambda)$  is atmospheric transmittance,  $\Omega$  is steradian coefficient and  $\alpha$  is incidence angle. In conclusion by using formulation given in (2), incident solar irradiation on earth any location can be calculated approximately by knowing the incidence angle, which can be found in [43]. Once development of the formulation is calculated, incident solar irradiation on 21 March 2016 at 12:00 from visible to mid-infrared spectrum is around 950 Watts. This finding is going to be used during the performance evaluations of radiative cooling designs given in chapter 3.

## 2.5 Investigation of Material's Spectral Behaviors for Radiative Cooling

As mentioned in chapter 2.1 spectral behaviors of the materials are dependent on their optical properties. In this chapter, potential materials are examined for the design method given in chapter 2.2 and for radiative cooling applications. As going to be mentioned in chapter 3, a design for radiative cooling application has to reflect strongly in the visible and near infrared spectrum and it also needs to strongly emit in the mid infrared spectrum.

In all of the following demonstrations, a system with single layer material which has thickness of 100 nm on a silicon substrate is analyzed from visible to mid-infrared spectrum to check whether spectral behavior of the material is appropriate for radiative cooling. Optical properties of the materials are taken from [45], unless otherwise stated. In figure 2.21, refractive index ' $n$ ' and extinction coefficient ' $k$ ' of GaAs is shown.

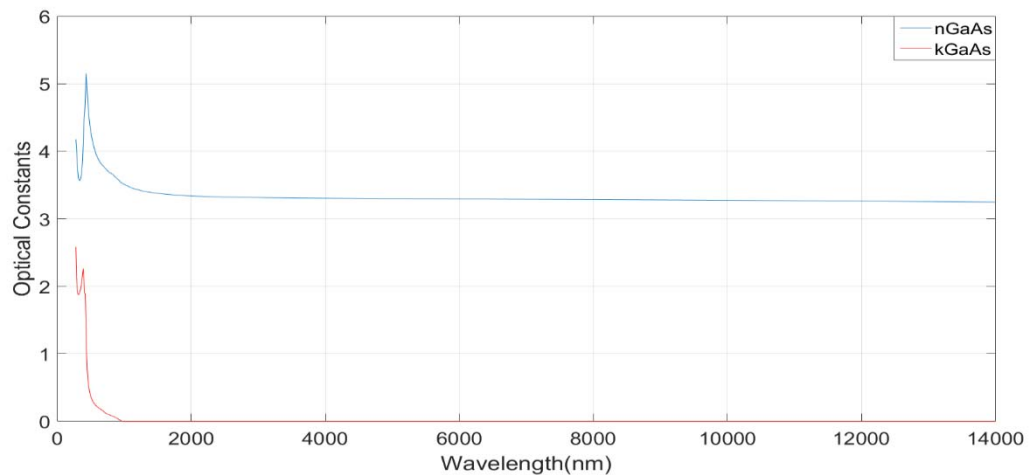


Figure 2.21. Refractive index and extinction coefficient of GaAs with respect to wavelength.

As it can be seen from figure 2.21, GaAs has high refractive index over a broad spectrum and this makes it a potential candidate for high-low index design. Although it has extremely low extinction coefficient at wavelengths longer than 1000 nm, it has relatively high extinction coefficient in the visible spectrum which causes absorption. Since absorption in the visible spectrum should be avoided strictly, GaAs would not be a proper choice. In figure 2.22, spectral behavior of the GaAs is shown.

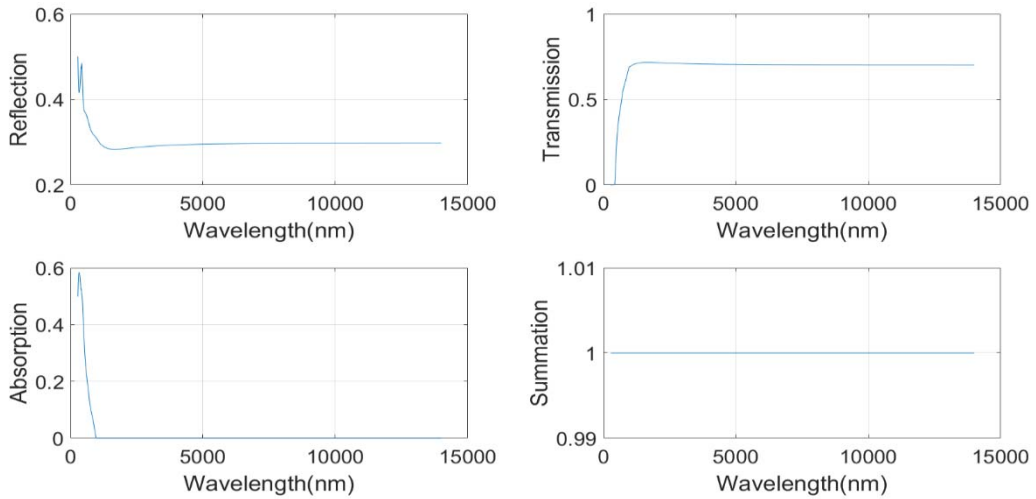


Figure 2.22. Spectral behavior of the GaAs layer with thickness of 100 nm on Si substrate.

As shown in figure 2.22, nearly %60 percentage of incident light is absorbed at most by GaAs in the visible spectrum where high amount of solar energy is stored as mentioned in chapter 2.4.

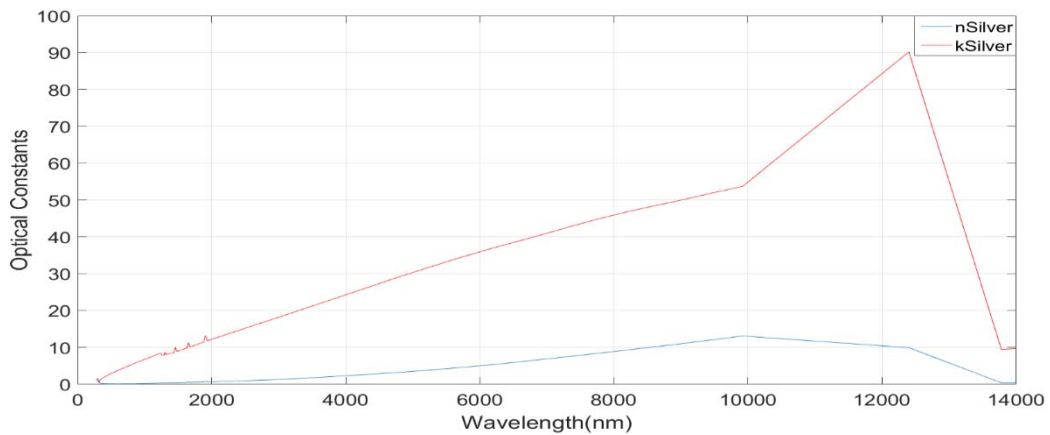


Figure 2.23. Refractive index and extinction coefficient of Ag with respect to wavelength.

Ag has high refractive index, as GaAs, in near infrared spectrum whereas it has low index in the visible spectrum. Due to the presence of extinction coefficient in a wide spectrum, which can be seen in figure 2.23, Ag causes absorption in that spectrum. In figure 2.24, spectral behavior of a silver layer can be seen.

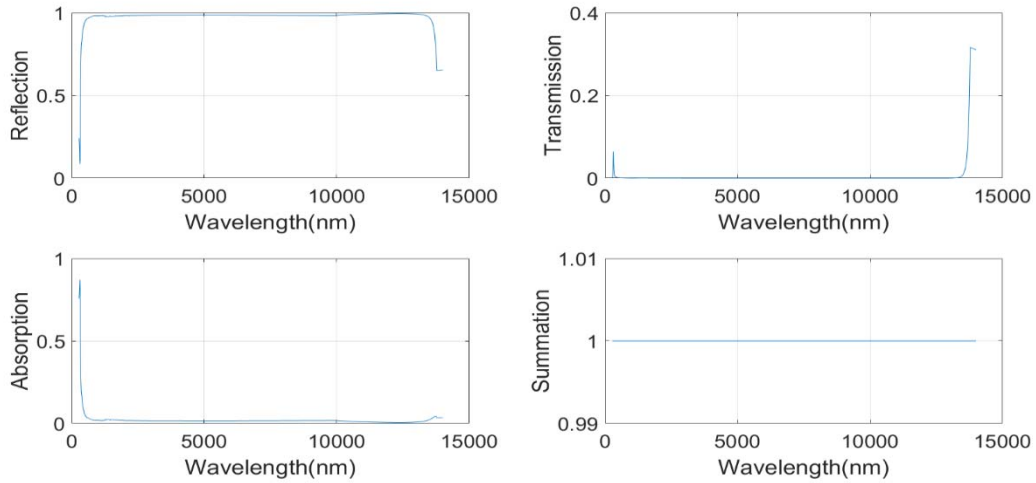


Figure 2.24. Spectral behavior of the Ag layer with thickness of 100 nm on Si substrate.

Although Ag provides a broadband reflection from visible to mid infrared spectrum, it has high absorption, which reaches to nearly %80 percentage and decreases slowly in the visible spectrum. Behavior of absorption is almost identical to GaAs. Advantage of the Ag over GaAs is the high reflectance of Ag over a large spectrum. Another high index material is SiC, whose optical properties are shown in figure 2.25.

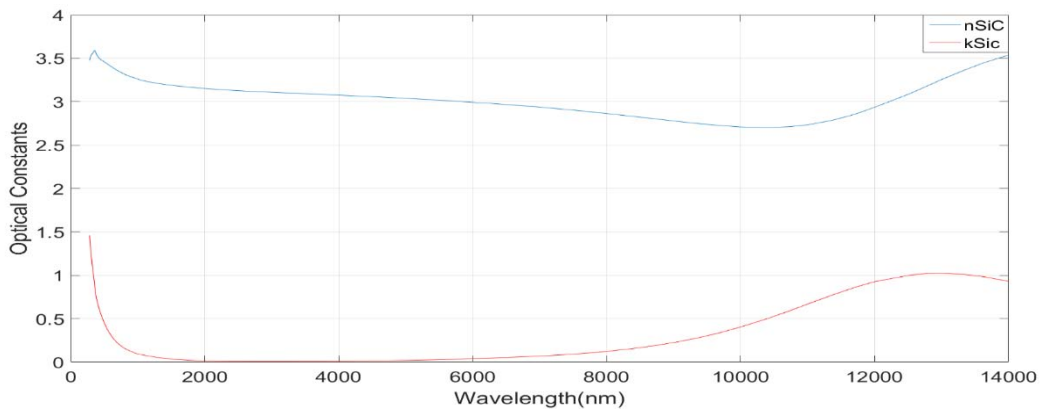


Figure 2.25. Refractive index and extinction coefficient of SiC with respect to wavelength.

Optical properties of SiC, which are retrieved from [46], can be seen in figure 2.25. It has high refractive index as GaAs over a broadband spectrum. Also it absorbs in the mid infrared spectrum due to non-zero extinction coefficient, which is essential for radiative cooling as stated in chapter 3. However, problem with SiC is the presence of extinction coefficient in the visible spectrum similar to GaAs and Ag. Spectral behavior of SiC is shown in figure 2.26.

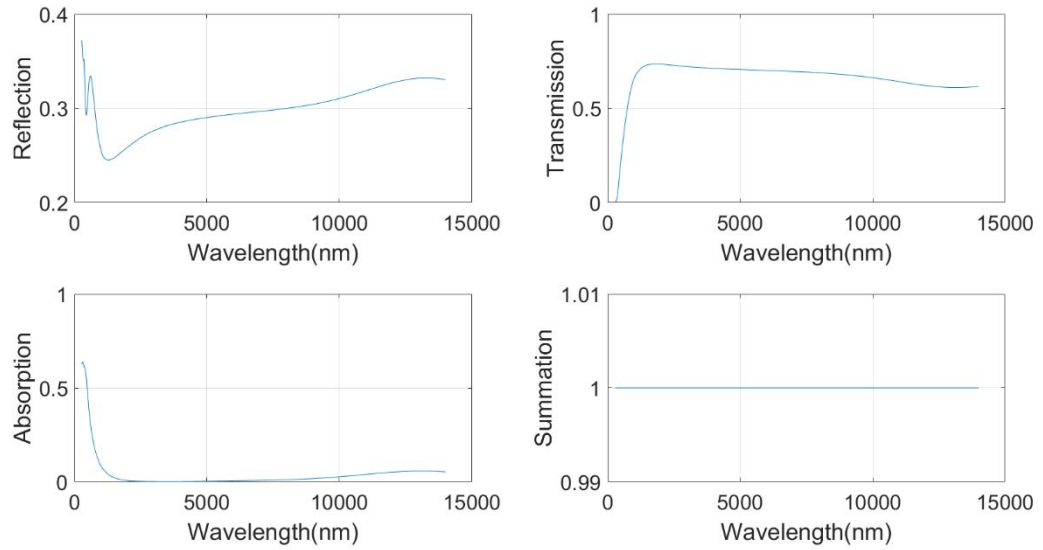


Figure 2.26. Spectral behavior of the SiC layer with thickness of 100 nm on Si substrate.

Absorption behavior of the SiC can be seen in figure 2.26. If SiC had not absorbed in the visible spectrum, it would be a great material for radiative cooling purposes. Because, it has nearly no absorption in near infrared until mid-infrared spectrum. It starts to emit in the mid-infrared spectrum which is important for radiative cooling applications as mentioned above.

Optical properties of the last high index material that is going to be demonstrated in this chapter, TiO<sub>2</sub>, can be seen in figure 2.27.

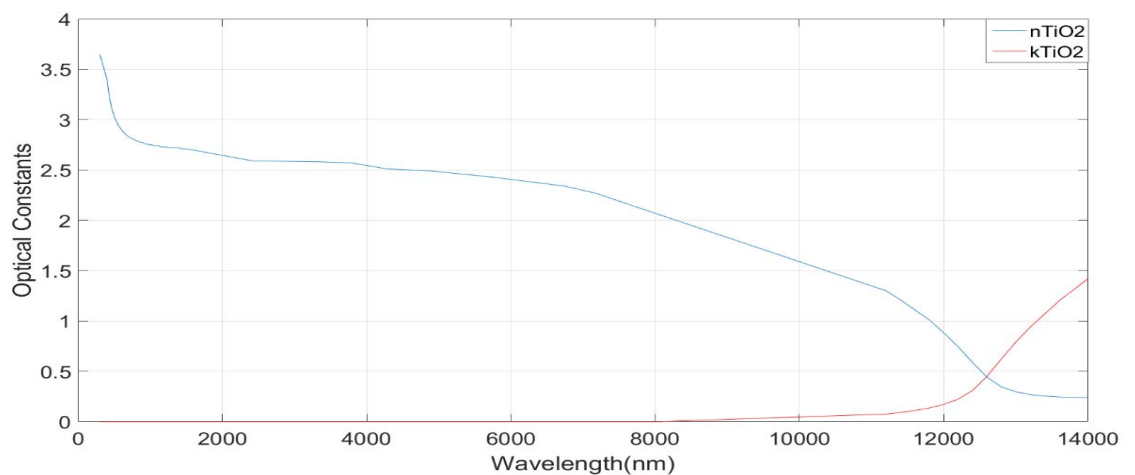


Figure 2.27. Refractive index and extinction coefficient of TiO<sub>2</sub> with respect to wavelength.

From figure 2.27 it can be seen that  $\text{TiO}_2$  has high refractive index in the visible and near infrared spectrum with extremely low extinction coefficient. Due to the absence of extinction coefficient it does not cause absorption in that spectrum. In addition to this extinction coefficient starts to increase in the mid-infrared spectrum which causes emission.

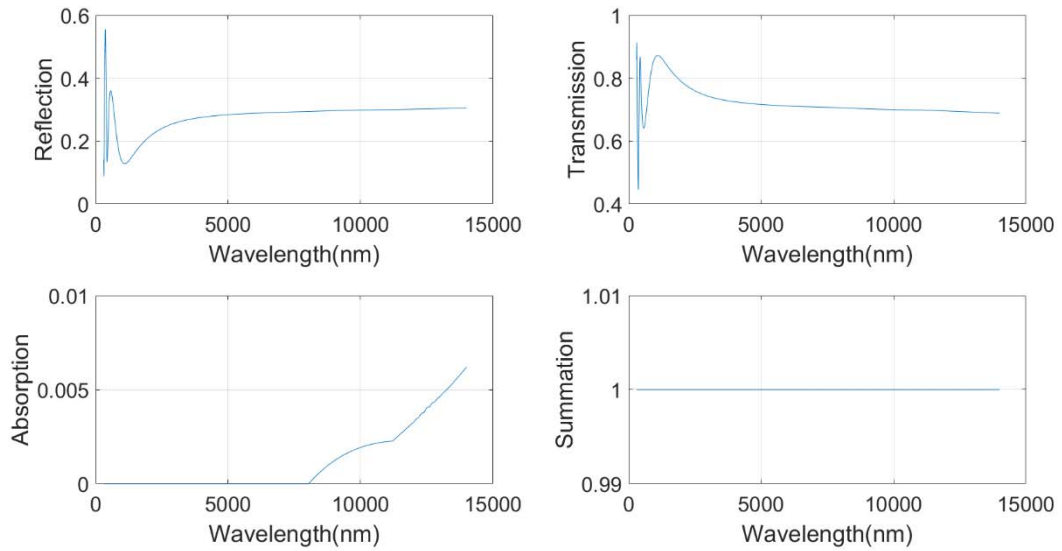


Figure 2.28. Spectral behavior of the  $\text{TiO}_2$  layer with thickness of 100 nm on Si substrate.

From figure 2.28, it is shown that  $\text{TiO}_2$  causes no absorption in the visible and near infrared spectrum. It also starts to absorb in the mid-infrared spectrum. Due to this spectral behavior  $\text{TiO}_2$  becomes a great choice in radiative cooling applications.

Until now, some high index materials are explored by analyzing their spectral behavior. Those materials, except silver since it has non zero extinction coefficient in the spectrum of interest, can be used as high index materials in the design method given in chapter 2.2. In the rest of this chapter, properties of some low index materials are going to be demonstrated as well as with their spectral behavior. In figure 2.29, optical properties of  $\text{Al}_2\text{O}_3$  is shown.

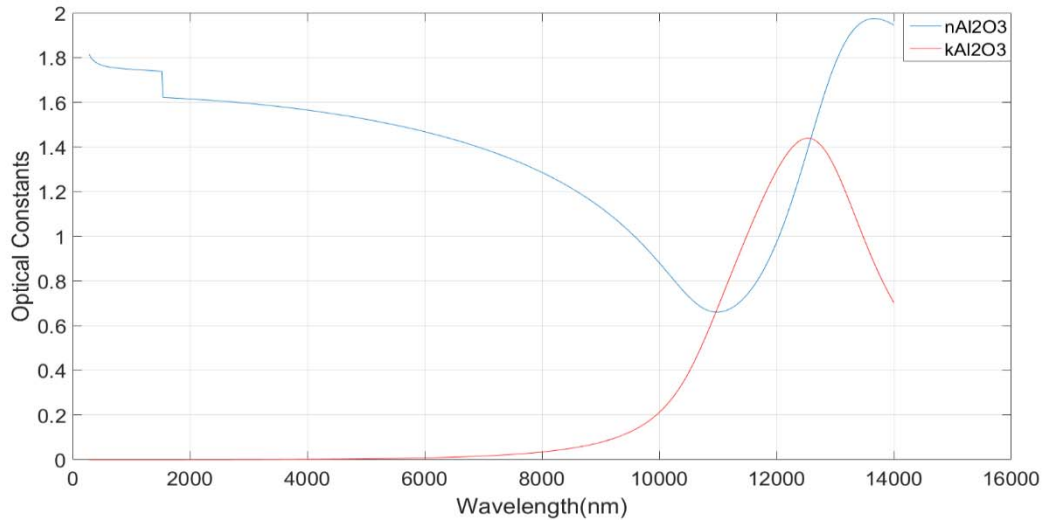


Figure 2.29. Refractive index and extinction coefficient of  $\text{Al}_2\text{O}_3$  with respect to wavelength.

As it can be seen from figure 2.29,  $\text{Al}_2\text{O}_3$  has low refractive index when compared with previously shown materials. It also does not have extinction coefficient in the visible and near infrared spectrum, thus it does not cause absorption in that spectrum. In addition to these, graph of extinction coefficient with respect to wavelength has a peak in mid-infrared spectrum. Because of that increase in extinction coefficient value in that spectrum,  $\text{Al}_2\text{O}_3$  emits in mid-infrared spectrum. In figure 2.30, spectral behavior of  $\text{Al}_2\text{O}_3$  is demonstrated.

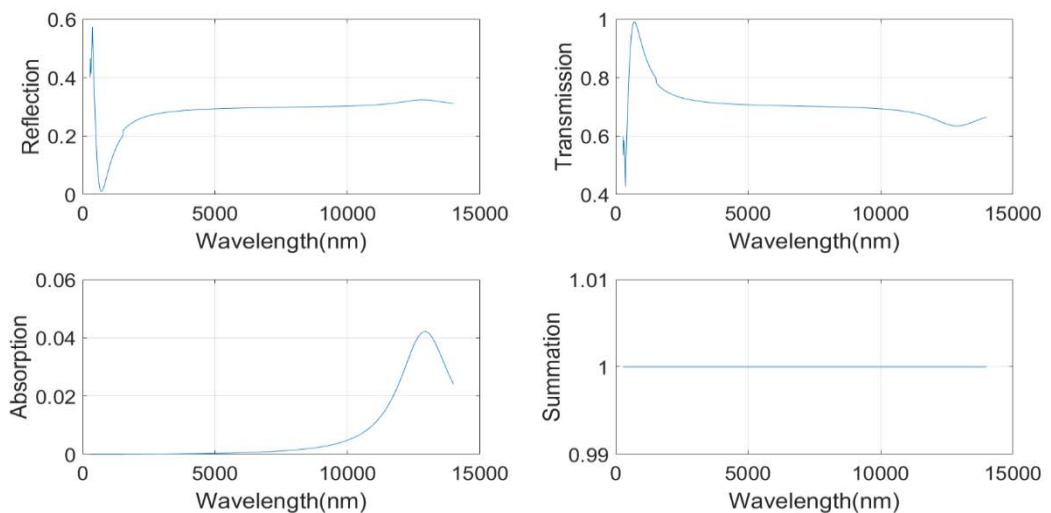


Figure 2.30. Spectral behavior of the  $\text{Al}_2\text{O}_3$  layer with thickness of 100 nm on Si substrate.

Results given in figure 2.30 are parallel to above discussion which is based on optical properties of  $\text{Al}_2\text{O}_3$ , given in figure 2.29. It does not absorb until  $6\ \mu\text{m}$  wavelength and has absorption peak around  $12\ \mu\text{m}$ . In figure 2.31, optical properties of  $\text{MgF}_2$  can be seen.

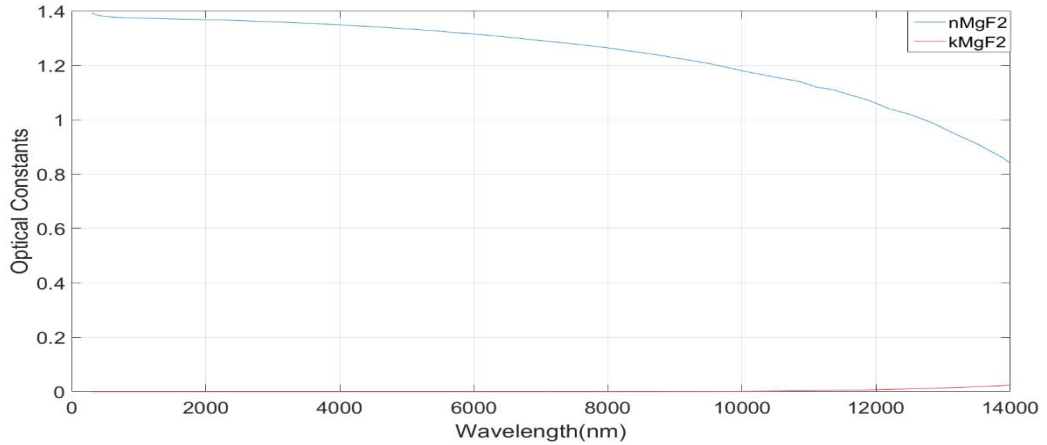


Figure 2.31. Refractive index and extinction coefficient of  $\text{MgF}_2$  with respect to wavelength.

Refractive index of  $\text{MgF}_2$  is smaller when compared to  $\text{Al}_2\text{O}_3$  in the visible and near infrared spectrum, which can be seen in figure 2.31. Due that property,  $\text{MgF}_2$  would be a better choice for design given in chapter 2.2. However, it also has lower extinction coefficient in the mid-infrared spectrum relative to  $\text{Al}_2\text{O}_3$ , which affects the amount of emission. Spectral behavior of  $\text{MgF}_2$  is demonstrated in figure 2.32.

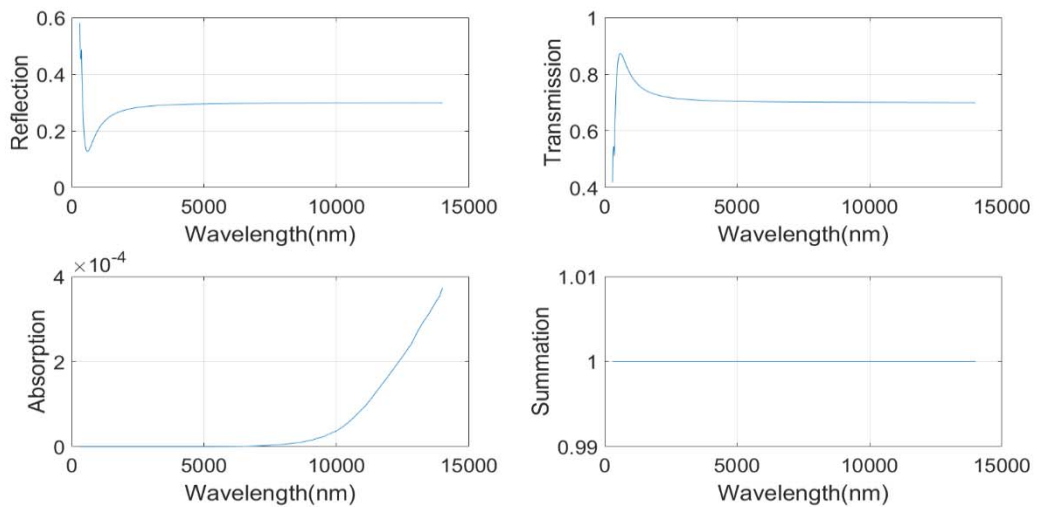


Figure 2.32. Spectral behavior of the  $\text{MgF}_2$  layer with thickness of 100 nm on Si substrate.

Spectral behavior of  $\text{MgF}_2$  is almost identical to  $\text{Al}_2\text{O}_3$ 's when figure 2.31 and 2.32 are compared. The reason for this similarity is the resemblance between optical properties. Although behavior patterns are same, magnitudes are different. Source of this difference lies in magnitudes of optical properties. For instance,  $\text{MgF}_2$  has lower emission in the mid-infrared spectrum, since it has lower extinction coefficient when compared with  $\text{Al}_2\text{O}_3$ . Optical properties of  $\text{SiO}_2$ , which is another low index material can be seen in figure 2.33.

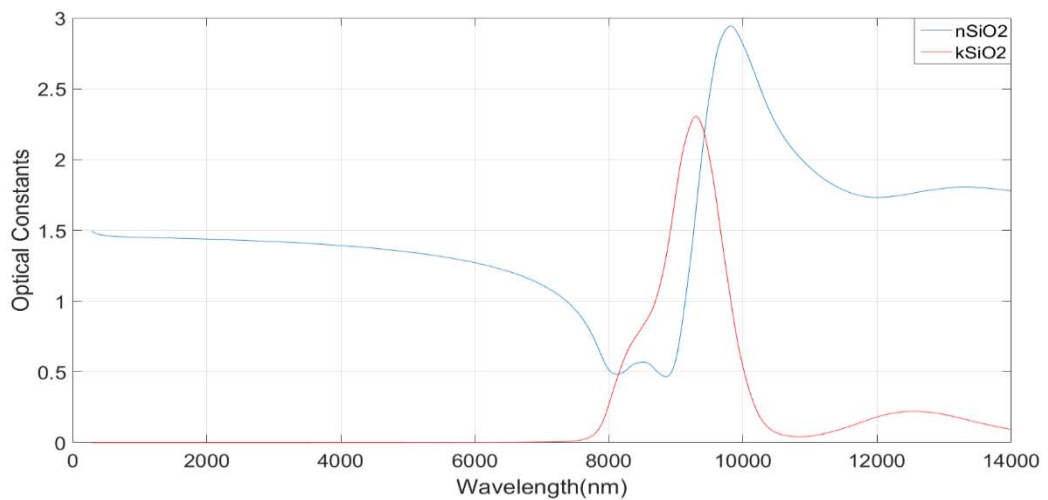


Figure 2.33. Refractive index and extinction coefficient of  $\text{SiO}_2$  with respect to wavelength.

When figure 2.33 is observed, it can be seen that refractive index of  $\text{SiO}_2$  is higher than  $\text{MgF}_2$ 's and lower than  $\text{Al}_2\text{O}_3$ 's slightly.  $\text{SiO}_2$  also has high extinction coefficient in middle infrared spectrum similar to  $\text{Al}_2\text{O}_3$ . Spectral behavior of  $\text{SiO}_2$  can be seen in figure 2.34.

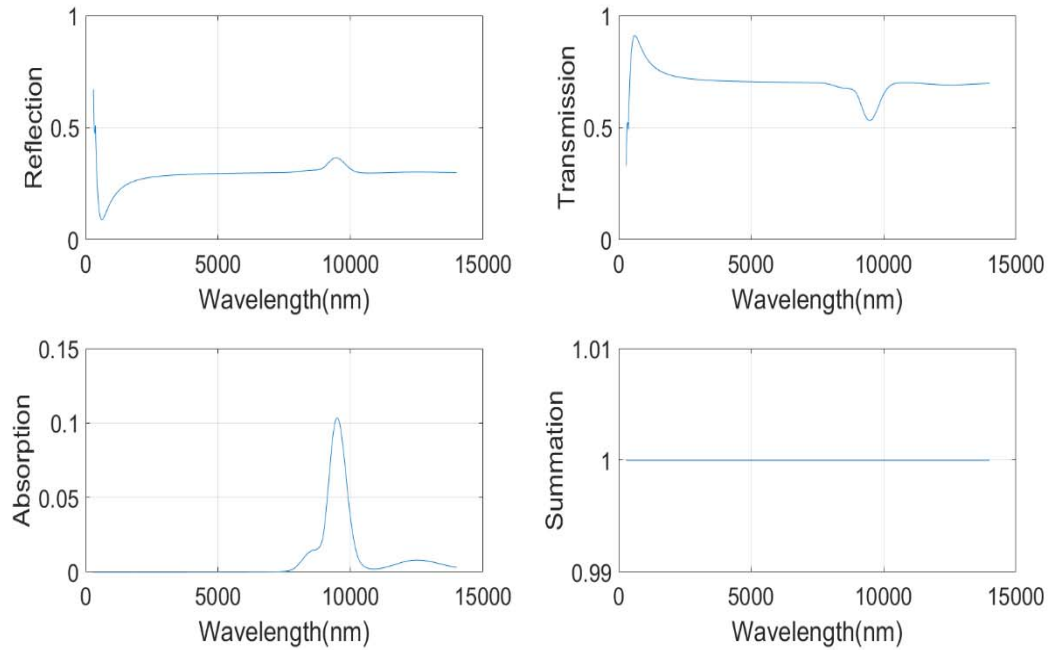


Figure 2.34. Spectral behavior of the SiO<sub>2</sub> layer with thickness of 100 nm on Si substrate

From figure 2.34, it can be seen that SiO<sub>2</sub> has almost similar absorption graph with Al<sub>2</sub>O<sub>3</sub>. Both does not cause absorption in the visible and near infrared spectrum and starts to absorb around mid-infrared spectrum. Difference between them in terms of absorption is that amount of absorption that SiO<sub>2</sub> makes is higher.

By analyzing behaviors of different materials in this section, the most suitable materials for a radiative cooling system can be selected. Considering the design given in chapter 2.2, materials with low and high refractive indexes have to be selected. Since the constraints given in chapter 3 are low absorption in visible and near infrared as well as high emission in mid-infrared spectrums, TiO<sub>2</sub> as high index and SiO<sub>2</sub> as low index material would be a good choice.

### 3 RADIATIVE COOLING SYSTEM DESIGN

Once dynamics of heat exchange between the design and its environment are defined, design requirements can be determined accordingly. Since dynamics of heat exchange are defined mathematically in chapter 2.3, necessary requirements can be deduced from those equations.

As stated in chapter 2.3, in order to cooling to be occurred, any system should transfer heat to its environment more than it receives. So, amount of heat flow into the system has to be minimized whereas outflow from the system has to be maximized. For this purpose, contributions from equations 2.19, 2.20, 2.21 and 2.22 have to be calculated. Firstly, heat transfer coefficient,  $h_c$ , given in equation 2.22 has to be minimized in order to insulate the design from its environment, hence prevent heat transfer to the system throughout conduction and convection.

Energy coming from the sun has to be hindered. Contribution from the sun is given in equation 2.21. Since incident solar irradiance to a given location is fixed as demonstrated in chapter 2.4, only tunable parameter in the equation 2.21 is emissivity of the system. By minimizing emissivity of the system at wavelengths in which high solar energy is carried, contribution from equation 2.21 can be minimized.

Finally, contribution from the surrounding molecules for which mathematical expression is given in equation 2.20, has to be minimized. Since thermal radiation from the atmosphere cannot be altered, only tunable parameter is the emissivity of the object as in equation 2.21. So, emissivity of the system has to be minimized at wavelengths where emissivity of the atmosphere is high, in other words atmosphere is opaque.

For the heat outflow from the system, equation 2.19 has to be maximized. This equation is the mathematical expression for the radiation that any body emits at different wavelengths. As emissivity of the body increases, radiation it emits also increases.

However, it is already stated that increasing emissivity in the spectrums in which solar energy is high and atmosphere is opaque, causes more heat inflow to the system. So, emissivity of the system has to be increased in the spectrums in which relatively small amount of solar energy is carried and atmosphere is transparent. Atmospheric transmittance in mid-infrared spectrum, 8-13  $\mu\text{m}$ , can be seen in figure 3.1 and solar irradiance with respect to wavelength from visible to mid-infrared spectrum can be seen in figure 3.2.

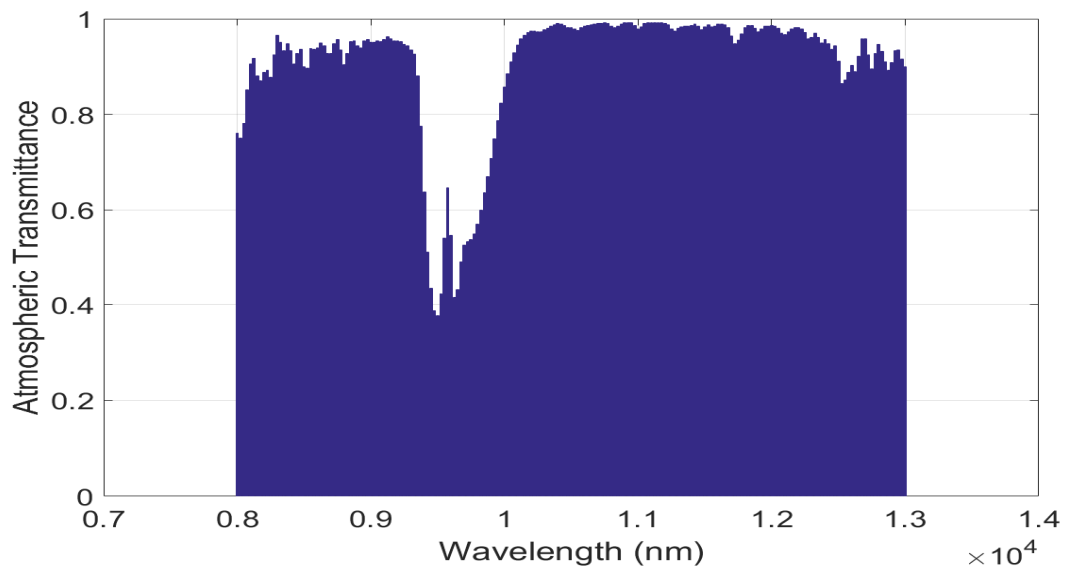


Figure 3.1. Atmospheric transmittance in the mid-infrared (8-13  $\mu\text{m}$ ) spectrum.

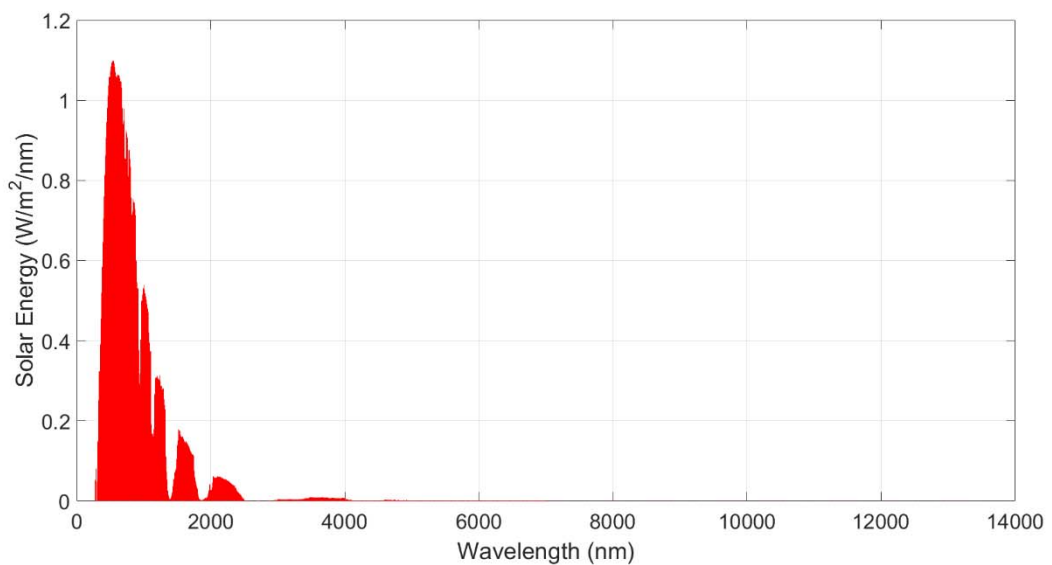


Figure 3.2. Solar irradiance with respect to wavelength from visible to mid-infrared (280nm to 14  $\mu\text{m}$ ) spectrum.

As it can be seen from figures 3.1 and 3.2, atmosphere is transparent in the mid-infrared spectrum and very low amount of solar energy is carried. So, when emissivity of a body is maximized in that spectrum, very small amount of energy flow into the system occurs, thus system radiates energy to its environment without absorbing high amount of energy.

In the light of the information given above, design requirements could be summarized as follows: System has to be insulated from its environment to minimize conduction and convection and emissivity of the system has to be minimized in the visible and near infrared spectrum and should be maximized in the mid-infrared spectrum. Ideal emissivity of a radiative cooling system is given in figure 3.3.

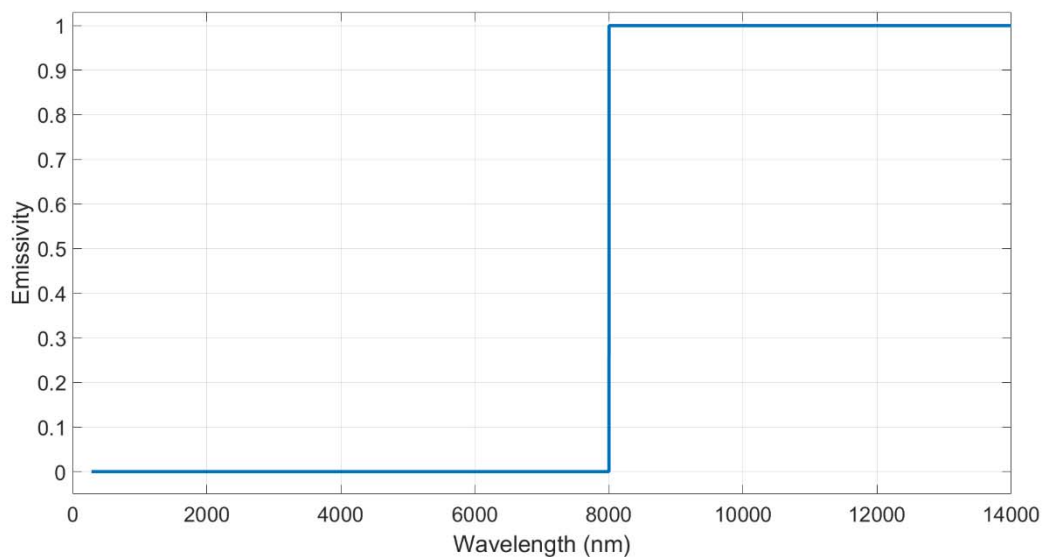


Figure 3.3. Ideal emissivity with respect to wavelength for a radiative cooling system.

Since there is not a material that has an emissivity profile as given in figure 3.3, a multilayer thin film system has to be designed. Developed multilayer system needs to reflect strongly in the visible and near infrared spectrum and emit in the mid-infrared spectrum. So, materials that are going to be used during the design should have very low absorption in the visible and near infrared spectrum and have high absorption in the mid-infrared spectrum.

Material selection for the multilayer design can be inspired from the findings demonstrated in chapter 2.5, since spectral behaviors of several materials are already illustrated there. Based on the given information in that chapter,  $\text{MgF}_2$ ,  $\text{SiO}_2$ ,  $\text{TiO}_2$  and  $\text{Al}_2\text{O}_3$  are appropriate choices, since they emit in the mid-infrared spectrum and more importantly they have extremely low absorption in the visible and near infrared spectrum.

The most important study in the literature can be considered as [42], since capability of a radiative cooling system under direct sunlight is shown both in theory and practice for the first time. Emission of the design demonstrated in [42] from visible to mid-infrared spectrum can be seen in figure 3.4.

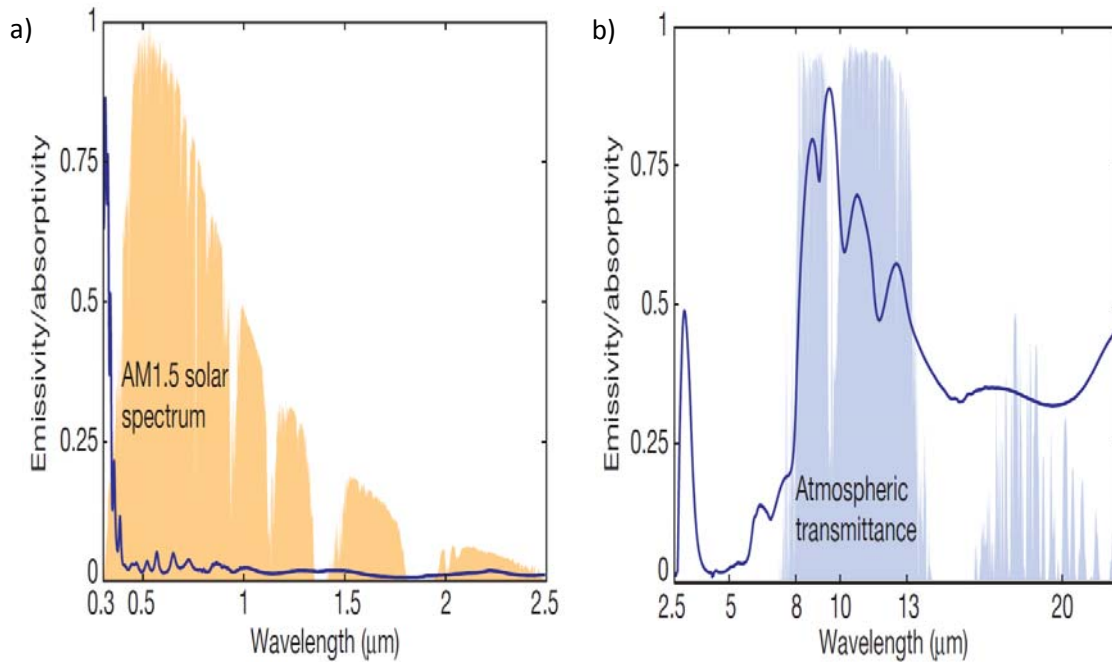


Figure 3.4. a) Emissivity of the design demonstrated in [42] from visible to near infrared spectrum. b) Emissivity from near infrared to mid-infrared.

From figure 3.4, it can be seen that designed structure has strong emission in the visible spectrum around 300-400 nm where solar energy is strong and has very low absorption in the rest of the spectrum until wavelength of 2.5  $\mu\text{m}$ . After 2.5  $\mu\text{m}$ , system starts to emit especially in 8-13  $\mu\text{m}$  wavelength range, where atmosphere is transparent as shown in figure 3.1. The design consists of following materials:  $\text{HfO}_2$ ,  $\text{SiO}_2$  and Ag all deposited on Si wafer. Before going into deeper analysis of the design, structure of it can be visualized with as shown in figure 3.5.

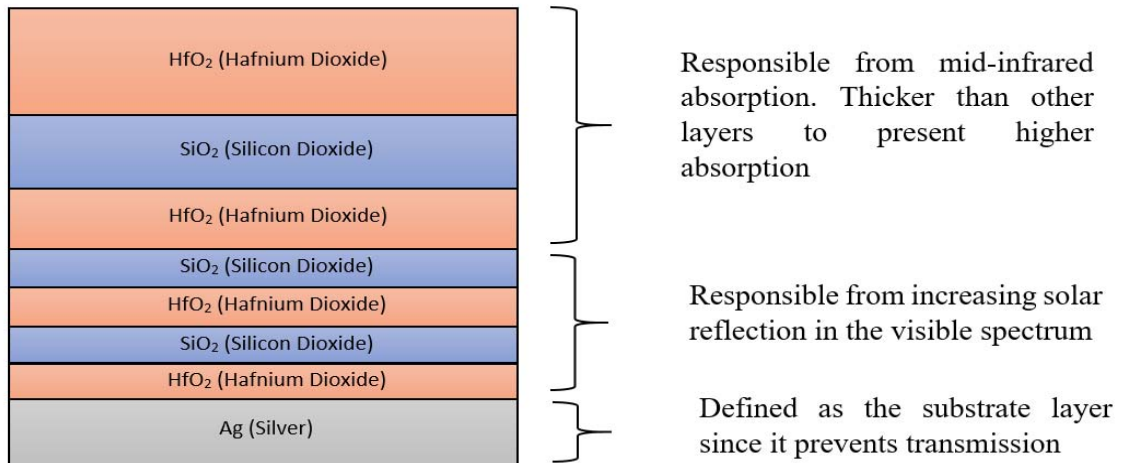


Figure 3.5. Visualization of radiative cooling design given in [42], which consists of seven thin film layers on top of a silver substrate.

As shown in figure 3.5, design consists of seven layers which are alternate high-low index layers. Number of layers and their thicknesses are determined by needle optimization method [47] for ideal reflection in the visible and near-infrared spectrum, and ideal emission in the 8-13  $\mu\text{m}$  spectrum. Also combination of simulated annealing and quasi-newton techniques are used to determine layer thicknesses after the needle optimization. HfO<sub>2</sub> is a high index material which has minimum absorption in the visible and near infrared spectrum and emits in the mid-infrared spectrum. Since, authors claim that TiO<sub>2</sub>, whose spectral behavior is given in chapter 2.5, would be used instead of HfO<sub>2</sub> as high index material TiO<sub>2</sub> is used as high index material. SiO<sub>2</sub> on the other hand, is the low index layer which has very similar spectral behavior with HfO<sub>2</sub> in terms of absorption. So in the aspect of spectral behaviors of the materials, these two materials denote parallel emissivity patterns to ideal emissivity given in figure 3.3. However, emissivity of the Ag contradicts with the ideal emissivity pattern. Intuition behind the usage of Ag in the design despite to this contradiction can be explained with the analysis of the spectral behavior of the overall design.

With the method demonstrated in chapter 2.1, design which is given above is imitated partially. Given structure in figure 3.5 is preserved in which top three layers are used for increasing emissivity in the 8-13  $\mu\text{m}$  spectrum, four layers are used to increase solar reflection on top of a Ag layer. Relying on author's claim about replacement of  $\text{HfO}_2$  with  $\text{TiO}_2$ ,  $\text{TiO}_2$  is used as high index material during the analysis. Although layer thicknesses are changed slightly, similar emissivity pattern could be obtained for the  $5^\circ$  incidence angle. Emissivity pattern for partially imitated design can be seen in figure 3.6.

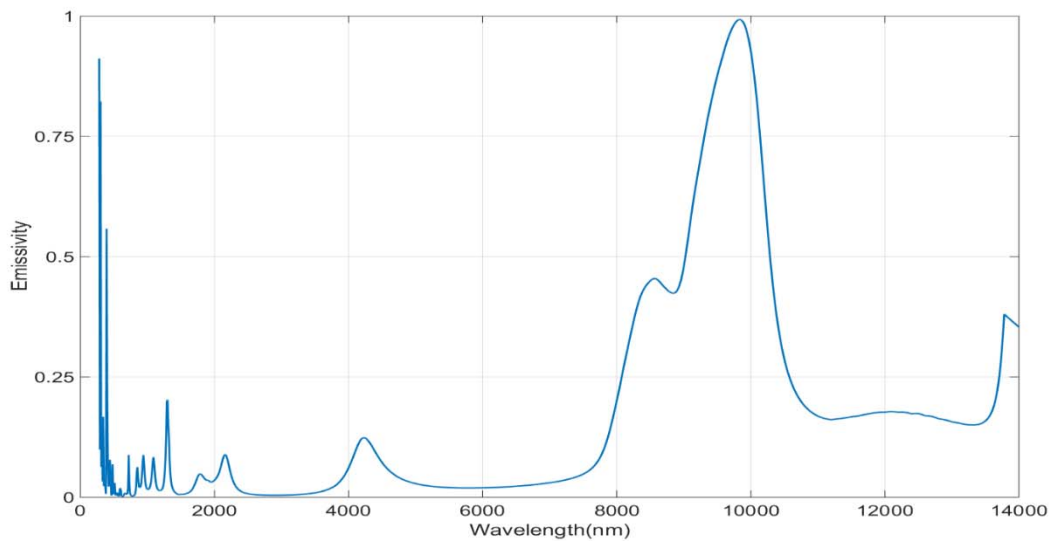


Figure 3.6. Emissivity graph of the partially imitated design given in [42] with respect to wavelength.

When compared with figure 3.4, obtained results in figure 3.6 is very similar. Reason for slight differences may stem from both usages of  $\text{TiO}_2$  instead of  $\text{HfO}_2$  and layer thicknesses. In order to understand the necessity of the Ag layer in this design, emissivity of the same thin film system without Ag layer this time is calculated and results are illustrated in figure 3.7.

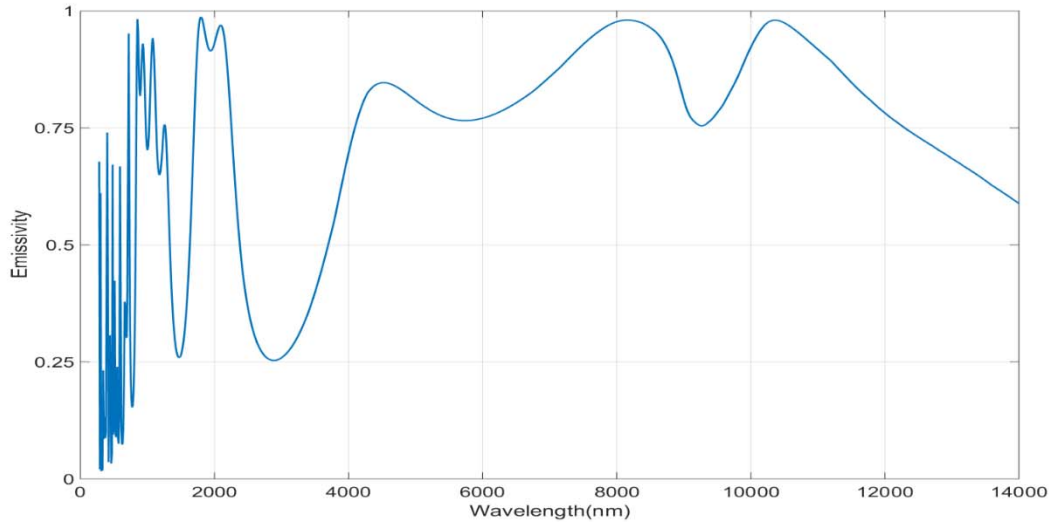


Figure 3.7. Emissivity graph of the partially imitated design from which silver layer is excluded.

As it can be seen from figure 3.7, emissivity of the thin film system is significantly altered. High amount of solar absorption occurred in the visible and near-infrared spectrum which violates the most important requirement of radiative cooling. So, with the specified number of  $\text{TiO}_2$  and  $\text{SiO}_2$  layers only, desired reflection in the solar spectrum cannot be achieved. From this result, role of Ag layer can be understood. As shown in chapter 2.5, Ag has broadband reflection from visible to mid-infrared spectrum. However, besides its high reflection behavior in solar spectrum, Ag layer brings an inevitable solar absorption. That absorption is inevitable in this design, because layers on top transmits the incident light onto the Ag layer and transmission behavior of  $\text{TiO}_2$  and  $\text{SiO}_2$  are again examined in chapter 2.5.

In order to observe the incidence angle dependency of the thin film design, emissivity of it is calculated for various incidence angles and results are demonstrated in figure 3.8.

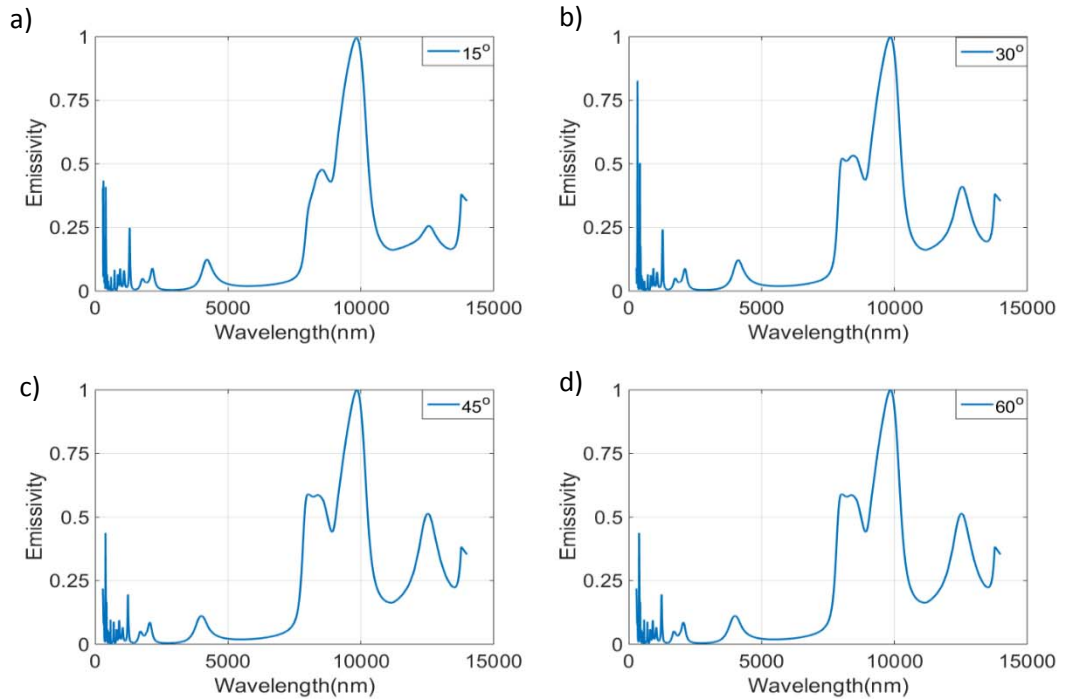


Figure 3.8. Emissivity of the partially imitated design for incidence angles of  $15^\circ$ ,  $30^\circ$ ,  $45^\circ$  and  $60^\circ$  in a, b, c and d respectively.

Results illustrated in figure 3.8 indicate that emissivity of this design does not vary dramatically with respect to incidence angle. A small change of emissivity in the visible spectrum can be observed whereas emission in mid-infrared spectrum is not affected by incidence angle.

Once the structure of the design is examined, performance of the radiative cooling design can be determined by evaluating its spectral behavior and calculating heat flows. For the performance evaluations, it is assumed that design is tested in Istanbul on 21 March 2016 at 12:00, which corresponds to incidence angle of  $40^\circ$  as given in chapter 2.4. Structure's reflection is around %97 when integrated from 280 nm to 2500 nm, where nearly  $940 \text{ W/m}^2$  solar energy is carried. So, nearly  $910 \text{ W/m}^2$  incident energy is reflected from the surface of the system. Emissivity of the structure is also integrated in  $8\text{-}13\mu\text{m}$  range, to evaluate amount of radiation to the outer space and calculation yields emission around %45 which corresponds to  $70 \text{ W/m}^2$  cooling. By inserting these values, also with other calculated heat flow components, into the heat balance equation given in chapter 2.3, net cooling power for this design comes out to be around  $35 \text{ W/ m}^2$ .

Results illustrated above is a solid proof that demonstrated model in chapter 2.1 is able to calculate spectral behavior correctly, since it yields similar results to those given in the literature for a multilayer thin film system. Until this point, a rough imitation of a design given in the literature is analyzed, it's results are presented and compared with results of our calculations. Once validity of our model is verified, further design studies to end up with systems whose cooling power is higher, can be conducted.

As mentioned several times, emissivity of the overall thin film structures determines the performance of radiative cooling systems. There are two ways to increase the performance of a radiative cooling system. Firstly, emissivity has to be minimized in the visible spectrum and secondly it has to be maximized in the 8-13  $\mu\text{m}$  range. As a starting point, design studies to increase the emission in the mid-infrared spectrum is conducted and those studies are explained below.

Absorption of several materials with respect to wavelength are investigated in chapter 2.5. As shown in that chapter,  $\text{SiO}_2$  has absorption peak around 10  $\mu\text{m}$  and because of that behavior, emissivity of the previous design reaches to 1 almost around 10  $\mu\text{m}$ . However, absorption peak of  $\text{TiO}_2$  cannot be observed until 14  $\mu\text{m}$ , so a distinctive peak in the design would not be observed which is caused by  $\text{TiO}_2$ . In addition to these materials,  $\text{Al}_2\text{O}_3$  has an absorption peak around 13  $\mu\text{m}$  whose magnitude is higher than  $\text{TiO}_2$ 's and lower than  $\text{SiO}_2$ 's. So, a design with  $\text{Al}_2\text{O}_3$  included would provide improved performance. In figure 3.9, schematic structure of the new design and differences from first design are illustrated.

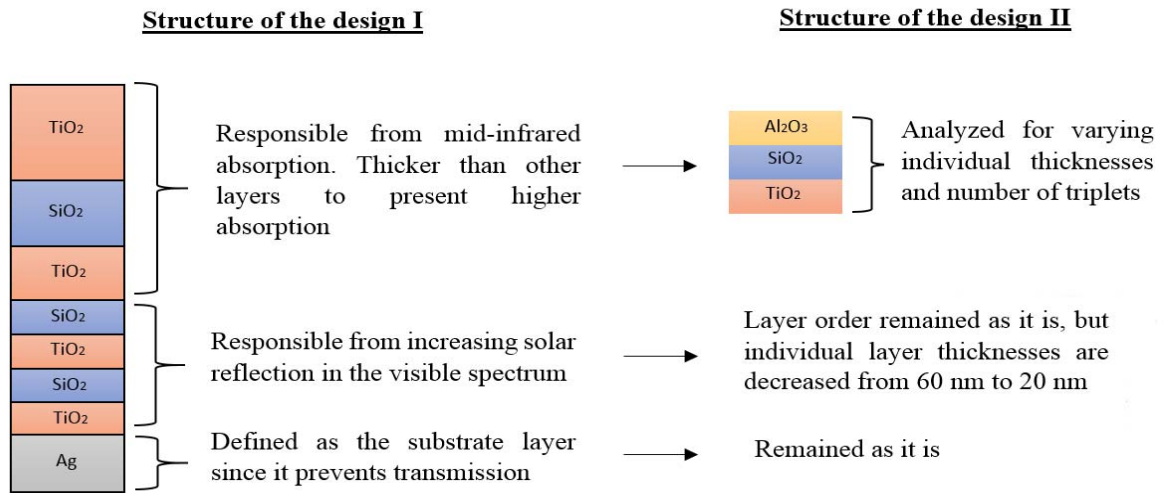


Figure 3.9. Schematic representation of structure of design II showing the changes from design I to design II.

In the previous design top three layers are responsible from the mid-infrared emission and average absorption in that spectrum is around %45. It is known that each layer absorbs at wavelengths in which extinction coefficient is present. Considering that fact, by increasing number of layers, composed of materials which have non-zero extinction coefficients in 8-13  $\mu\text{m}$ , average emission can be improved in that range. Only side effect of increasing number of layers would be raise in the overall thickness. For the sake of balancing overall thickness, thickness of each layer which are responsible from solar reflection, are decreased from 60 nm to 20 nm.

Solar reflection, from 280 nm to 2.5  $\mu\text{m}$  wavelength, almost remained same due to absence of any dramatic change in the solar reflection segment in the second design. Since the focus of the second design is on 8-13  $\mu\text{m}$  range and changes in visible and near-infrared spectrums are almost negligible, graphs of the conducted analysis are in 8-13  $\mu\text{m}$  range. First, performance of the second design in 8-13  $\mu\text{m}$  is compared with the previous design's performance. Second, to show the effect of addition of  $\text{Al}_2\text{O}_3$  layers in the mid-infrared absorption, system performance is evaluated with and without  $\text{Al}_2\text{O}_3$  layers. Third, the new design's performance is analyzed in 8-13  $\mu\text{m}$  for varying thicknesses of individual layers' in the triplets, which consist of  $\text{Al}_2\text{O}_3$ ,  $\text{SiO}_2$  and  $\text{TiO}_2$ . Also, influence of number of triplets is examined at fixed thicknesses. Finally, it is analyzed for different incidence angles. Comparison of emission curves of the two design can be seen in figure 3.10.

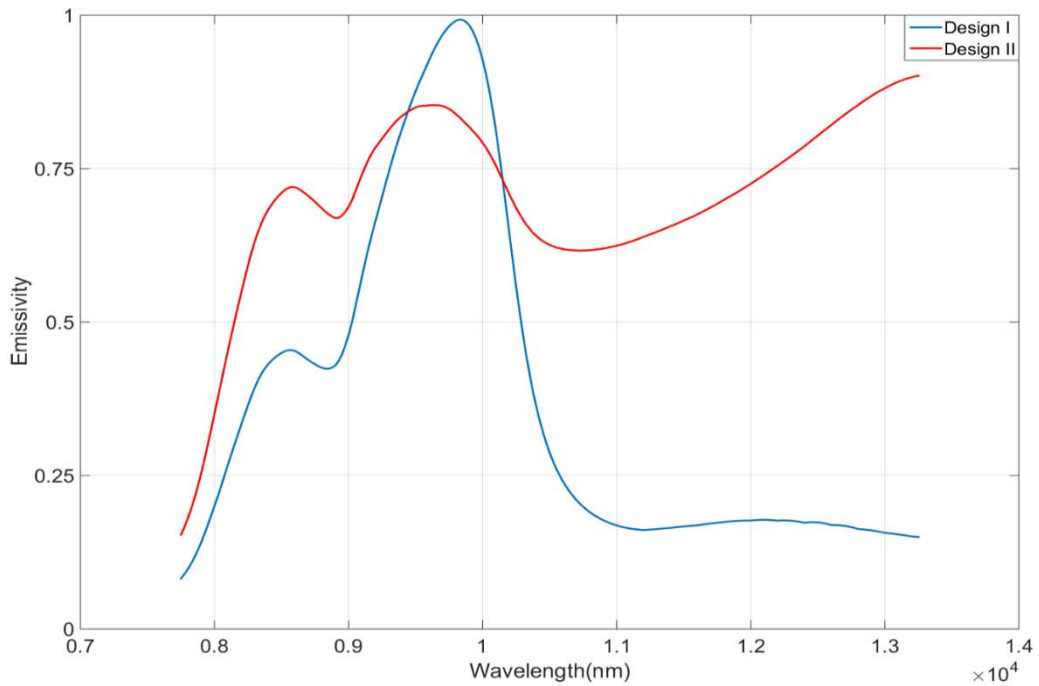


Figure 3.10. Comparison of emission curves in design I and II in 8-13  $\mu\text{m}$  spectrum.

In figure 3.10, graphs of absorptions of two designs with respect to wavelength is illustrated. In the second design three triplets with individual layer thicknesses of 200 nm are placed on top of solar reflection segment. When compared in terms of thicknesses, overall thickness of the first design was 1300 nm (except the silver layer), whereas thickness of the second design is 1900 nm. So, second design is 600 nm thicker than the first design. In terms of performance considerable amount of increase in the emissivity of the second design with respect to first design's emissivity can be observed. Average emissivity of the second design is around %71, whereas it is %45 in the first design. So, a dramatic change in the mid-infrared emission occurred.

To observe contribution coming from  $\text{Al}_2\text{O}_3$  layers, performances of two variations of the second design are compared. In one of the designs, alternating  $\text{SiO}_2$  and  $\text{TiO}_2$  layers are used, each 200 nm thick and 9 layers in total. In the other one, 200 nm of  $\text{SiO}_2$ ,  $\text{TiO}_2$  and  $\text{Al}_2\text{O}_3$ , each 200 nm thick and 9 layers in total are used. So for the same number of layers and thicknesses, influence of  $\text{Al}_2\text{O}_3$  layers are observed. Results of this comparison are examined in figure 3.11.

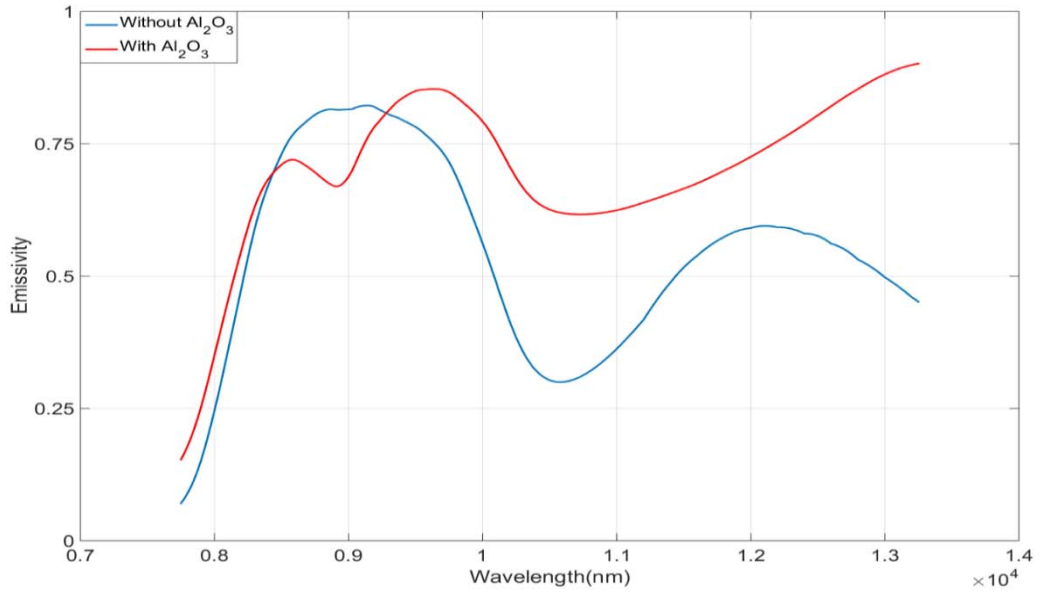


Figure 3.11. Comparison of emission curves of with and without Al<sub>2</sub>O<sub>3</sub> layers.

As it can be seen from figure 3.11, including Al<sub>2</sub>O<sub>3</sub> layers increase emission in the mid-infrared spectrum especially after 10 μm. In average, system with Al<sub>2</sub>O<sub>3</sub> layers has %71 emission as stated above, whereas it is %55 for the system which does not have Al<sub>2</sub>O<sub>3</sub> layers. So for this configuration, including Al<sub>2</sub>O<sub>3</sub> layers brings %15 more emission. In the following figure, results for varying individual layer thicknesses in the triplets are demonstrated.

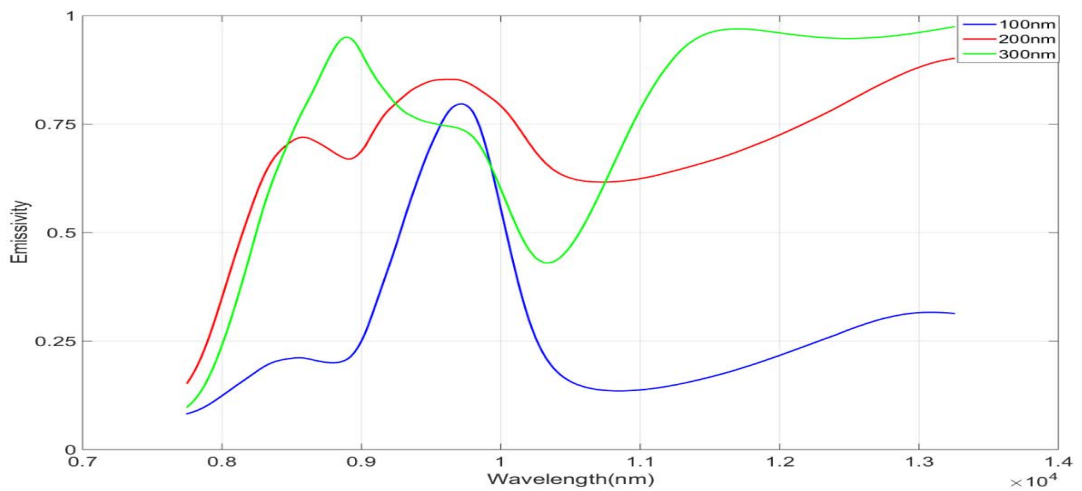


Figure 3.12. Comparison of emission curves for varying individual layer thicknesses of 100 nm, 200 nm and 300 nm in the triplets.

Results in figure 3.12 indicates that as individual thicknesses of the layers in the triplets increase, amount of emission also increases. In this configuration, 9 layers are used in the absorption segment. For 100 nm case average emissivity is around %30, for 200 nm it is around %71 and finally for 300 nm case it is around %78. So by looking at the high rate of change between 100 nm and 200 nm case relative to 200 nm to 300 nm, rate of change decreases as the layers get thicker. In the next figure, effect of layer number is examined.

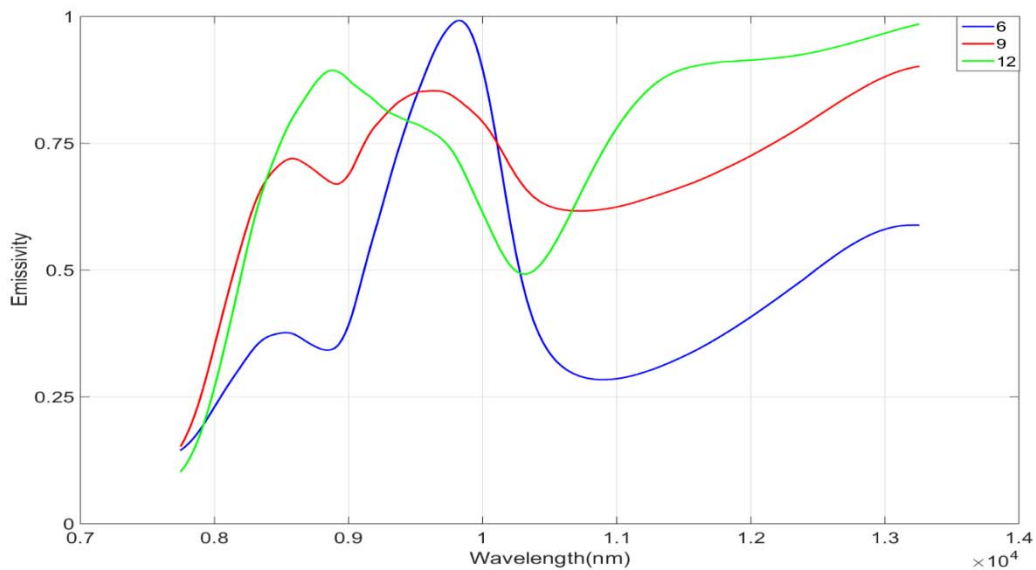


Figure 3.13. Comparison of emission curves for varying number (multiples of number of triplets) of absorption layers whose individual layer thicknesses are 200 nm.

In figure 3.13, layer numbers in the absorption segment are set to 6, 9 and 12 which corresponds to 2, 3 and 4 triplets. Although absorption around 10  $\mu\text{m}$  is lower for larger number of layers, it is higher for other wavelengths in 8-13  $\mu\text{m}$  range. For layer numbers of 6, 9 and 12 average emissions are around %47, %71 and %77 respectively. As in the analysis of layer thicknesses, amount of increase gets smaller as the number of layers increase. Results related to emission of the system for various incidence angles can be seen in figure 3.14.

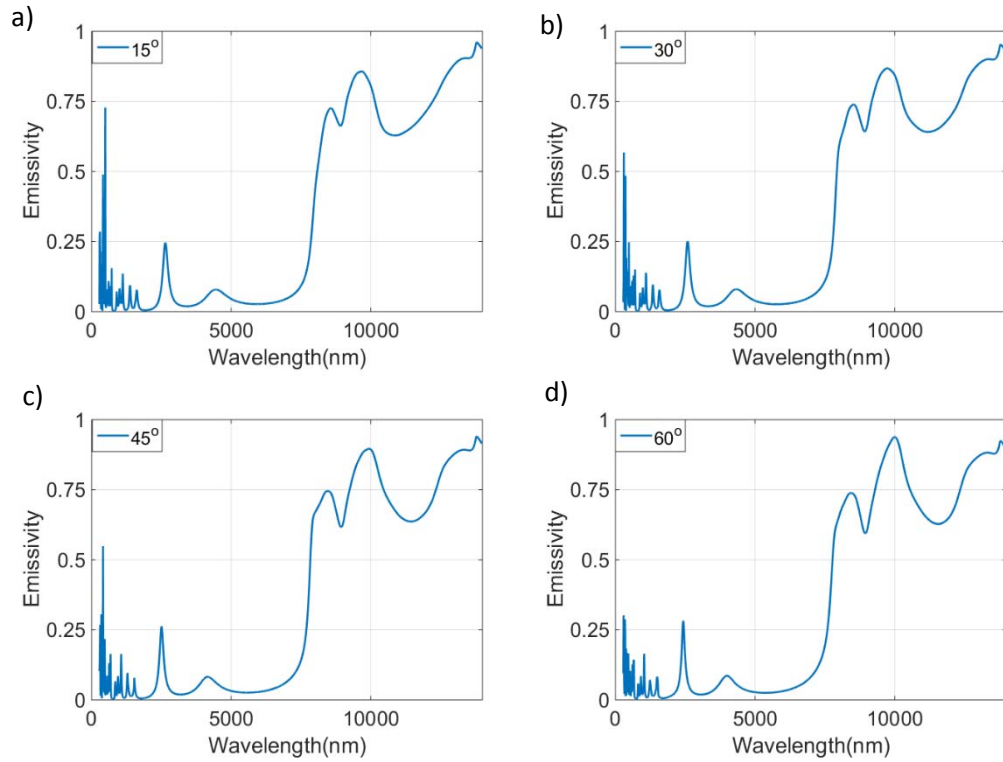


Figure 3.14. Comparison of emission curves of systems, which has 3 absorption triplets with individual thicknesses of 200 nm, for varying incidence angles of 15°, 30°, 45° and 60° from ‘a’ to ‘d’ respectively.

As shown in figure 3.14, emissivity curves of systems with 3 absorption triplets which have individual layer thicknesses of 200 nm, are plotted against wavelength for incidence angles of 15°, 30°, 45° and 60°. Reflection in the 280 nm to 2.5 μm spectrum is around %96 in each case with slight fluctuations when integrated with respect to wavelength. Emission in the 8-13 μm is around %73 for different incidence angles again with small fluctuations. So, spectral behavior of the design is not altered dramatically as incidence angle changes.

As in the case of previous design, once emissivity of the multilayer system is obtained it is used in the equations given in chapter 2.3 to obtain net cooling power of the system. Second design is also tested at the same conditions with the previous design, for the purpose of making objective comparisons. So, emissivity of the second design is plotted against wavelength at 40° and results are demonstrated in figure 3.15.

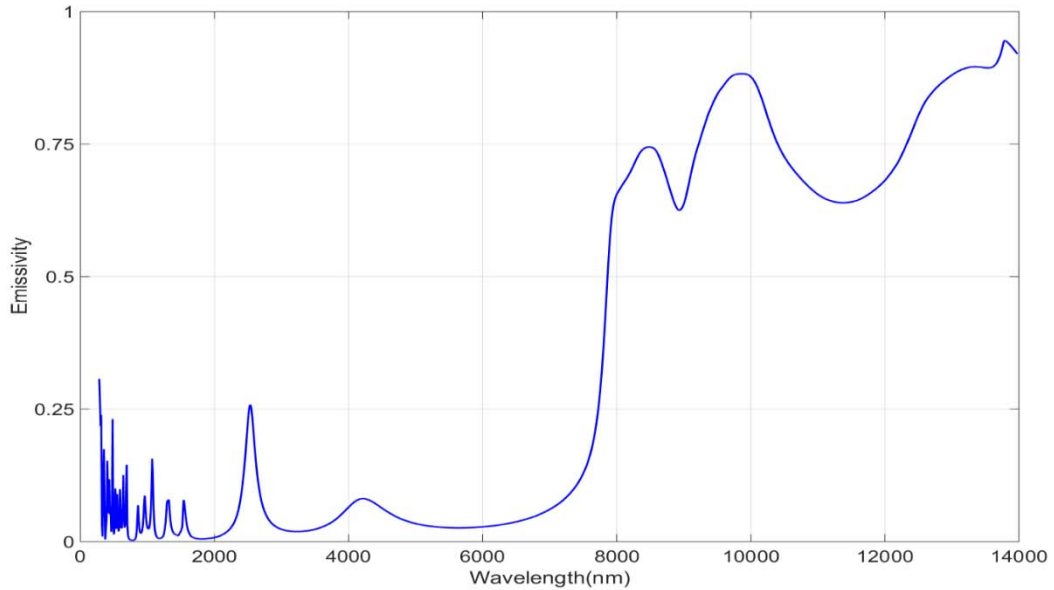


Figure 3.15. Emissivity curve of the second design at 40° incidence angle with 3 absorption triplets, each has individual layer thickness of 200 nm.

Demonstrated emissivity graph belongs to second design with 3 absorption triplets, which has individual layer thickness of 200 nm, with respect to wavelength at incidence angle of 40°. When integrated from 280 nm to 2.5  $\mu\text{m}$ , reflection is around %96 and emission in 8-13  $\mu\text{m}$  range is around %74. 900  $\text{W}/\text{m}^2$  incident solar energy is reflected from the surface of the system and nearly 110  $\text{W}/\text{m}^2$  energy is emitted in the 8-13  $\mu\text{m}$  range. According to calculations given in chapter 2.4, system has net cooling power of 62  $\text{W}/\text{m}^2$  which is almost twice of the previous design's.

After a comprehensive analysis of the second design, it is shown that cooling power can be increased by including an extra material,  $\text{Al}_2\text{O}_3$ , which has different absorption peak than  $\text{TiO}_2$  and  $\text{SiO}_2$ . It is also shown that by increasing layer thicknesses and number of triplets, emission in the 8-13  $\mu\text{m}$  range can be increased without observing a substantial change in the reflection in 280 nm to 2.5  $\mu\text{m}$  range. So by an extensive numerical optimization, number of triplets and thicknesses of each individual layer can be determined such that emission in the atmospheric transparency window is maximized.

As mentioned before in this chapters, increasing emission in transparency window and reflection in the visible and near-infrared spectrum improves the performance of a radiative cooling system. In the second design, ways of increasing emission in the atmospheric transparency window are studied. Although considerable amount of

improvement is observed in the cooling power, design studies are restricted to 8-13  $\mu\text{m}$  range and this situation limits the overall design performance. A new design, which contains findings from second design studies, may yield even more improved performance. To end up with such a design, problems with the previous designs have to be carefully examined.

In the second design, it is shown that emission in the mid-infrared spectrum can be increased tremendously by using triplets. However, in all cases, nearly %3-4 absorption is present in the visible and near infrared spectrum which corresponds to 33  $\text{W}/\text{m}^2$  solar energy. If that energy had been reflected, cooling power would have been improved. In addition to this, if that reflection had been achieved by a multilayer thin film system which contains triplets or couples which consist of materials that introduce absorption in the mid-infrared spectrum, as in the case of second design, emission in that spectrum would have been increased. Since, such a design satisfies two main requirements better than previous designs, e.g. less absorption than %3-4 in the visible and near infrared spectrum and at least %70 emission in 8-13  $\mu\text{m}$  range, it may outperform the previous designs. In order to prevent that %3-4 absorption, source of it has to be determined properly.

Various materials' spectral behavior is analyzed in chapter 2.5 including Ag thin film layer. As examined in figure 2.24, Ag has high absorption in the visible spectrum which is also present in the previous designs. So, it can be concluded that source of %3-4 absorption stems from presence of an Ag layer which absorbs nearly %4 percentage of incident light in the visible and near-infrared spectrum. Considering  $\text{TiO}_2$ ,  $\text{Al}_2\text{O}_3$  and  $\text{SiO}_2$  does not cause absorption in the visible spectrum, overall system still introduces absorption in the visible and near-infrared spectrum in the previous designs, although Ag layer is placed at the bottom in both of them. This behavior indicates that layers above Ag transmits the incident light to the Ag layer. This claim about the transmission can be verified as follows: In the previous designs, Ag is defined as a layer in the thin film system, not as the substrate. As mentioned in chapter 2.1, model provides the transmission onto the substrate. So, transmission data of the system when Ag is not defined as substrate is expected to be very low in magnitude. On the other hand, transmission data should be high in magnitude when Ag is defined as the substrate according to proposed claim above. Related figures to this comparison can be seen in figure 3.16 and 3.17.

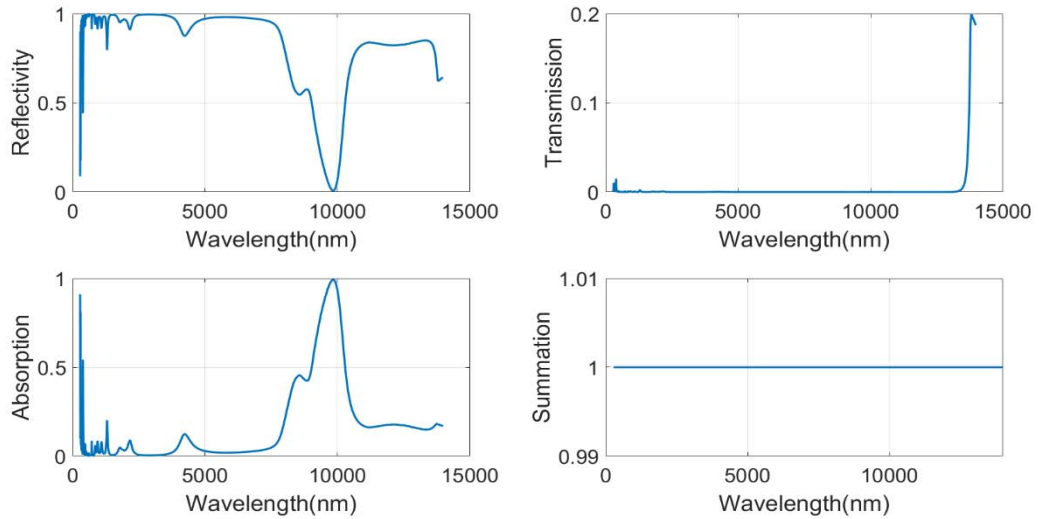


Figure 3.16. Spectral behavior of the first design when Ag is defined as a layer on top of Si substrate.

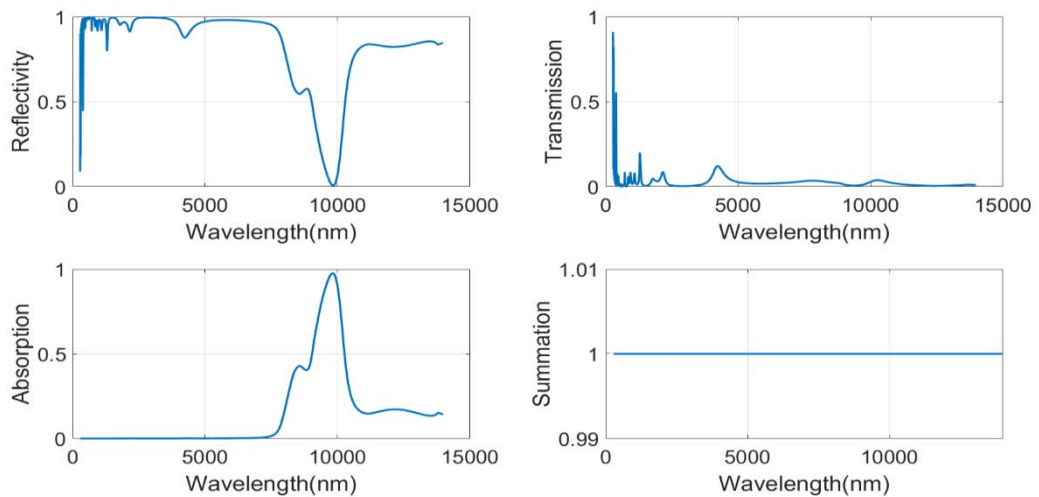


Figure 3.17. Spectral behavior of the first design when Ag layer is defined as the substrate.

In figure 3.16, spectral behavior of the first design is demonstrated when Ag is not defined as the substrate. It can be seen that transmission to the substrate is extremely low due to presence of an Ag layer which does not transmit incident light to the adjacent medium. On the other hand, transmission to the substrate is high especially in the visible spectrum, as shown in figure 3.17, when Ag is defined as the substrate. This comparison is a solid proof that layers above the Ag in the previous designs transmit the incident light to the Ag layer, which is responsible from high absorption in the visible spectrum.

Once source of absorption in the visible spectrum is determined, next stage is to prevent this absorption. This can be achieved by maximizing the reflection in the visible and near-infrared spectrum without any contribution from Ag layer. More explicitly, it is already shown in figure 3.17 that in the absence of Ag layer, previous designs are not capable of providing broadband reflection, thus necessitation of usage of Ag layer in the previous designs are proved. So, although Ag is essential in terms of providing broadband reflection, due to its absorption in the visible spectrum usage of it has to be avoided to improve system performance. For that purpose, radical changes have to be made in the design structure.

In chapter 2.2, it is shown that by using high-low index layers high reflection zones can be obtained with dielectrics by arranging optical thicknesses of the layers. A set of high-low index layers form a segment which has high reflection as a spectral response and by using different segments which create high reflection zones at different spectral ranges, high reflection over a desired spectrum range can be obtained. Comparison scheme of the previous designs and the new design can be seen in figure 3.18.

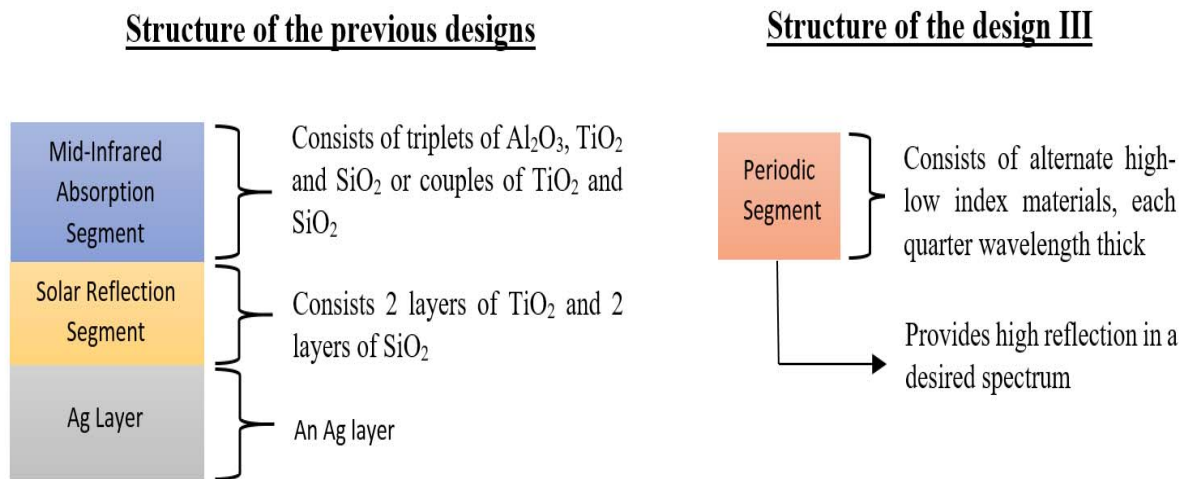


Figure 3.18. Comparison of structures of the previous designs and the new design. Third design is composed of more than one segment.

By designing the periodic segment demonstrated in figure 3.18, selection of high-low index materials and determination of geometrical thicknesses of the layers, a new system which satisfies radiative cooling requirements can be obtained. Design process and validation of the decisions related to design are expressed below.

Firstly, in chapter 2.2, influence of ratio of the refractive indexes of the layers is illustrated. To achieve higher reflection and wider width with lower number of layers, ratio of the refractive indexes needs to be selected as high as possible. However, reflection in the visible and near-infrared spectrum is not the only requirement of the radiative cooling as stated above several times. If materials that are going to be used have emission in the 8-13  $\mu\text{m}$  range, then two requirements of the radiative cooling can be achieved in similar segments. In other words, segments that are responsible from high reflection in the visible and near-infrared spectrum may also increase the absorption in the 8-13  $\mu\text{m}$ , if materials in the segments have non zero extinction coefficients in the mid-infrared spectrum. Since  $\text{TiO}_2$  and  $\text{SiO}_2$  have emission in the 8-13  $\mu\text{m}$  range and ratio of refractive indexes nearly 1.6 at visible and near infrared spectrum, they are chosen as materials to be used in the segment designs. When materials in the segments are determined, based on the equations 2.15 and 2.16, required thicknesses of the layers at the specified wavelengths can be calculated.

In the following design, aim is to achieve high reflection between 280 nm and 2.5  $\mu\text{m}$ , in which solar energy is high when compared to longer wavelengths as shown in figure 3.2. For that purpose, 8 segments are designed to provide high reflection zones around 300, 600, 750, 900, 1200, 1500, 2000 and 2300 nm. Geometrical thicknesses of the layers are calculated such that they satisfy the condition given in equation 2.13. Design performance is analyzed for different number of layers in the segments and various incidence angles. In figure 3.19, emission of the system for various number of layers in the segments at a fixed angle is demonstrated.

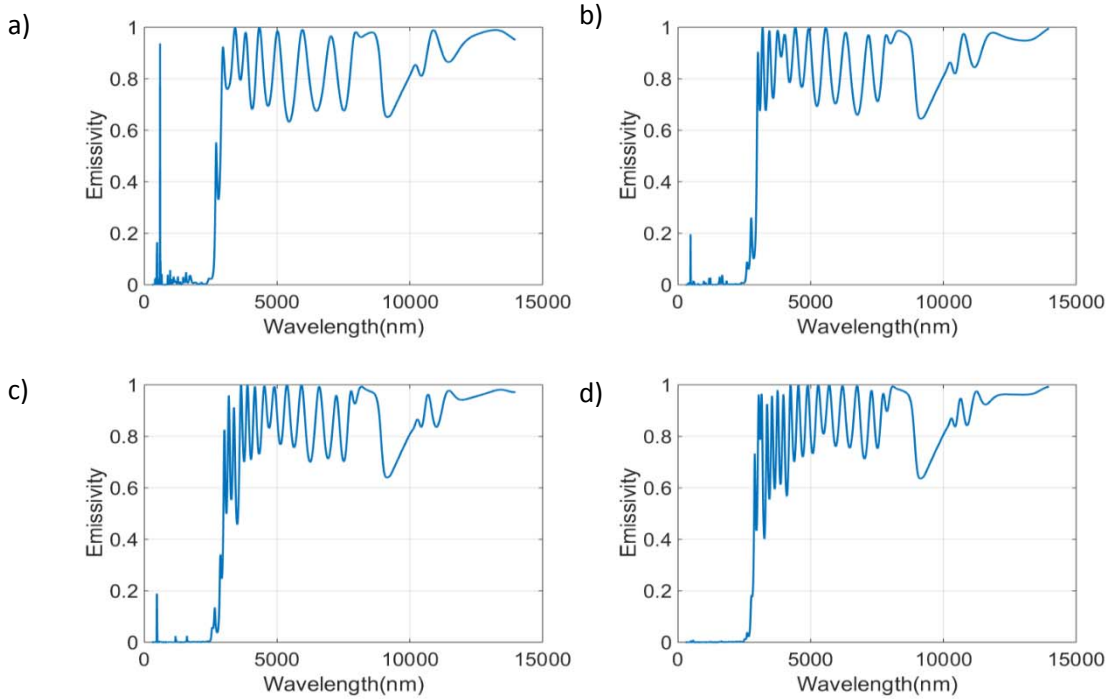


Figure 3.19. Emissivities of the systems with number of layers of 6, 8, 10 and 12 at each segment for incidence angle of  $0^0$  for cases ‘a’, ‘b’, ‘c’ and ‘d’ respectively.

As shown in figure 3.19, very low emission is occurred from 280 nm to 2.5  $\mu\text{m}$  spectrum. On the other hand, system strongly emits after 2.5  $\mu\text{m}$  wavelength. In order to evaluate the performance in a more scientific fashion, emissivities are integrated with respect to wavelength both in 280 nm to 2.5  $\mu\text{m}$  range and 8-13  $\mu\text{m}$  range and results are demonstrated in table 3.1.

Number of Layers in the Segments	Reflection in the 280 nm to 2.5 $\mu\text{m}$ spectrum range	Emission in the 8-13 $\mu\text{m}$ spectrum range
6	% 98.51	% 68.53
8	% 99.57	% 73.74
10	% 99.74	% 77.23
12	% 99.9	% 79.74

Table 3.1. Rates of reflection and emission for various number of layers in the segments in different spectrum ranges.

When table 3.1 is considered, an increase in both reflection and emission in the spectrum ranges of interest can be observed. In the following figure, effect of incidence angle on emissivity is examined.

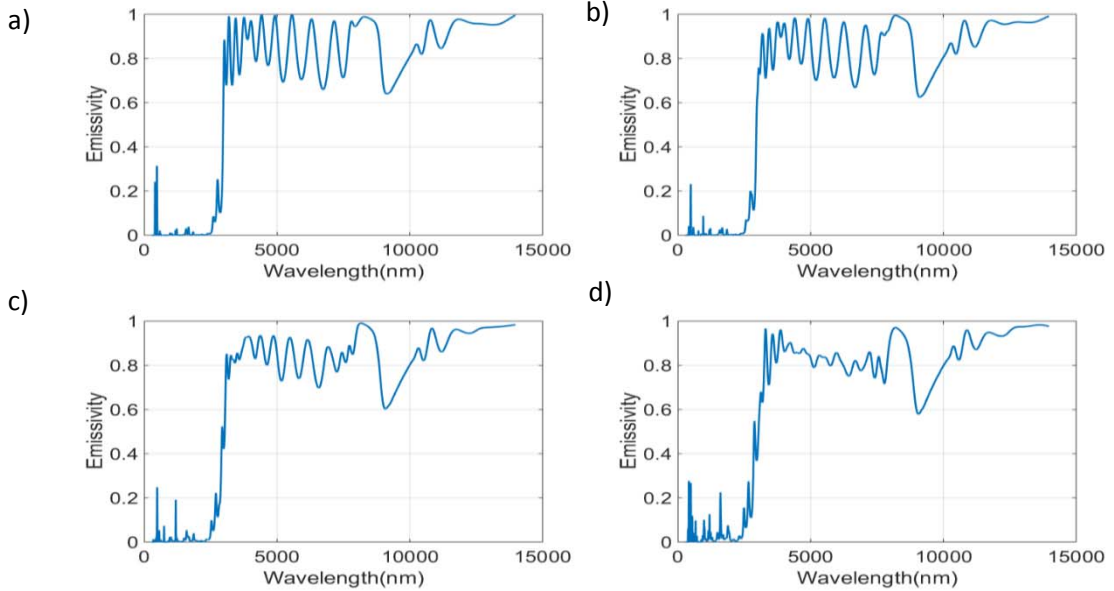


Figure 3.20. Emissivities of the systems with 8 layers at each segment for incidence angles of  $15^{\circ}$ ,  $30^{\circ}$ ,  $45^{\circ}$  and  $60^{\circ}$  for cases ‘a’, ‘b’, ‘c’ and ‘d’ respectively.

In figure 3.20, it can be seen that number of small peaks are increased when compared to  $0^{\circ}$  for different incidence angles. However, any considerable change cannot be observed in the 8-13  $\mu\text{m}$  range. More detailed information is given on table 3.2.

Incidence Angle	Reflection in the 280 nm to 2.5 $\mu\text{m}$ spectrum range	Emission in the 8-13 $\mu\text{m}$ spectrum range
a) $15^{\circ}$	% 99.39	% 74.60
b) $30^{\circ}$	% 99.32	% 75.94
c) $45^{\circ}$	% 98.97	% 76.98
d) $60^{\circ}$	% 97.49	% 77.46

Table 3.2. Rates of reflection and emission for various number of layers in the segments in different spectrum ranges.

When results given in table two is examined, a decrease in solar reflection and increase in emission in the specified spectrum can be observed. A solution to decreased reflection could be increasing the number of layers in the segments which increases reflection as demonstrated in table 3.2.

Cooling performance of the system is evaluated under similar conditions with the previous designs to make a valid comparison. Absorption of the system which consists of 8 different segments, each has 8 layers, with incidence angle of  $40^\circ$  is illustrated in figure 3.21. When heat balance equations are calculated, reflection in 280nm to 2.5  $\mu\text{m}$  range is around %99.2 which reflects nearly  $930 \text{ W/m}^2$  energy. Percentage of the reflection is higher than previous designs by %2-3. In addition to high reflection in the visible and near-infrared spectrum, system has nearly %77 emission in the 8-13  $\mu\text{m}$  range which corresponds to nearly  $112.5 \text{ W/m}^2$  energy to the outer space. At the end system has cooling power of  $85.5 \text{ W/m}^2$  which is higher than performance of the previous designs by around  $20 \text{ W/m}^2$ .

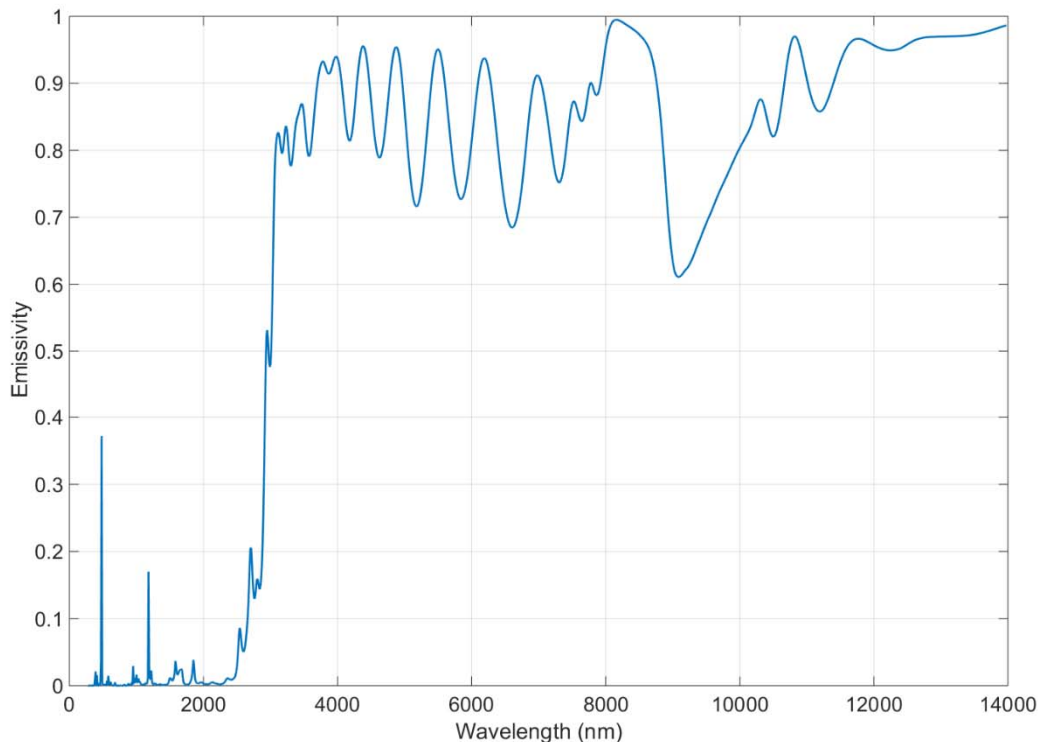


Figure 3.21. Emissivity curve of the third design at  $40^\circ$  incidence angle with 8 segments, each has 8 layers which are quarter wavelength thick.

When the performance of the third design is considered, it can be seen that it is improved drastically. Performance can be further increased by simply increasing number of layers in each segment or by adding more high reflection segments which decreases absorption at the wavelength of interest. Reason of this improvement can be understood by looking at the absorption graph of the system given in figure 3.21. It is very close to ideal emissivity given in figure 3.3 in the spectral range of 280 nm to 2.5  $\mu\text{m}$  and 8-13  $\mu\text{m}$ . However, there is a tremendous difference between actual and ideal absorption in the spectral range of 2.5-8  $\mu\text{m}$  range. High emission in that spectrum occurred, because high reflection segments in the system covers only 280 nm to 2.5  $\mu\text{m}$  spectrum. Extra high reflection segments can be added to enlarge high reflection zone to 8  $\mu\text{m}$ , but it may require much more segments. A more elegant solution can to this problem can be proposed. As mentioned above several times, role of Ag layer in the previous designs is to provide broadband reflection, but because of introduced absorption in the visible spectrum by Ag layer, it is omitted in the new design to improve the overall cooling. Absorption in the visible spectrum occurs in the previous designs, because layers above Ag layer transmits the incident light onto it. If that transmission had prevented, absorption in the visible spectrum would have been avoided. It is already shown that Ag only has strong absorption in the visible spectrum and has low absorption until 14  $\mu\text{m}$  wavelength. So, preventing transmission in the visible spectrum should be sufficient. Because of this situation, a Ag, is added at the bottom of the third design and emission of the system in that case with incidence angle of  $40^\circ$  is shown in figure 3.22.

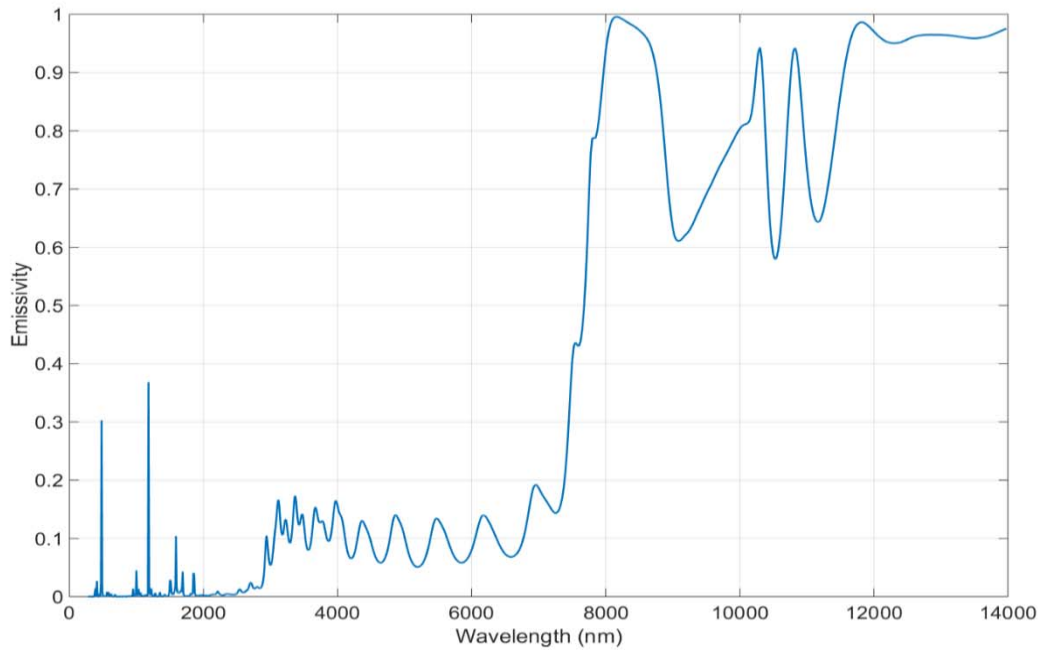


Figure 3.22. Emissivity curve of the third design at 40° incidence angle with 8 segments, each has 8 layers which are quarter wavelength thick and a 50 nm thick Ag layer at the bottom.

When figure 3.22 is observed, it can be seen that absorption in the 2.5-8  $\mu\text{m}$  range is dropped greatly. In addition to this, reflection in the 280 nm to 2.5  $\mu\text{m}$  increased slightly to %99.25 and emission in the 8-13  $\mu\text{m}$  range increased to %85 percentage, whereas it was around %77 in previous case. Overall cooling power increased to 103  $\text{W}/\text{m}^2$  by increasing nearly 20  $\text{W}/\text{m}^2$  when compared to previous case. So, adding a Ag layer makes the emissivity of the system much more close to the ideal emissivity given in figure 3.3, hence increases cooling power drastically.

In this section, several important results are obtained. It is shown that number of layers and their thicknesses' greatly affect the spectral behavior of the system. Also, it is found that by including  $\text{Al}_2\text{O}_3$  and creating triplets, instead of duplexes which consist of  $\text{TiO}_2$  and  $\text{SiO}_2$ , emission performance would be improved without increasing the overall thickness too much and losing from reflection efficiency in the visible and near infrared spectrums. In addition to these, reflection bound in the previous design which stems from presence of a metallic layer is exceeded with the proposed design method. By generating high reflection zones with limited bandwidths in the desired spectrums with periodic high-low indexed layers and compounding those together, improved reflection

performance is obtained without a metallic layer which causes inevitable absorption. Using SiO<sub>2</sub> and TiO<sub>2</sub> in the proposed design also causes emission in 8-13 μm spectrum which is mandatory in radiative cooling. Also, adding a metallic layer at the bottom, increases the reflection after 2.5 μm spectrum and emission in 8-13 μm. So by altering the design structure, tremendous performance improvement is achieved in return of increased number of layers.

#### **4 MINIMIZATION OF REFLECTION ON THE FRONT SURFACE IN THE 8-13 $\mu\text{m}$ SPECTRUM BY USING CHEBYSHEV TRANSFORM**

As stated several times in the previous chapters, for radiative cooling maximizing emissivity of the design in the 8-13  $\mu\text{m}$  range is a requirement. When spectral response of a design to an incident wave is considered, incident wave splits into three components as reflected, transmitted and absorbed. Since one of the requirements of radiative cooling is high emission in the 8-13  $\mu\text{m}$  range, design studies can be carried out by using emitting materials in the 8-13  $\mu\text{m}$  range, as in chapter three. From a mathematical perspective, to increase emission; reflection and transmission have to be minimized since summation of these three coefficients equal to 1. It can be considered as an indirect way of increasing the emissivity of the object. However, minimization of both reflection and transmission is not necessary for emissivity maximization, but minimization of reflection would be enough. If transmission from incident medium, e.g. air, to the system had been increased by layers on top, absorption of the system would increase since transmission percentage of the bottom layers remains as it is. In other words, when quarter wavelength design given in chapter 3 is considered as a multilayer system, an extra transmission region between the incident medium and multilayer system would not alter the transmission percentage of the multilayer system. Role of transmission region is to increase transmission to the multilayer system, by decreasing reflection on the front surface of the multilayer system. Considering that reflection, transmission and absorption coefficients should add up to 1, absorption by the multilayer system should increase, since reflection of it is decreased and transmission is remained similar. A visualization of that case is given in figure 4.1.

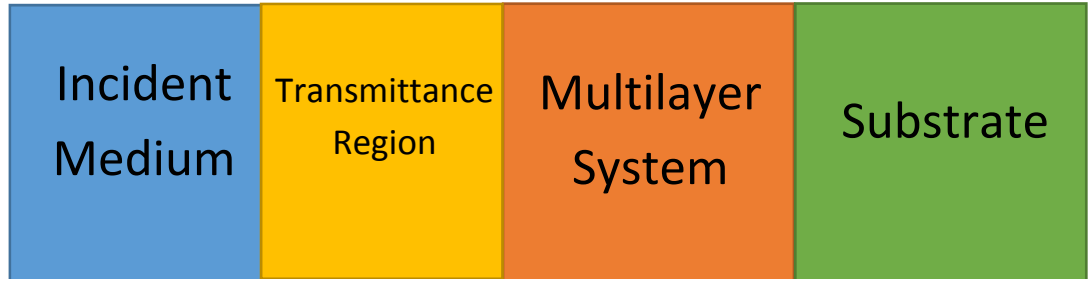


Figure 4.1. ‘Transmittance Region’ is responsible for minimizing the reflection of incident wave from the surface of the multilayer system. In other words, it is used to maximize transmission to the multilayer system and it does not alter the transmittance response of the multilayer system. Since reflection from the surface of the multilayer system is decreased and transparency of it is not changed, its absorption should increase to satisfy Kirchhoff’s scattering law.

One way of increasing transmission in a broadband spectrum is to use impedance matching techniques given in [48]. Purpose of impedance matching is to minimize the reflection between two adjacent mediums by using intermediate layers, each has thickness of quarter of wavelength. Depending on the desired transmission behavior, impedances of the layers are calculated. Chebyshev transform method is used to minimize reflection losses which creates a constant high transmission, bounded by specified ripple, behavior between two different media over a broadband spectrum. Different designs’ performances are evaluated under various conditions, such as center of wavelength, number of layers and ripple values. Firstly, a design is developed for air-Si interface to show that methodology is correct and able to provide expected transmission behavior. Once methodology is verified Chebyshev transform design is developed between air-TiO<sub>2</sub> interface and combined with the quarter wavelength design given in chapter 3 and performance is evaluated.

As a starting point, reflection of a multilayer system can be given as in equation 4.1:

$$\Gamma(\theta) = 2e^{-jN\theta}[\Gamma_0 \cos(N\theta) + \Gamma_1 \cos(N - 2)\theta + \dots + \Gamma_n \cos(N - 2n)\theta + \dots + G(\theta)] \quad (4.1)$$

In equation 4.1, ‘N’ is the number of layers between the two interface and is the only design parameter with the ripple magnitude and center of wavelength. ‘G(θ)’ is a piecewise function and can be expressed as in equation 2.

$$G(\theta) = \begin{cases} \frac{1}{2} \Gamma_{N/2} & \text{for } N \text{ even} \\ \Gamma_{(N-1)/2} & \text{for } N \text{ odd} \end{cases} \quad (4.2)$$

By equating equation 1 with a Chebyshev polynomial whose order is equal to number of layers between the two interface, ' $\Gamma_n$ ' coefficients can be calculated such that overall reflection in equation 4.1 yields similar behavior to Chebyshev polynomial. Chebyshev polynomials from order 2 to 4 is given in equation 4.3.

$$T_2(\cos\theta \sec\theta_m) = \sec^2\theta_m \cos 2\theta + (\sec^2\theta_m - 1)$$

$$T_3(\cos\theta \sec\theta_m) = \sec^3\theta_m \cos 3\theta + (3\sec^2\theta_m - 3)\sec\theta_m \cos\theta \quad (4.3)$$

$$T_4(\cos\theta \sec\theta_m) = \sec^4\theta_m \cos 4\theta + 4\sec^2\theta_m(\sec^2\theta_m - 1)\cos 2\theta \\ + (3\sec^4\theta_m - 4\sec^2\theta_m + 1)$$

Since 2, 3 and 4 layered Chebyshev transformers are designed, polynomials of those orders are given in equation 4.3. Depending on the order of the transformer, coefficients of ' $\cos N\theta$ ' terms can be matched and ' $\Gamma_n$ ' coefficients can be calculated as in the equality 4.4.

$$\Gamma(\theta) = \Gamma_m e^{-jN\theta} T_N(\cos\theta \sec\theta_m) \quad (4.4)$$

In equation 4.3 and 4.4, ' $\sec\theta_m$ ' term exists for which the expression can be seen in equation 4.5.

$$\sec\theta_m = \cosh \left[ \frac{1}{N} \cosh^{-1} \left( \frac{1}{2\Gamma_m} \left| \ln \frac{R_L}{Z_0} \right| \right) \right] \quad (4.5)$$

In equation 4.5,  $Z_L$  is the impedance of air which is  $377 \Omega$  and  $Z_0$  is the impedance of Si or  $\text{TiO}_2$ ,  $110.40 \Omega$  and  $256.75 \Omega$  respectively, depending on the design scenario. Once ' $\Gamma_n$ ' coefficients are calculated, impedance of each layer to satisfy Chebyshev behavior can be calculated as in equation 4.6.

$$Z_{n+1} = Z_n \exp(2\Gamma_n) \quad (4.6)$$

When impedance of each layer is calculated based on equation 4.6, thicknesses of the layers are set to quarter wavelength and design procedure is finished. By using the optical constants given in the literature, impedance of the layers can be calculated from those as in equation 4.7.

$$Z = Z_{air} \sqrt{\frac{\mu_r}{\epsilon_r}} \quad \text{where } \epsilon_r = n^2 \quad (4.7)$$

In equation 4.7, ' $\mu_r$ ' is the relative permeability and ' $\epsilon_r$ ' is the relative permittivity of the medium. In our optical studies, permeability can be assumed as 1 and by using the relationship between refractive index and permittivity, impedance of the layers can be obtained. Then by using the materials that has close value to ideally calculated impedance value, high transmittance region between two mediums with the desired characteristics can be created. Comparisons of transmission performances for various designs can be seen below.

As mentioned above, design performance may vary with respect to center of wavelength, number of layers and ripple magnitude. In figure 4.2, transmission in 8-13  $\mu\text{m}$  spectrum with two layers in air-Si interface, with ripple magnitude of 0.05, for different center of wavelengths can be seen.

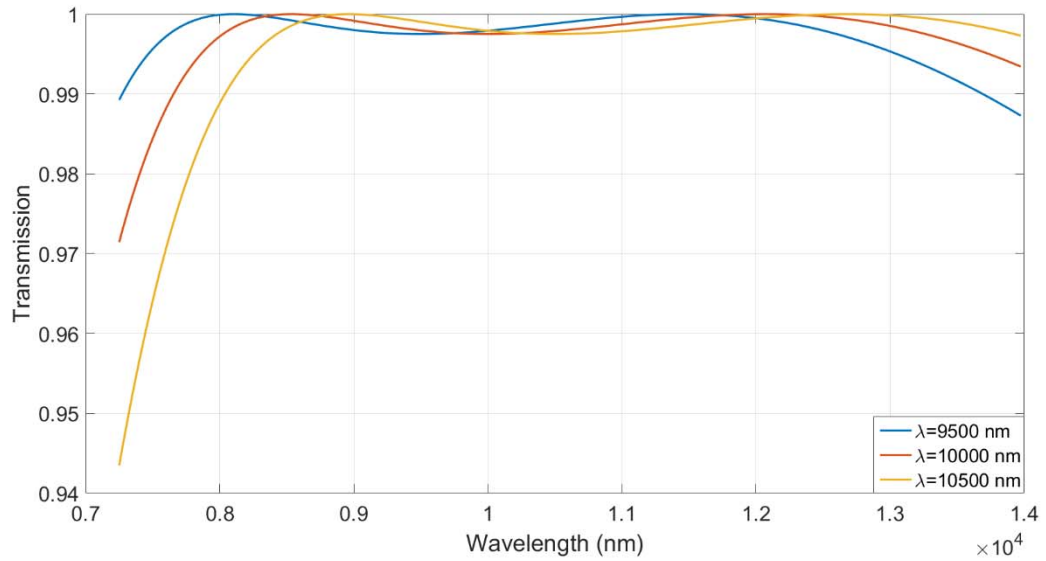


Figure 4.2. Transmission graphs with respect to wavelength, for ripple magnitude 0.05 and 2 layers with center of wavelength 9.5, 10 and 10.5  $\mu\text{m}$  air-Si interface.

In figure 4.2, it can be seen that very high transmission, around %99 percentage, is achieved especially around center of wavelengths. Transmission around center of wavelength is bounded by ' $\Gamma_m$ ', which is 0.05 in this case. Bandwidth of the high transmission zone is around 4  $\mu\text{m}$  which is able to cover 8-13  $\mu\text{m}$  spectrum almost entirely. From the graph it can be seen that, as center of wavelength shifts trough 9.5  $\mu\text{m}$  to 10.5  $\mu\text{m}$ , transmission around 7.5  $\mu\text{m}$  decreases and around 13  $\mu\text{m}$  it increases. So, center of wavelength has to be selected such that it maximizes the transmission in 8-13  $\mu\text{m}$  spectrum. In figure 4.3, results for change of center of wavelength on the performance with 3 layers is shown.

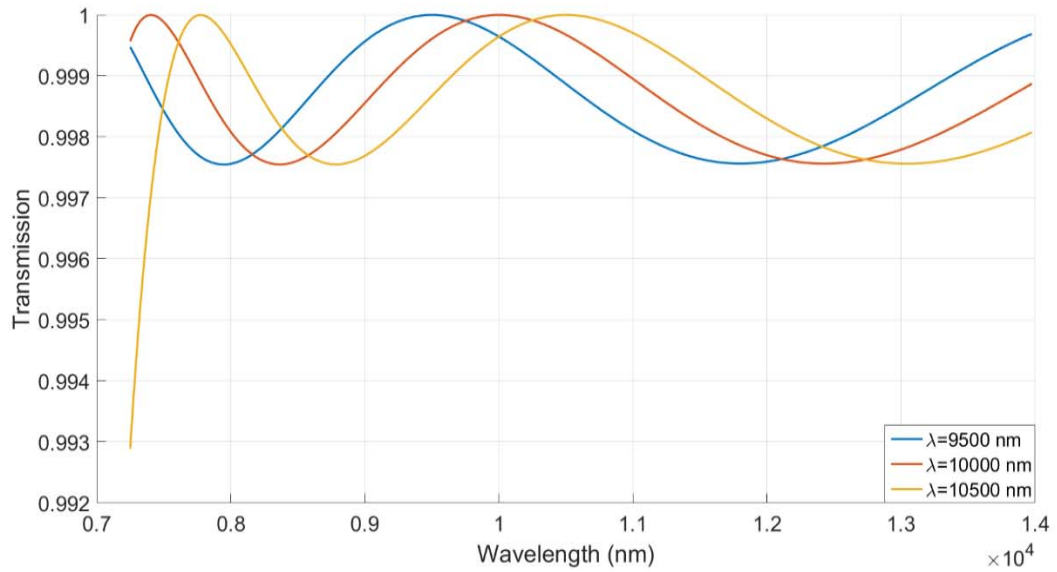


Figure 4.3. Transmission graphs with respect to wavelength, for ripple magnitude 0.05 and 3 layers with center of wavelength 9.5, 10 and 10.5  $\mu\text{m}$  air-Si interface.

In figure 3, similar trend is observed with the results in figure 4.2 in terms of effect of center of wavelength on the performance. Only difference with the previous case is that bandwidth of the high transmission zone is increased considerably. This difference can be observed from the results of design with center of wavelength 10.5  $\mu\text{m}$ . In the previous graph, transmission is nearly %95 percentage around 7.5  $\mu\text{m}$  and it is %99 percentage around 14  $\mu\text{m}$ , whereas in this case transmission around 7.5  $\mu\text{m}$  is also higher than %99 percentage and remains around same percentage until 14  $\mu\text{m}$ . So, when compared with the previous case increasing number of layers clearly enlarged the bandwidth of the high transmission zone. A supportive graph is illustrated in figure 4.4, in which performance for four layers can be seen.

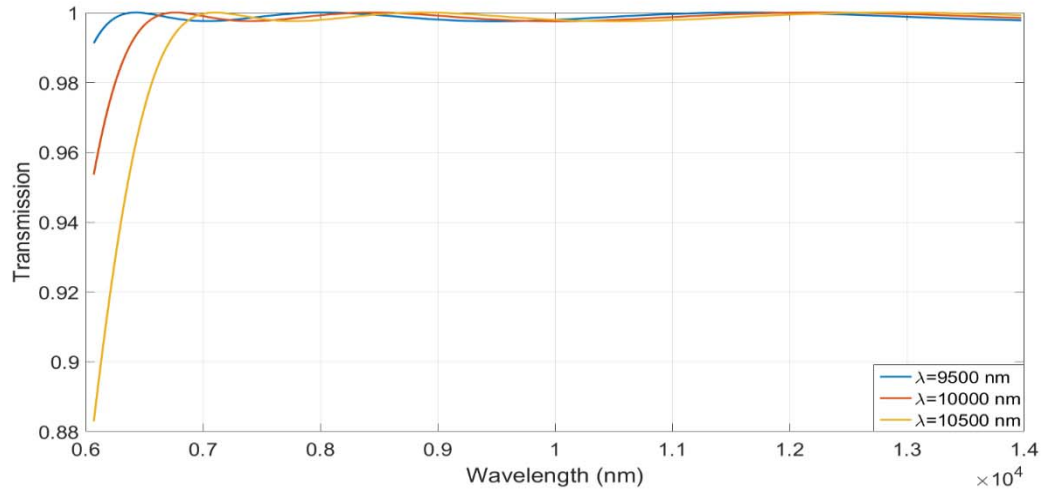


Figure 4.4. Transmission graphs with respect to wavelength, for ripple magnitude 0.05 and 4 layers with center of wavelength 9.5, 10 and 10.5  $\mu\text{m}$  air-Si interface.

From figure 4.4, it can be seen that %99 percentage transmission can be achieved until 14  $\mu\text{m}$ . When compared with the previous scenarios in which center of reflection is around 9.5  $\mu\text{m}$ , high transmission still present around 6  $\mu\text{m}$ , whereas it is not the case for lower number of layers. So, from these results it can be seen by increasing number of layers, bandwidth of the high transmission zone can be enlarged and by altering center of wavelength, transmission in 8-13  $\mu\text{m}$  spectrum can be maximized. After the analysis of the influence of the variation of the center of wavelength, effect of ripple magnitude can be examined. In figure 4.5, transmission graphs of the designs with different ripple magnitudes, with center of wavelength 10  $\mu\text{m}$  and 2 layers, is given.

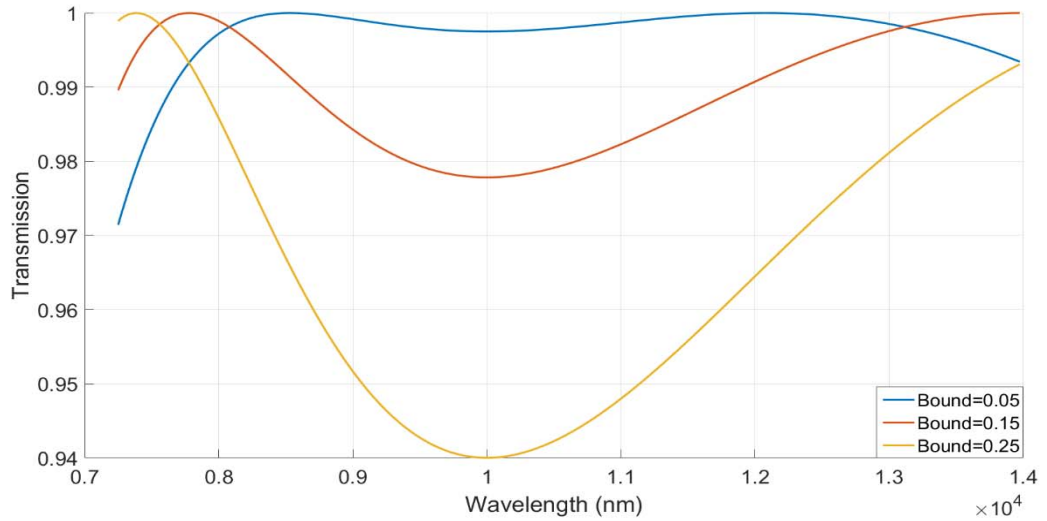


Figure 4.5. Transmission graphs with respect to wavelength, for center of wavelength 10  $\mu\text{m}$  and 2 layers with ripple magnitudes of 0.05, 0.15 and 0.25 air-Si interface.

When figure 5 is examined, it can be seen that as ripple magnitude increases difference between the highest and the lowest transmission rate also increases. It is also observable that bandwidth is not affected by the ripple magnitude. In figure 4.6 and 4.7, results for 3 and 4 layered transformers with different ripple magnitudes around 10  $\mu\text{m}$  is given.

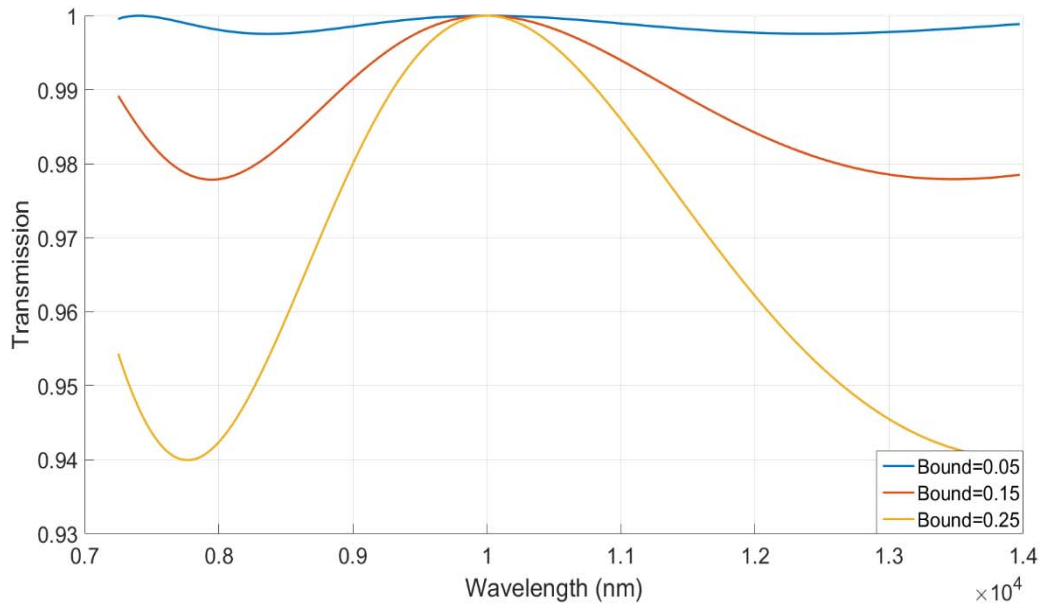


Figure 4.6. Transmission graphs with respect to wavelength, for center of wavelength 10  $\mu\text{m}$  and 3 layers with ripple magnitudes of 0.05, 0.15 and 0.25 air-Si interface.

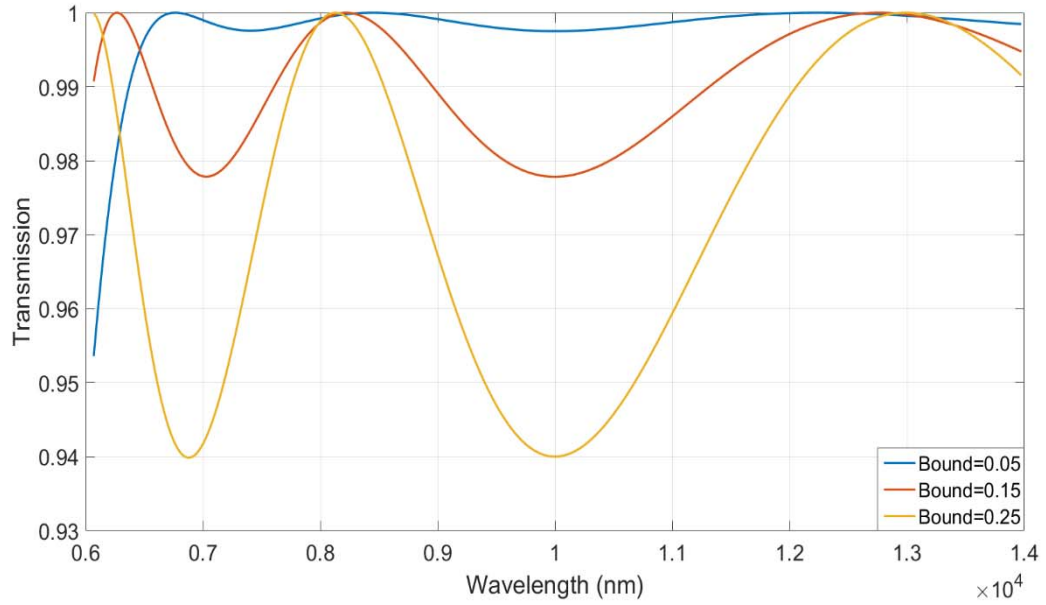


Figure 4.7. Transmission graphs with respect to wavelength, for center of wavelength 10  $\mu\text{m}$  and 4 layers with ripple magnitudes of 0.05, 0.15 and 0.25 for air-Si interface.

When figure 4.6 and 4.7 are examined, no contradiction with the expectations is observed, since bandwidth of the high transmission zones are similar to previous results and as ripple magnitude increases, overall transmission performance decreases in the design spectrum.

Until this point, influence of number of layers, center of wavelength and ripple magnitudes are demonstrated with transmission graphs. In table 4.1 and 4.2, average transmission in 8-13  $\mu\text{m}$  spectrum is given for the cases for which graphs are given above.

Number of Layers \ Center of Wavelength	9.5 $\mu\text{m}$	10 $\mu\text{m}$	10.5 $\mu\text{m}$
2	99.87	99.89	99.84
3	99.86	99.86	99.87
4	99.99	99.99	99.89

Table 4.1. Average transmission in 8-13  $\mu\text{m}$  spectrum for layer numbers of 2, 3 and 4 at center of wavelengths 9.5, 10 and 10.5  $\mu\text{m}$ , with ripple magnitude of 0.05 for air-Si interface.

Number of Layers \ Ripple Magnitude	0.05	0.15	0.25
2	99.89	98.65	95.68
3	99.90	98.96	97.48
4	99.99	99.01	97.14

Table 4.2. Average transmission in 8-13  $\mu\text{m}$  spectrum for layer numbers of 2, 3 and 4 with the ripple magnitudes of 0.05, 0.15 and 0.25, with center of wavelength 10  $\mu\text{m}$  for air-Si interface.

All analysis given above is conducted with perpendicular incidence angle. In order to observe the effect of the incidence angle, a design which has center of wavelength 10  $\mu\text{m}$ , ripple magnitude 0.05 and 3 layers is analyzed for different incidence angles and results are shown in figure 4.8.

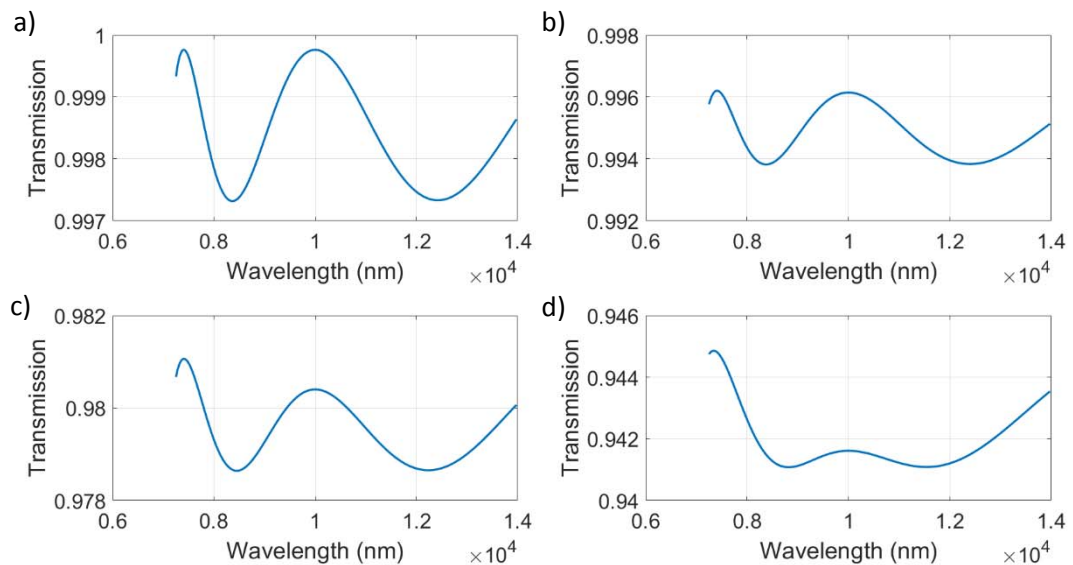


Figure 4.8. Transmittance graphs with respect to wavelength of a design which has 10  $\mu\text{m}$  center of wavelength, 0.05 ripple magnitude and 3 layers with incidence angles of  $15^\circ$ ,  $30^\circ$ ,  $45^\circ$  and  $60^\circ$  from 'a' to 'd' with average performances of %99.83, %99.48, %97.93 and %94.14 respectively.

From figure 4.8, it can be seen that as incidence angle increases, transmission performance in 8-13  $\mu\text{m}$  spectrum decreases, yet it is around %95 at the worst case. After the discussion of the results of air-Si interface, results for air-TiO<sub>2</sub> interface are demonstrated below.

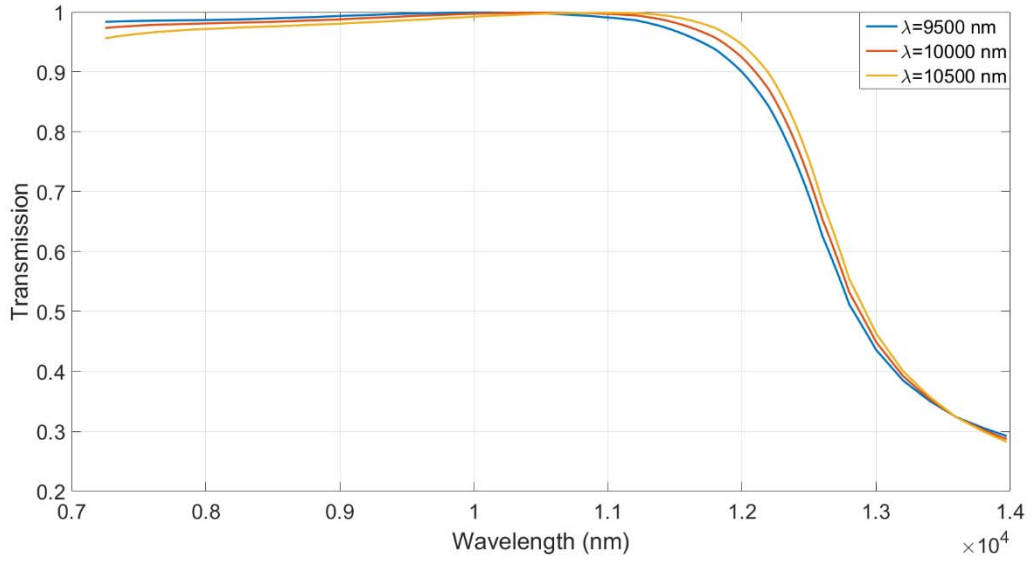


Figure 4.9. Transmission graphs with respect to wavelength, for ripple magnitude 0.05 and 2 layers with center of wavelength 9.5, 10 and 10.5  $\mu\text{m}$  for air-TiO<sub>2</sub> interface.

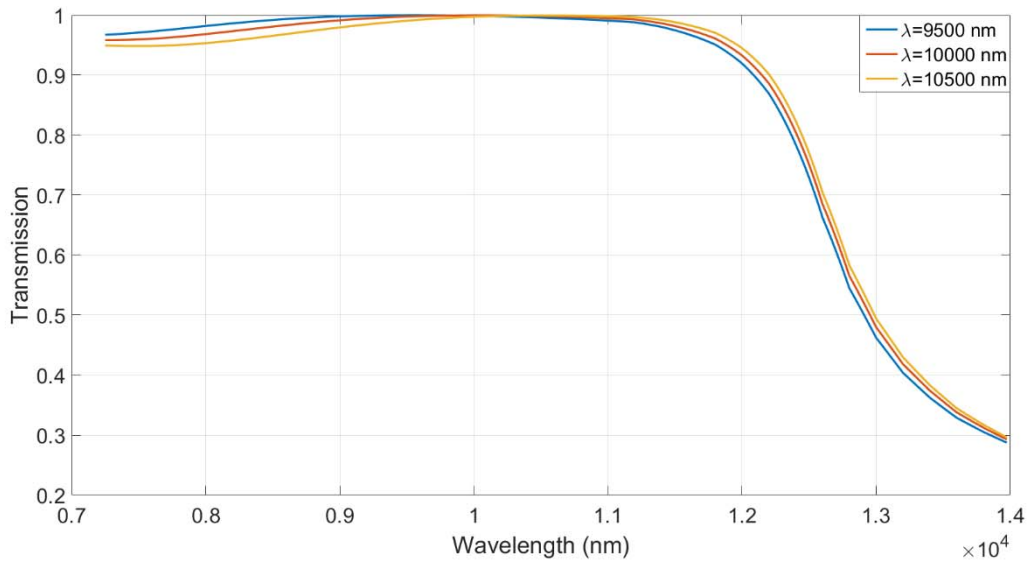


Figure 4.10. Transmission graphs with respect to wavelength, for ripple magnitude 0.05 and 3 layers with center of wavelength 9.5, 10 and 10.5  $\mu\text{m}$  for air-TiO<sub>2</sub> interface.

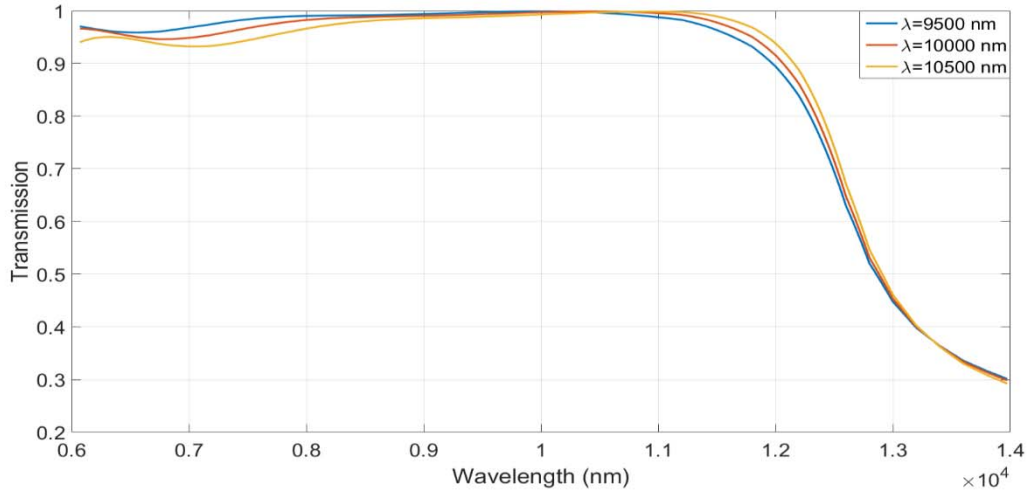


Figure 4.11. Transmission graphs with respect to wavelength, for ripple magnitude 0.05 and 4 layers with center of wavelength 9.5, 10 and 10.5  $\mu\text{m}$  for air-TiO<sub>2</sub> interface.

In figure 4.9, 4.10 and 4.11 effect of change of center of wavelength are examined by comparing the performances of the designs which have 0.05 ripple magnitude and 2, 3 and 4 layers respectively. As in air-Si interface results, high transmission zone is shifted towards right as the value of center of wavelength increases and bandwidth enlarges as number of layers is increased. However, a decline in the transmission after 12  $\mu\text{m}$  is observed. Discussion about this decline is given after the analysis of air-TiO<sub>2</sub> interface for various ripple magnitudes. In figure 4.12, 4.13 and 4.14 transmission performance for the designs which has center of wavelength 10  $\mu\text{m}$  but different ripple magnitudes are illustrated for 2, 3 and 4 number of layers.

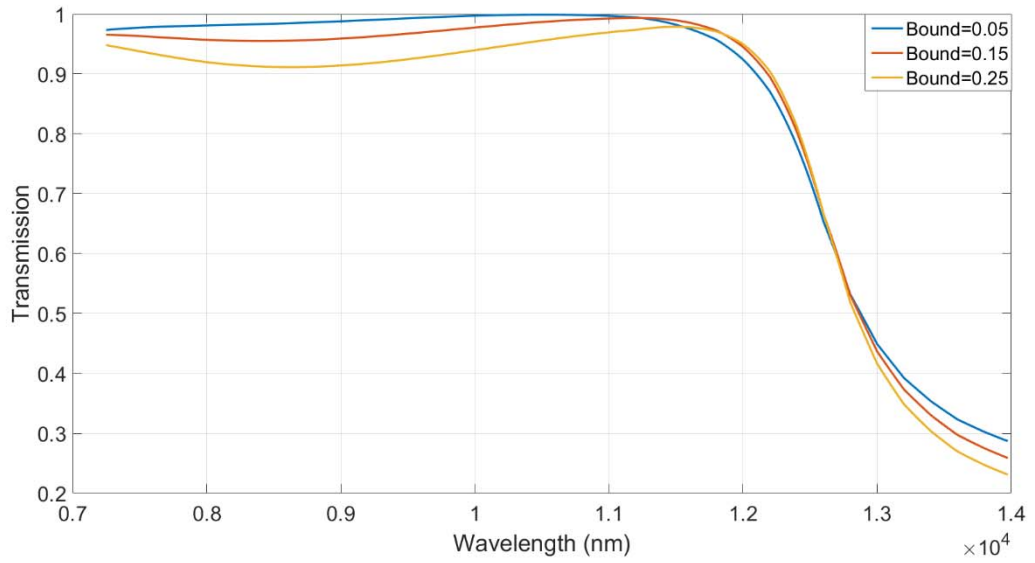


Figure 4.12. Transmission graphs with respect to wavelength, for center of wavelength  $10\ \mu\text{m}$  and 2 layers with ripple magnitudes of 0.05, 0.15 and 0.25 for air-TiO<sub>2</sub> interface.

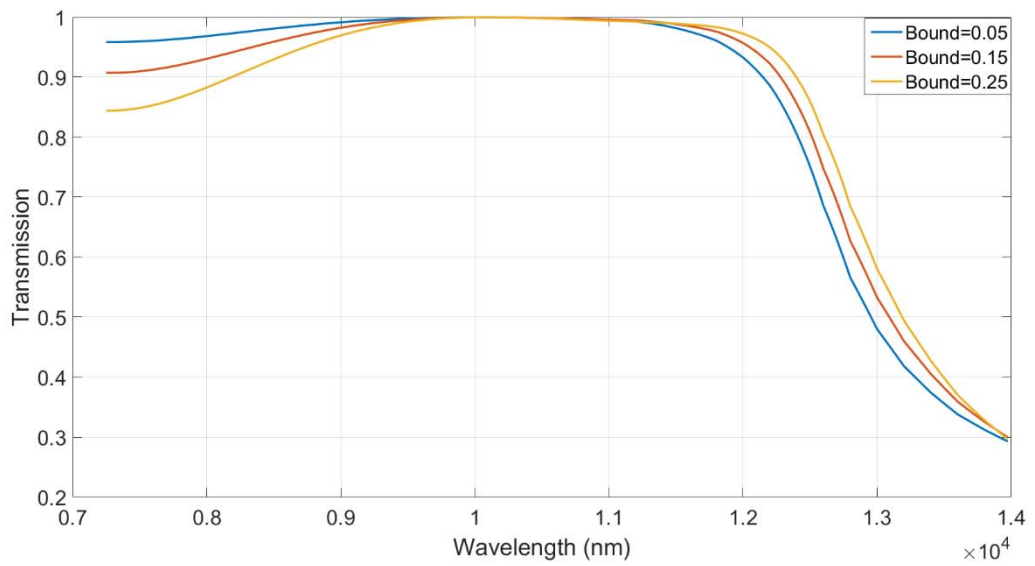


Figure 4.13. Transmission graphs with respect to wavelength, for center of wavelength  $10\ \mu\text{m}$  and 3 layers with ripple magnitudes of 0.05, 0.15 and 0.25 for air-TiO<sub>2</sub> interface.

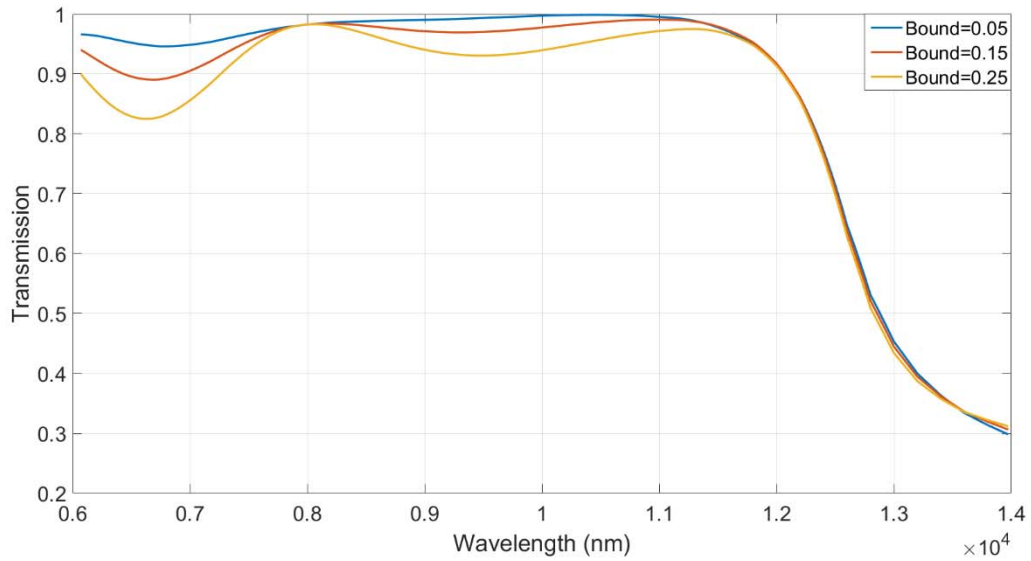


Figure 4.14. Transmission graphs with respect to wavelength, for center of wavelength 10  $\mu\text{m}$  and 4 layers with ripple magnitudes of 0.05, 0.15 and 0.25 for air-TiO<sub>2</sub> interface.

When figure 4.12, 4.13 and 4.14 are examined it can be deduced that as ripple magnitude increases, transmission decreases which is similar in air-Si interface designs. However, decline after 12  $\mu\text{m}$  is still present in the results. From these results, it can be seen that magnitude ripple is not the source of decline after 12  $\mu\text{m}$ .

Source of transmission decline after 12  $\mu\text{m}$  can be understood, if working principle of Chebyshev transform is considered. Since aim of Chebyshev transform is to maximize transmission between two interface by impedance matching, design procedure starts with impedance of two mediums. In equation 4.7, relationship between impedance and refractive index is given. Since refractive index varies with respect to wavelength, impedance of a medium is also dependent on wavelength. However, during the design procedure impedances of the mediums are assumed to be constant along the bandwidth of the Chebyshev transformer. Chebyshev transformer worked in a good way in air-Si interface, since Si has nearly constant refractive index in the 8-13  $\mu\text{m}$  spectrum, however refractive index of TiO<sub>2</sub> decreases gradually in that spectrum. Due to this change, high transmission in the shape of a straight line with respect to wavelength, with constant ripple, cannot be achieved around 12  $\mu\text{m}$ , although it is achieved in air-Si interface for 2, 3 and 4 number of layers. Decline in this spectrum causes performance drop in average transmission, which can be seen in table 4.3 and 4.4 for different conditions.

Number of Layers \ Center of Wavelength	9.5 $\mu\text{m}$	10 $\mu\text{m}$	10.5 $\mu\text{m}$
2	92.43	93.05	93.44
3	93.25	93.58	93.63
4	92.39	92.92	93.29

Table 4.3. Average transmission in 8-13  $\mu\text{m}$  spectrum for layer numbers of 2, 3 and 4 at center of wavelengths 9.5, 10 and 10.5  $\mu\text{m}$ , with ripple magnitude of 0.05 for air-TiO<sub>2</sub> interface

Number of Layers \ Ripple Magnitude	0.05	0.15	0.25
2	93.05	92.14	89.61
3	93.58	94.25	94.48
4	91.97	91.97	90.00

Table 4.4. Average transmission in 8-13  $\mu\text{m}$  spectrum for layer numbers of 2, 3 and 4 with the ripple magnitudes of 0.05, 0.15 and 0.25, with center of wavelength 10  $\mu\text{m}$  for air-TiO<sub>2</sub> interface

Once results for the air-TiO<sub>2</sub> interface are examined, theoretical design can be realized. In order to make this realization, materials which have close impedance values to the ideally calculated impedance values are required. Due to the fact that materials in real life may not have identical impedance values with the calculated ones, there would be an error between the theoretical and real design. 18 different performance comparisons are given above for air-TiO<sub>2</sub> interface and selected 3 designs' performances are demonstrated below. Before the implementation results, refractive index of some materials with respect to wavelength are given in table 4.5.

Material \ Wavelength	9.5 $\mu\text{m}$	10 $\mu\text{m}$	10.5 $\mu\text{m}$
BaF <sub>2</sub>	1.4081	1.4014	1.3941
CaF <sub>2</sub>	1.3137	1.2995	1.2842
LiF	1.1344	1.1005	1.0627
MgF <sub>2</sub>	1.2070	1.1800	1.1562
KCl	1.4583	1.4564	1.4545

Table 4.5. Refractive indexes of BaF<sub>2</sub>, CaF<sub>2</sub>, LiF, MgF<sub>2</sub> and KCl for wavelengths of 9.5, 10 and 10.5  $\mu\text{m}$  which are going to be used in the realization of theoretical design of Chebyshev transformer.

Materials given in table 4.5 are going to be used in the realization of the air-TiO<sub>2</sub> interface designs. First design that is going to be realized has center of wavelength 10.5  $\mu\text{m}$ , 0.05 ripple magnitude and 2 layers. Comparison of performances of theoretical and realized design's is shown in figure 4.15.

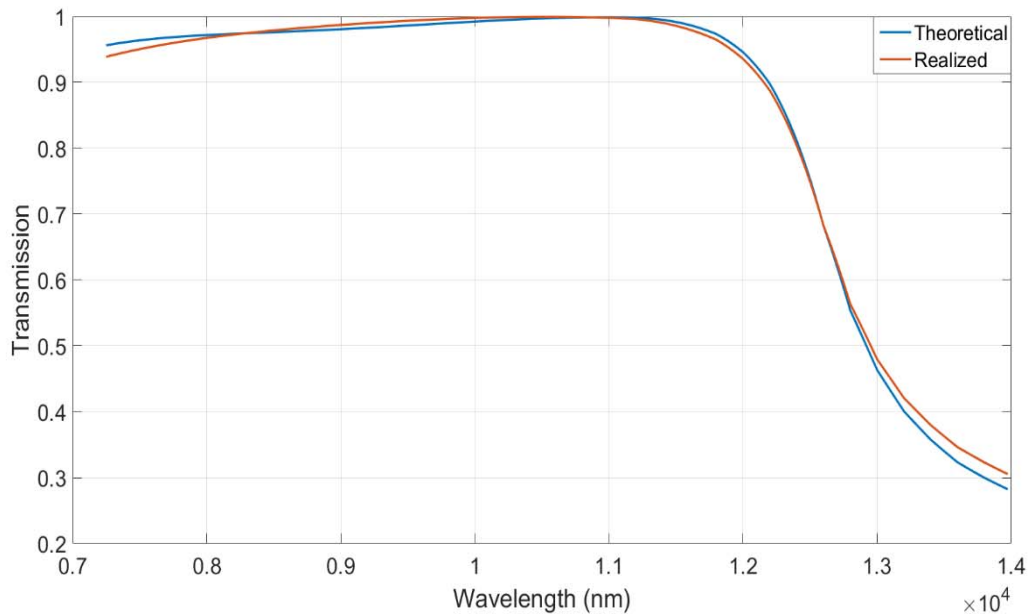


Figure 4.15. Comparison of theoretical and realized design performances in which center of wavelength is 10.5  $\mu\text{m}$ , ripple magnitude is 0.05 and number of layers is two. In theory, average transmission in 8-13  $\mu\text{m}$  range is %93.44, whereas in realization it is %93.16.

In this design, ideal refractive indexes are calculated as 1.1287 and 1.3010. By looking at table 4.5, these refractive indexes are very close to indexes' of  $\text{MgF}_2$  and  $\text{CaF}_2$ , so realization is carried out with these materials. In theory average transmission in 8-13  $\mu\text{m}$  is calculated as %93.44 and in the realized design it is %93.16 which can be considered as a very close match. Next design to be realized is the 3-layer version of the design given in figure 4.15 for which performance comparison between theory and realized versions is given in figure 4.16.

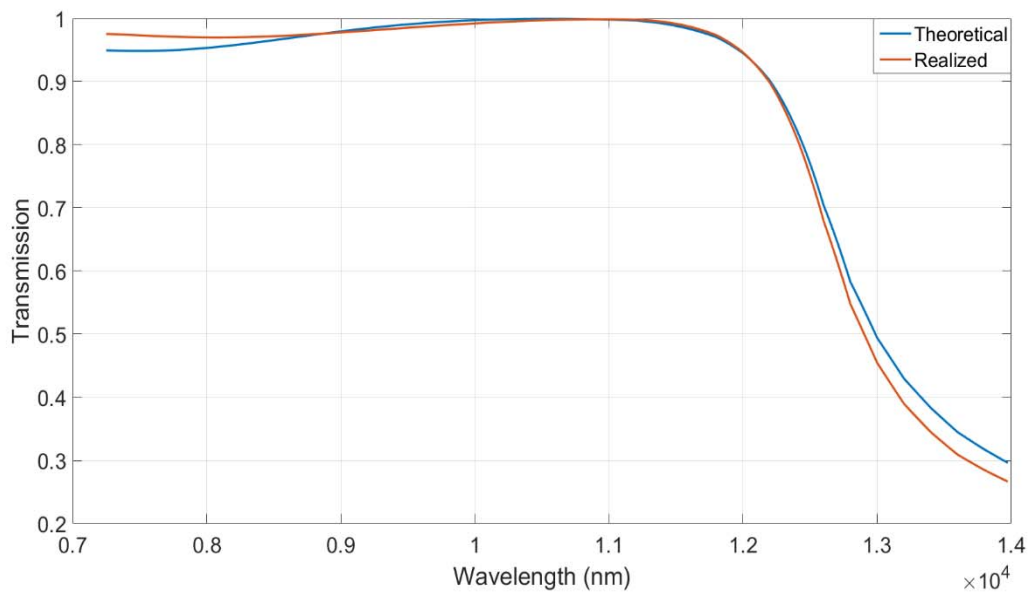


Figure 4.16. Comparison of theoretical and realized design performances in which center of wavelength is 10.5  $\mu\text{m}$ , ripple magnitude is 0.05 and number of layers is three. In theory, average transmission in 8-13  $\mu\text{m}$  range is %93.63, whereas in realization it is %93.29.

For this design, refractive indexes of the layers are calculated as 1.0627, 1.2842 and 1.3941 which are very close to indexes  $\text{LiF}$ ,  $\text{CaF}_2$  and  $\text{BaF}_2$  according to table 4.5. Average transmission is %93.63 in theory, whereas it is dropped to %93.29 when realized. Finally, implementation results for a design with center of wavelength 10  $\mu\text{m}$ , ripple magnitude 0.05 and 4 layers are illustrated in figure 4.17.

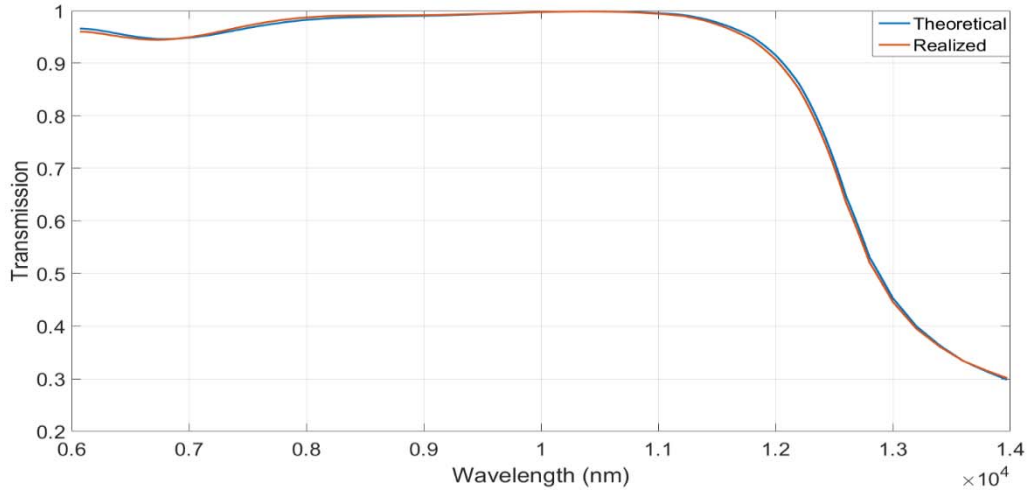


Figure 4.17. Comparison of theoretical and realized design performances in which center of wavelength is 10  $\mu\text{m}$ , ripple magnitude is 0.05 and number of layers is four. In theory, average transmission in 8-13  $\mu\text{m}$  range is %92.92, whereas in realization it is %92.70.

Ideal refractive indexes for the design given in figure 4.17 are 1.4524, 1.3265, 1.1976 and 1.0938 which can be realized by KCl, CaF<sub>2</sub>, MgF<sub>2</sub> and LiF when table 4.5 is considered. In theory average transmission is calculated as %92.92 and it is %92.70 when realized. Similar to previous cases, realization is achieved by a slight difference in the performance. Once it is shown that air-TiO<sub>2</sub> interface Chebyshev designs can be realized with marginal errors, these designs can be combined with the quarter wavelength design to decrease reflection in 8-13  $\mu\text{m}$  range, which would result in increase in absorption.

Realized three air-TiO<sub>2</sub> interface Chebyshev designs are combined with the quarter wavelength design and performance analysis is conducted in each case. Analyses include average reflection in the visible and near-infrared spectrum, reflection decrease in 8-13  $\mu\text{m}$  spectrum and improvement of the absorption in that spectrum. Firstly, design with 10.5  $\mu\text{m}$  center of wavelength, ripple magnitude of 0.05 and 2 layers whose performance is illustrated in figure 4.15 is combined with the quarter design and results are demonstrated in figure 4.18.

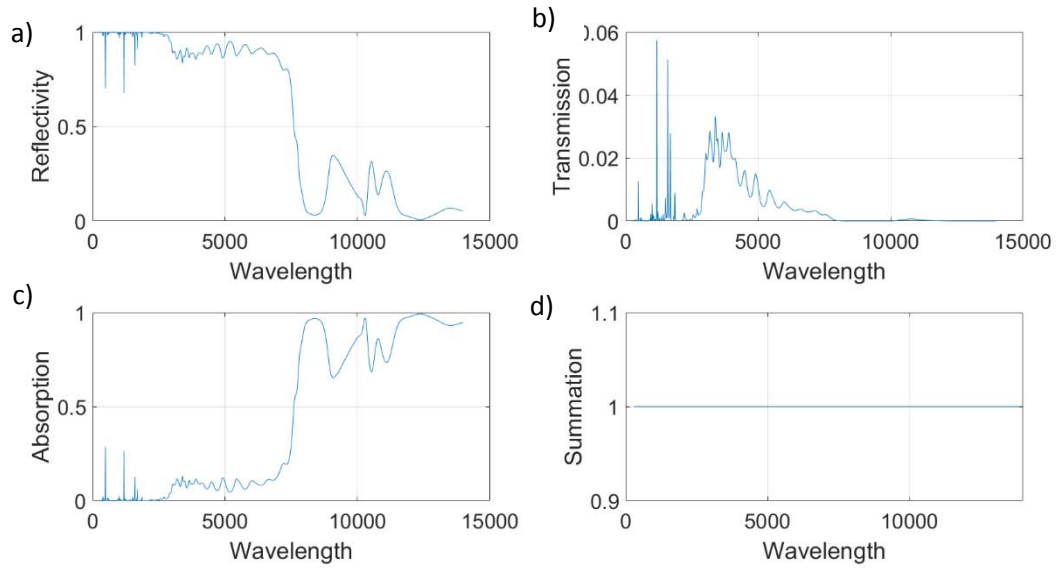


Figure 4.18. a) Reflectivity of quarter wavelength design with Ag combined with transmittance region, consists of 2 layers of MgF<sub>2</sub> and CaF<sub>2</sub>. Average reflection from 280 nm to 2.5 μm is 99.20 and it is %14.29 in 8-13 μm. b) Transmission to the substrate with respect to wavelength. c) Emission/Absorption of the design in which average emission in 8-13 μm is 85.69. d) Summation of reflection, transmission and emission coefficients which equals to 1.

To make comparisons with the quarter wavelength design with Ag spectral behavior of it with average values are going to be used. In the previous design, average reflection in 280 nm to 2.5 μm spectrum is %99.25 and it slightly drops to %99.2 when transmittance region is added. So, transmittance region designed for 8-13 μm spectrum does not alter the behavior in the visible and near-infrared spectrum. When emission of the previous design in the 8-13 μm is considered, emission percentage is %84.15 and reflection is %15.83. Absorption and reflection in that spectrum is changed to %85.69 and % 14.29 when transmission region is added. It can be seen that nearly %1.55 percentage of decrease in the reflection is added to absorption which is an expected behavior. Secondly, similar comparisons are made and graphs of the results are given below in figure 4.19.

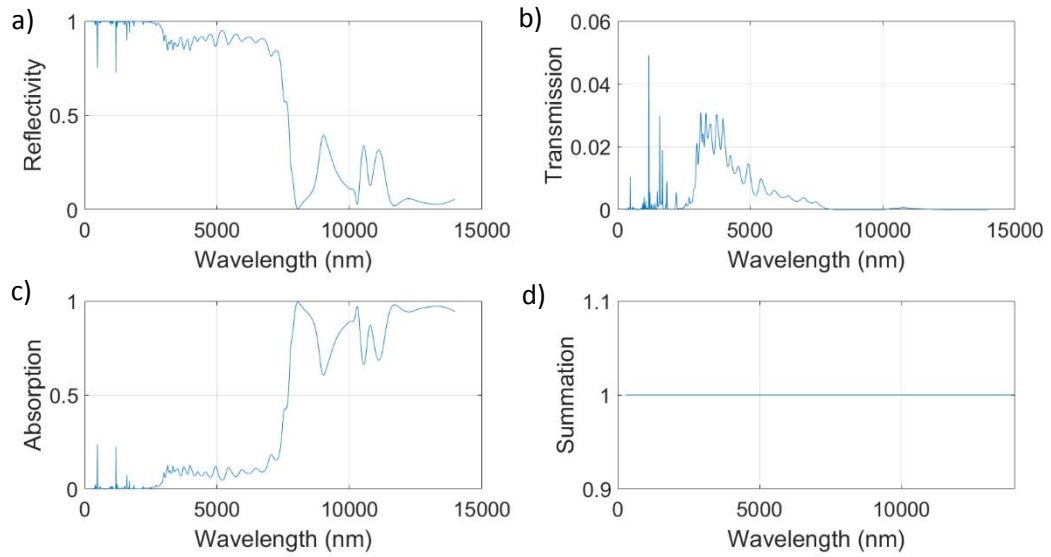


Figure 4.19. a) Reflectivity of quarter wavelength design with Ag combined with transmittance region, consists of 3 layers of LiF, CaF<sub>2</sub> and BaF<sub>2</sub>. Average reflection from 280 nm to 2.5  $\mu\text{m}$  is 99.29 and it is %13.89 in 8-13  $\mu\text{m}$ . b) Transmission to the substrate with respect to wavelength. c) Emission/Absorption of the design in which average emission in 8-13  $\mu\text{m}$  is 86.10. d) Summation of reflection, transmission and emission coefficients which equals to 1.

When integrated from 280 nm to 2.5  $\mu\text{m}$  spectrum, reflection percentage becomes %99.29 which is slightly higher than average reflection of the previous design. Reflection and absorption percentages are %13.89 and %86.10 in 8-13  $\mu\text{m}$  spectrum. Decrease in reflection is around %1.95 which is equals to increase in emission, as in the case of previous analysis. Finally, design with 4 layers which has center of wavelength 10  $\mu\text{m}$  and ripple magnitude 0.05 is added on top of a quarter wavelength design and results are shown in figure 4.20.

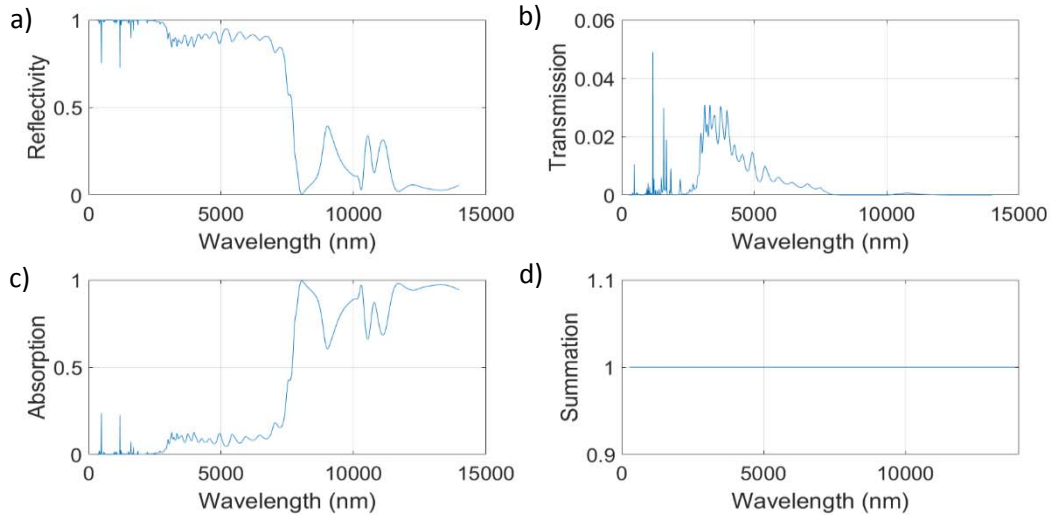


Figure 4.20. a) Reflectivity of quarter wavelength design with Ag combined with transmittance region, consists of 4 layers of LiF, MgF<sub>2</sub>, CaF<sub>2</sub> and BaF<sub>2</sub>. Average reflection from 280 nm to 2.5  $\mu\text{m}$  is 99.22 and it is %13.04 in 8-13  $\mu\text{m}$ . b) Transmission to the substrate with respect to wavelength. c) Emission/Absorption of the design in which average emission in 8-13  $\mu\text{m}$  is 86.94. d) Summation of reflection, transmission and emission coefficients which equals to 1.

In this design, average reflection in 280 nm to 2.5  $\mu\text{m}$  spectrum is %99.22 percentage which is very close to the performance of the design which does not have transmission region. Mean reflection in the 8-13  $\mu\text{m}$  is around %13.04, which is smaller than quarter wavelength design's by %2.79. Absorption in that spectrum is %86.94, which indicates that %2.79 performance improvement is achieved by in 8-13  $\mu\text{m}$ , when compared to quarter wavelength design. As in the case of previous comparisons, decrease in reflection results in increase in absorption. When cooling performance of this design is analyzed, it is observed that %2.79 increase in absorption in the 8-13  $\mu\text{m}$  spectrum, results in 5 W/m<sup>2</sup> increase in the cooling power.

In this chapter, an indirect way of improving absorption performance in the 8-13  $\mu\text{m}$  is discussed and related results to discussion are illustrated. By using Chebyshev polynomials, which are used in impedance matching, a transmission region is created between air and TiO<sub>2</sub> whose aim is to decrease reflection on the front surface. It is observed that absorption is increased by the amount of decrease in reflection when transmission region is added. Based on this finding, a new design with an antireflective coating which covers entire atmospheric transmittance window can be developed which minimizes reflection loss in that spectrum. Then, transmitted components can be absorbed to increase cooling power in radiative cooling applications.

## 5 CONCLUSION

In this thesis, spectral behaviors of different thin film coating systems are examined in order to end up with new radiative cooling designs that have improved performance. For that purpose, a model is used which is able to obtain reflection, absorption and transmission of a multilayer thin film system depending on number of layers, optical properties of the materials from which the layers are composed, thicknesses of the layers, incidence angle and wavelength. Before design studies, for the performance evaluations, heat dynamics between an object and its surroundings are expressed with the equations and incident solar irradiance depending on date and location is calculated. Finally, optical properties and spectral behaviors of the several materials are investigated and results are demonstrated to find materials that can be used in a radiative cooling designs.

For the design studies, initially a design given in the literature is developed and performance of it is evaluated. Then it is shown that by changing number and thicknesses of the layers, emission in 8-13  $\mu\text{m}$  range can be increased. Also, by including extra layers composed of materials which have emission in the 8-13  $\mu\text{m}$  spectrum also improves the emission performance even without increasing overall thickness and reducing reflection in 400 nm to 2.5  $\mu\text{m}$  spectrum. Based on these findings, new designs can be developed which highly emits energy to outer space.

Secondly, another approach is used which alters the design structure given in the literature dramatically. Its novelty is the way of obtaining high reflection in 400 nm to 2.5  $\mu\text{m}$  spectrum. With the proposed method given in this thesis, quarter wavelength design, high reflection zone in the 400 nm to 2.5  $\mu\text{m}$  spectrum can be generated by using only dielectrics, which does not cause inevitable absorption in that spectrum, as metallic layers used in the previous designs do. Also, using dielectric materials to create high reflection zones, which have emission in the 8-13  $\mu\text{m}$  spectrum, increases the emission

in 8-13  $\mu\text{m}$  spectrum. Reason for this performance improvement in the emission is the increased number of emitting layers, which is an expected outcome when previous findings given in this thesis are considered. Only negation of this design is the increased number of layers which would cause difficulties in the production process. As a result of material investigations,  $\text{TiO}_2$  and  $\text{SiO}_2$  are chosen as best materials for the design. Reflection of this design in the 400 nm to 2.5  $\mu\text{m}$  spectrum is around %99 percentage and it has %85 percentage emission in the 8-13  $\mu\text{m}$  spectrum which corresponds to 103  $\text{W}/\text{m}^2$  cooling power.

Finally, another novel way of increasing the performance of the overall system in an indirect fashion is proposed. By using Chebyshev transform impedance matching technique, reflection on the front surface of the quarter wavelength design in the 8-13  $\mu\text{m}$  spectrum is decreased by including Chebyshev layers between air and  $\text{TiO}_2$ . Decrease in reflection is resulted in increase in absorption in that spectrum. This behavior occurs, because transmission percentage of the quarter wavelength design remains as it is when Chebyshev layers are added, since structure of it is not altered. However, considering the fact that Chebyshev layers decreases the reflection on the front surface of the multilayer system, absorption in that spectrum increases in order to balance the reduction in the reflection. Balance is created by increase in absorption certainly, because transmission of the multilayer remains as it is.

In conclusion, aim of performance improvement of radiative cooling in the presence of solar irradiation is achieved greatly with the proposed methods given in this thesis. Intuition behind those methods and corresponding results are summarized above in the conclusion section. Below, reason for novelty of those methods are explained by discussing their contribution to the literature.

Previous designs given in the literature are based on optimization methods and include a metallic layer, which generally absorbs solar irradiance, for broadband reflection. However, as mentioned several times throughout the thesis, presence of such metallic layer limits the reflection percentage. When such layer is excluded from the design, average reflection drops to extremely low percentages and makes radiative cooling impossible. It would be difficult to generate high reflection requirement without a metallic layer with the optimization methods. To overcome such problem, quarter wavelength method is proposed in which sub-designs are developed to generate high

reflection zones in the desired spectrum and brought together to cover entire visible spectrum with high reflection. It is an entirely new approach for radiative cooling system designs with improved performances over the designs given in the literature.

Usage of Chebyshev transform in this field is the other novelty of this thesis. Chebyshev transform is an impedance matching technique to maximize transmission mainly used in microwave engineering. Although there are methods for increasing amount of absorption with Chebyshev transform [49], proposed way of achieving this is entirely different in this thesis. This is achieved by including air gaps between absorbing mediums with Chebyshev designs. However, proposed method does not include air gaps and materials that are used does not absorb in the desired spectrum. So, Chebyshev transformation is designed in a way that it is used to maximize transmission and combined with the previously designed periodic quarter wavelength design. As a result, Chebyshev transform maximizes the transmission onto the periodic design, by minimizing the reflection on the front surface of it. Since transmission of periodic quarter wavelength design is almost zero, equality given in 1.1 is satisfied by absorption increase to balance reflection decrease on the front surface. So with the combination of two different designs, absorption/emission in the 8-13  $\mu\text{m}$  spectrum is increased in an indirect fashion.

Based on these improvements, it can be deduced that different design approaches given in the literature would yield outstanding performance improvements. Also, studies and proposed design methods contribute to the literature with their novelty.

## 6 REFERENCES

- [1] Heavens, O. S. (1986). *Thin-film Optical Filters. Optica Acta: International Journal of Optics* (Vol. 33).
- [2] Kirby, P. L. (1978). *Thin Solid Films*, 50, 211-221.
- [3] Krüger, G., (1972). “335 applications of thin films in commercial electronics”, *12*(3), 335–339.
- [4] Xi, J.-Q., Schubert, M., F., Kim, J., K., Schubert, E., F., Chen, M., Lin, S., Liu, W., Smart, J.A. (2007). “Optical thin-film materials with low refractive index for broadband elimination of Fresnel reflection”. *Nature Photonics*, 1, 176-179.
- [5] Rees, N. D., James, S. W., Tatam, R. P., & Ashwell, G. J. (2002). Optical fiber long-period gratings with Langmuir-Blodgett thin-film overlays. *Optics Letters*, 27(9), 686–688.
- [6] Korotcenkov, G., Brinzari, V., Schwank, J., DiBattista, M., & Vasiliev, A. (2001). Peculiarities of SnO<sub>2</sub> thin film deposition by spray pyrolysis for gas sensor application. *Sensors and Actuators, B: Chemical*, 77(1-2), 244–252.
- [7] Aberle, A. G. (2009). Thin-film solar cells. *Thin Solid Films*, 517(17), 4706–4710.
- [8] Contreras, M. A., Egaas, B., Ramanathan, K., Hiltner, J., Swartzlander, A., Hasoon, F., & Noufi, R. (1999). Progress Toward 20% Efficiency in Cu(In,Ga)Se<sub>2</sub> Polycrystalline Thin-film Solar Cells. *Progress in Photovoltaics: Research and Applications*, 7, 311–316.
- [9] Moorthy, B., K. (2015). “Thin Film Structures in Energy Applications”.
- [10] Santamouris, M., & Asimakopoulos, D. (1996). Passive cooling of buildings. *Passive Cooling of Buildings*, 28(1), 424–453.

- [11] Performance and applicability of passive and low-energy cooling systems. *Energy and Buildings*, 17(3), 177–199.
- [12] Craig, S., Harrison, D., Cripps, A., & Knott, D. (2008). BioTRIZ Suggests Radiative Cooling of Buildings Can Be Done Passively by Changing the Structure of Roof Insulation to Let Longwave Infrared Pass. *Journal of Bionic Engineering*, 5(1), 55–66.
- [13] Diatezua, D. M., Thiry, P. A., Dereux, A., & Caudano, R. (1996). Silicon oxynitride multilayers as spectrally selective material for passive radiative cooling applications. *Solar Energy Materials and Solar Cells*, 40(3), 253–259.
- [14] Retrieved (2016) from, <https://atran.sofia.usra.edu/cgi-bin/atran/atran.cgi>
- [15] Smith, R. (2005). *Computing the Planck Function*. Professional Paper, Yale University.
- [16] Catalanotti, S., Cuomo, V., Piro, G., Ruggi, D., Silvestrini, V., & Troise, G. (1975). The radiative cooling of selective surfaces. *Solar Energy*, 17(2), 83–89.
- [17] Granqvist, C.G. and Hjortssberg, A. (1980). Surfaces for radiative cooling: Silicon monoxide films on aluminum. *Applied Physics Letters*, 36, 139-141.
- [18] Granqvist, C. G. and Hjortsberg, A., (1981). “Radiative cooling to low temperatures: General considerations and application to selectively emitting SiO films”. *Journal of Applied Physics*, 52, 4205-4220.
- [19] Berdahl, P., Martin, M., & Sakkal, F. (1983). Thermal performance of radiative cooling panels. *International Journal of Heat and Mass Transfer*, 26(6), 871–880.
- [20] Orel, B., Gunde, M. K., & Krainer, A. (1993). Radiative cooling efficiency of white pigmented paints. *Solar Energy*, 50(6), 477–482.
- [21] Chetan N. Suryawanshi and Chhiu-Tsu Lin, (2009). Radiative Cooling: Lattice Quantization and Surface Emissivity in Thin Coatings. *ACS Applied Materials & Interfaces*, 1(6), 1334-1338.
- [22] A.R. Gentle and G. B. Smith, (2010). Radiative Heat Pumping from the Earth Using Surface Phonon Resonance Nanoparticles. *Nano Letters*, 10(2), 373-379.

- [23] Nilsson, T. M. J., Niklasson, G. A., & Granqvist, C. G. (1992). A solar reflecting material for radiative cooling applications: ZnS pigmented polyethylene. *Solar Energy Materials and Solar Cells*, 28(2), 175–193.
- [24] Nilsson, T. M. J., & Niklasson, G. A. (1995). Radiative cooling during the day: simulations and experiments on pigmented polyethylene cover foils. *Solar Energy Materials and Solar Cells*, 37(1), 93–118.
- [25] Silvestrini, V., Peraldo, M., & Monza, E. (1982). Covering Element screening off the solar radiation for the applications in the refrigeration by radiation. *US Patent 4,323,619*.
- [26] Fleming, J. G., Lin, S. Y., El-Kady, I., Biswas, R., & Ho, K.M. (2002). “All-metallic three-dimensional photonic crystals with a large infrared bandgap”. *Nature*, (417), 52-55.
- [27] P. Bermel, M. Ghebrebrhan, W. Chan, Y. Yeng, M. Araghchini, R. Hamam, C. Marton, K. Jensen, M. Soljačić, J. Joannopoulos, S. Johnson, and I. Celanovic, (2010). "Design and global optimization of high-efficiency thermophotovoltaic systems," *Opt. Express* 18, A314-A334.
- [28] Xiaofeng, Z., Jianjun, L., Huafeng L., & Sihai, C. (2010). “Performance analysis of thermophotovoltaic system with an equivalent cut-off blackbody emitter”. *Journal of Applied Physics*, (108), 074507.
- [29] Rephaeli, E., Fan, S. (2009). "Absorber and emitter for solar thermophotovoltaic systems to achieve efficiency exceeding the Shockley-Queisser limit," *Opt. Express* 17, 15145-15159.
- [30] Wu, C., Neuner III, B., John, J., Milder, A., Zollars, B., Savoy, S., & Shvets, G. (2012). “Metamaterial-based integrated plasmonic absorber/emitter for solar thermo-photovoltaic systems”. *Journal of Optics*, 14(2), 024005.
- [31] Le Gall, J., Olivier, M., Greffet, J. (1997). “Experimental and theoretical study of reflection and coherent thermal emission by a SiC grating supporting a surface-phonon polariton”. *Phys. Rev. B*, 55, 10105.
- [32] Greffet, J.-J., Carminati, R., Joulain, K., Mulet, J.-P., Mainguy, S., Chen, Y. (2002). “Coherent emission of light by thermal sources”. *Nature*, 416, 61-64.

- [33] Luo, C.; Narayanaswamy, A.; Chen, G.; Joannopoulos, J. D. (2004). "Thermal radiation from photonic crystals: A direct calculation". *Phys. Rev. Lett.*, 93, 213905.
- [34] Chan, D. L. C.; Soljčić, M.; Joannopoulos, J. D. (2006). "Thermal emission and design in 2D-periodic metallic photonic crystal slabs". *Opt. Express*, 14, 8785-8796.
- [35] Fleming, J. G.; Lin, S. Y.; El-Kady, I.; Biswas, R. (2002). "All-metallic three-dimensional photonic crystals with a large infrared bandgap". *Nature*, 417, 52-55.
- [36] Rephaeli, E.; Fan, S. (2008). "Tungsten black absorber for solar light with wide angular operation range". *Appl. Phys. Lett.*, 92, 211107.
- [37] Arpin, K. A.; Losego, M. D.; Braun, P. V. (2011). "Electrodeposited 3D tungsten photonic crystals with enhanced thermal stability". *Chem. Mater.*, 23, 4783-4788.
- [38] Wang, M.; Hu, C.; Pu, M.; Huang, C.; Zhao, Z.; Feng, Q.; Luo, X. (2011). "Truncated spherical voids for nearly omnidirectional optical absorption". *Opt. Express*, 19, 20642-20649.
- [39] Zhang, S.; Li, Y.; Feng, G.; Zhu, B.; Xiao, S.; Zhou, L.; Zhao, L. (2011). "Strong infrared absorber: surface-microstructured Au film replicated from back silicon". *Opt. Express*, 19, 20462-20467.
- [40] Zhu, L., Raman, A., Wang, K., Anoma, M., Fan, S. (2014). "Radiative cooling of solar cells," *Optica* 1, 32-38.
- [41] Rephaeli, E., Raman, A., & Fan, S. (2013). Ultrabroadband photonic structures to achieve high-performance daytime radiative cooling. *Nano Letters*, 13(4), 1457–1461.
- [42] Raman, A. P., Anoma, M. A., Zhu, L., Rephaeli, E., & Fan, S. (2014). Passive radiative cooling below ambient air temperature under direct sunlight. *Nature*, 515(7528), 540–544.
- [43] Retrieved (2016) from,  
<https://www2.pvlighthouse.com.au/calculators/solar%20spectrum%20calculator/solar%20spectrum%20calculator.aspx>
- [44] Luciuk, M. (2016). *Temperature and Radiation*.
- [45] Palik, E. (1997). *Handbook of Optical Constants of Solids*.

- [46] Larruquert , J. I., Pérez-Marín, A. P., García-Cortés, S., Rodríguez-de Marcos, L., Aznárez, J. A., Méndez, J. A. (2011). “Self-consistent optical constants of SiC thin films”. *J. Opt. Soc. Am. A* 28, 2340-2345.
- [47] Tikhonravov, A. V., Trubetskov, M. K., DeBell, G. W. (1996). “Application of the needle optimization technique to the design of optical coatings”. *Appl. Opt.* 35, 5493–5508.
- [48] Balanis, C. A. (2005). *Antenna Theory Analysis and Design, Third Edition*.
- [49] Saville, P. (2005). Review of Radar Absorbing Materials Defence R & D Canada – Atlantic. Defence Research and Development Canada.